



StudienArbeit Nr.

Investigation of two CFD validation test cases for turbulent mixing of different gaseous species (fuel and oxidizer) in typical laboratory flame configurations

Mr. Malav M Soni
Matriculation Number:
4360054

Submitted to: Prof. Dr.-Ing. R. Radespiel
Institut für
Strömungsmechanik
Herrmann-Blenk-Straße 37
38108
Braunschweig
Deutschland

Supervisor: Dr. rer. nat. Thorsten J. Möller

Publication:

Acknowledgment

Firstly I would like to thank my supervisor; Dr Thorsten J. Möller, Institut für Strömungs-Mechanik, Technische Universität Braunschweig, for all the support and constant encouragement throughout the duration of my work.

I would like to take this opportunity and express my deep gratitude towards ANSYS Germany GmbH, for allowing me to carry out my work and providing me with the excellent facilities for my work. I would like to express my sincere gratitude to my supervisor at ANSYS Germany GmbH, Dr. Thomas Frank for his aspiring guidance, patience, motivation, and immense knowledge. Dr. Frank, you have been an excellent mentor for me. I would like to express my warm thanks to my colleague at ANSYS Germany GmbH; Dr. Hendrik Forkel, for providing me with the insightful ideas and sharing his simulation Knowledge with me. I would like to also acknowledge Marc Kainz at ANSYS Germany GmbH for his help and suggestions related to the mesh generation.

Lastly, I would express my sincere thanks to other students; Monzer Rayya and Yunqing Dong at ANSYS Germany GmbH for all the simulating talks and productive discussions which kept me motivated during my stay at ANSYS Germany GmbH.

ABSTRACT:

Primary purpose of this study is to validate the turbulence models available in ANSYS CFX 16.1 and ANSYS Fluent 17.0 against two test cases viz. Sandia national laboratory propane jet and Sydney bluff body jet flame. This study is divided in to two sections a) Investigation of Sandia National Laboratory Propane Jet b) Investigation of Sydney Bluff Body jet. Both investigations involve simulations carried out under isothermal, non-reacting and steady state conditions. Sandia propane jet configuration involves quasi-2D meshes, defined as the 2D mesh rotated by 5° in the circumferential direction, used for computation. In order to validate the test configurations numerically the turbulence models k- ω SST, k- ϵ , BSL RSM (Base Line Reynolds Stress Model) and EARSM (Explicit Algebraic Reynolds Stress Model) from ANSYS CFX 16.1 and k- ω SST, standard k- ϵ , realizable k- ϵ models from ANSYS Fluent 17.0 were used. Round jet anomaly phenomenon was addressed and modification in the dissipation (ϵ) equation of k- ϵ model was applied and the results compared with the experimental data. The second case study with Sydney Bluff Body Jet flame, involved full 3D meshes for the numerical investigation. Investigation was carried out with k- ω SST and standard k- ϵ turbulence models in ANSYS CFX 16.1 and k- ω SST, standard k- ϵ and realizable k- ϵ turbulence model in ANSYS Fluent 17.0.

In the Sandia Propane Jet case, a small single vortex recirculation region was obtained behind the bluff body. Mean axial velocity (U m/s) was under-predicted by all RANS models, used for this investigation, along the centerline when compared with the experimental data. The reason for this can be the simplifying assumptions made in the RANS models i.e. isotropic turbulence and round jet anomaly phenomenon. Results from modification in the constant of dissipation equation delivered that, on one side improvement is obtained in the results of certain quantity and on other side there is deterioration in the result of other quantity. Difficulties in order to achieve convergence were observed in the k- ϵ turbulence models, but they delivered results that were in good agreement with the experimental data, along with k- ω SST model.

In the Sydney Bluff Body jet case, a double vortex recirculation region is obtained behind the bluff body. Three mixing layers are observed in the recirculation zone [8]. It was found that the smaller vortex near the jet loses the circulation pattern with the increase in the momentum of jet fuel. It was observed from the comparison of the mixture fraction profile with the experimental data that k- ω SST turbulence model, in ANSYS CFX 16.1, over-predicts the mixing slightly in certain locations of the domain. Realizable k- ϵ model, in ANSYS Fluent 17.0, over-predicted the mixing significantly, in certain domain locations, as observed from the mixture fraction comparison plots. Apart from that other turbulence models were in good agreement with each other as well as the experimental data.

Contents

Nomenclature

List of Figures

List of Table

1	Introduction	1
1.1	Literature survey	2
1.2	Objective of the work.....	2
2	Experimental Description.....	4
3	Computational Domain.....	7
4	Turbulence	10
4.1	RANS Models.....	11
4.1.1	Two equation models	12
4.1.1.1	k- ϵ model	13
4.1.1.2	Realizable k- ϵ model	14
4.1.1.3	Standard k- ω model.....	14
4.1.1.4	Shear stress transport model (SST).....	15
4.1.2	Reynolds Stress Models (RSM).....	15
4.1.2.1	Base line reynolds stress ω based (BSLRSM)	15
4.1.2.2	Explicit Algebraic Reynolds stress (EARSM) model.....	17
5	Additional Theories.....	18
5.1	Turbulent Schmidt number (Sc_t)	18
5.2	Round jet anomaly	18
6	Quality Assurance	19
6.1	Iteration Error Study	19
6.2	Spatial discretisation errors	19
6.3	Additional Quality Assurance studies	20
6.3.1	Test of turbulent inlet boundary conditions.....	20
6.3.2	Turbulent Schmidt number study.....	20
6.4	Inspection of the results	21
7	CFD Model setup.....	22

7.1	Boundary conditions	22
7.2	Material properties	22
7.3	Initialization.....	23
7.4	Numerical Settings	23
7.5	Post-Processing	23
8	Results.....	24
8.1	ANSYS CFX 16.1	24
8.1.1	Iteration or Convergence Error	24
8.1.2	Spatial discretization error.....	25
8.1.3	Turbulence inlet boundary condition (TIBC)	28
8.1.4	Turbulent Schmidt number (Sc_t)	30
8.1.5	Model Error Study.....	31
8.2	ANSYS Fluent 17.0.....	34
8.2.1	Model Error Study.....	34
8.3	Solver Comparison between ANSYS CFX 16.1 & ANSYS Fluent 17.0	35
9	Experimental Description.....	40
10	Computational Domain.....	43
11	CFD Model Setup	46
11.1	Boundary conditions	46
11.1.1	Boundary conditions (Flow field)	46
11.1.2	Boundary conditions (Mixing field).....	46
11.2	Material Properties	47
11.2.1	ANSYS CFX 16.1	47
11.2.2	ANSYS Fluent 17.0	47
11.3	Initialization.....	47
11.3.1	ANSYS CFX 16.1	47
11.3.2	ANSYS Fluent 17.0	48
11.4	Numerical Settings	48
11.4.1	ANSYS CFX 16.1	48
11.4.2	ANSYS Fluent 17.0	48
12	Results.....	49
12.1	ANSYS CFX 16.1	49

12.1.1	Iteration Error Study	49
12.1.2	Spatial Discretization Error (Flow field)	50
12.1.3	Spatial Discretization study (Mixing field).....	51
12.1.4	Model Error Study.....	55
12.2	ANSYS Fluent 17.0.....	61
12.2.1	Model Error Study.....	61
12.3	Solver comparison between ANSYS CFX 16.1 and ANSYS Fluent 17.0	66
12.3.1	CNG	67
12.3.1.1	$k-\epsilon$ model.....	67
12.3.1.2	$k-\omega$ SST model	68
13	Conclusions	70
13.1	Sandia Propane jet.....	70
13.2	Sydney Bluff Body	71

References

Appendix

Nomenclature:

English symbols

Symbol	Description	Unit
u_j	Fuel jet velocity (Sandia propane jet)	m/s
u_{co}	Co-flow velocity(Sandia propane jet)	m/s
L_1	Length of fuel jet pipe	m
L	Length of domain	m
L_2	Length of bluff body	m
D	Diameter of jet pipe	m
D_{Coflow}	Diameter of co-flow	m
H	Height of the domain	m
H_B	Height of the bluff body	m
S_{ij}	strain rate tensor	s^{-1}
Pr_t	Turbulent Prandtl number	-
Sc_t	Turbulent Schmidt number	-
k	Turbulent kinetic energy	$m^2 s^{-2}$
U_J	Fuel jet velocity (Sydney Bluff Body)	m/s
D_B	Bluff body diameter (Sydney Bluff Body)	m
R_B	Bluff body radius(Sydney Bluff Body)	m
D_J	Diameter of jet (Sydney Bluff Body)	m
U	Mean axial velocity component	ms^{-1}
V	mean radial velocity component	ms^{-1}
u'	RMS value of u velocity fluctuation	ms^{-1}
v'	RMS value of v velocity fluctuation	ms^{-1}

Greek Symbols

Symbol	Description	Unit
ρ	Density	kg m^{-3}
τ_{ij}	Molecular stress tensor	N/m^2
μ	Dynamic viscosity	$\text{kg m}^{-1}\text{s}^{-1}$
ν	Kinematic viscosity	m^2s^{-1}
ε	Turbulence eddy dissipation	$\text{m}^2 \text{s}^{-3}$
ω	Turbulence eddy frequency	s^{-1}
Γ_t	Turbulent diffusivity	m^2s^{-1}
μ_t	Turbulent viscosity	$\text{kg m}^{-1}\text{s}^{-1}$
δ_{ij}	Kronekar delta	-

List of Figures

Figure	Description
Figure 2.1(a)	Experimental Setup Sandia Propane Jet
Figure 2.1(b)	2D axisymmetric experimental setup for Sandia Propane Jet
Figure 2.1(c)	Measurement locations for Sandia Propane Jet
Figure 3.1(a)	Computational Domain with boundary names for Sandia Propane Jet
Figure 3.1(b)	Visual Comparison of the different mesh resolutions
Figure 8.1(a)	Iteration Error Study comparison profile plots
Figure 8.2(a)-(b)	Residual Convergence history & Imbalance Monitor plots for Mesh 3 & 4, Spatial Discretization Study
Figure 8.2(c)	Radial profiles compared for ANSYS CFX 16.1
Figure 8.2(d)	Monitor residuals for ANSYS CFX 16.1
Figure 8.3(a)-(b)	Turbulent Inlet Boundary condition study for ANSYS CFX 16.1
Figure 8.4(a)-(b)	Turbulent Schmidt number study (Sc_t) for ANSYS CFX 16.1
Figure 8.5(a)-(d)	Comparison of different models for ANSYS CFX 16.1
Figure 8.6(a)	Model Error Study for ANSYS Fluent 17.0
Figure 8.7(a)-(d)	Cross comparison of k- ω SST model of ANSYS CFX 16.1 & ANSYS Fluent 17.0
Figure 8.8(a)-(d)	Cross comparison of k- ϵ model of ANSYS CFX 16.1 & ANSYS Fluent 17.0
Figure 9.1(a)&(b)	Schematic of a burner and 2D axisymmetric schematic of burner and flow field, Sydney Bluff Body
Figure 9.1(c)&(d)	Measurement locations for the flow field data, for data set 1 , data set 2&3 respectively
Figure 10.1(a)&(b)	Full 3D & 2D axisymmetric computational domain respectively for Sydney Bluff Body
Figure 12.1(a)-(d)	Iteration Error study for ANSYS CFX 16.1
Figure 12.2-12.3	Spatial Discretization Study for flow field and mixing field for ANSYS CFX 16.1
Figure 12.4	Model Error Study for ANSYS CFX 16.1
Figure 12.5	Model Error Study for ANSYS Fluent 17.0
Figure 12.6	Cross comparison of different combinations of turbulence models in ANSYS CFX 16.1 and ANSYS Fluent 17.0

List of Tables

Table	Description
Table 1	Test section dimensions and inlet conditions
Table 2	Dimensions of 2d axisymmetric domain
Table 3	Details regarding the number of nodes and quality of mesh for Sandia Propane Jet
Table 4	Classification of RANS models based on number of additional equations used
Table 5	Boundary conditions for the Sandia Propane Jet (both solvers)
Table 6	Array of the simulations carried out for Turbulent Inlet boundary condition study (TIBC) with Sandia Propane Jet
Table 7	Naming convention used in the comparison plots of ANSYS Fluent 17.0
Table 8	Lists of fuels and their velocities as used in the experiments
Table 9	Details regarding the number of nodes and quality of mesh for Sydney Bluff Body
Table 10	Boundary conditions for the Sydney Bluff Body for flow field (both solvers)
Table 11	Boundary conditions for the Sydney Bluff Body for Mixing field (both solvers)
Table 12	Array of simulations for Model error study ANSYS CFX 16.1
Table 13	Array of simulations for Model error study ANSYS Fluent 17.0

1 Introduction

Combustion is one of the most important processes in engineering, which involves turbulent fluid flow, heat transfer, chemical reaction, radiative heat transfer and other complicated physical and chemical processes. Typical engineering applications include internal combustion engines, power station combustors, aero engines, gas turbine combustors, boilers, furnaces, and many other combustion equipments. Combustion is an extremely difficult phenomenon for several reasons. It involves a large number of chemical species and associated chemical reactions. Coupling of the thermo-chemistry with fluid mechanics can be strong, and leads to further complications. In most applications the flows are turbulent, leading to the phenomenon of turbulent combustion, which is the interaction of the two non-linear problems with multiple scales.

Modeling of the turbulent combustion flows has been intensively researched and models are used in the design of several industrial components. Direct numerical simulation (DNS) can be used to resolve all the time and length scales in the turbulent combustion. But large number of degrees of freedom involved in turbulent combustion makes a full DNS of a practical system prohibitively expensive and averaging techniques leading to unclosed equations then become necessary. Apart from that a formidable challenge is placed by the turbulent combustion for the modelers, because of the multitude and complexity of processes which interacts with in such systems. Apart from the above mentioned complexities it also involves other complications in terms of complex geometries and boundary conditions [8].

Development of the numerical models is largely based on the sub-models developed for non-reacting constant density flows. But this poses another challenge in terms of verification of these sub-models, which becomes difficult in the reacting flows due to the turbulent mixing and heat release. According to several authors [20-21], it is not useful to use the sub-models developed for non-reacting constant density flows for reacting flows. This is where the non-reacting variable densities flows come into play. It provides a simplified flow situation in which the complexity of variable density remains without the complex coupling between the turbulent mixing and chemical heat release. This means the variable density effects on the turbulent mixing can be isolated from combustion chemistry [1].

Sandia propane jet experiment is performed with the purpose of providing the data, for preparing a database of non-reacting variable density jets, which becomes useful for the development of numerical models for the turbulent reacting flows. Non-reacting constant and variable density flow data has also been measured in the experiment for Sydney bluff body jet flame for the same purpose [6].

Various approaches have been developed to account for turbulent combustion and the associated heat and density fluctuations. They show a lot of potential in terms of taking in to account all the

complexities and complications associated with the turbulent combustion. But still these models are not applicable to the complex industrial flows.

Efforts are being applied to bridge the gap prevailing in between the “engineering” and “research” type approaches [8]. The example is the Sydney bluff body burner. The geometry of the Sydney Bluff burner is a compromise between the industrial and research. Bluff body flames have a complex recirculation flow pattern like that of the industrial combustor, but with simple and well defined boundary and initial conditions [6]. Hence models are validated first on the simple research based model experiment, which represents the real problem as close as possible, before being applied to the industrial problems.

1.1 Literature survey

Sandia propane jet is the case where non-reacting variable density jet have been used for the experiment, which is considered to be one of the few data's available for non-reacting variable density case. Wild [17] carried out the numerical investigation of the experiment with modified k- ϵ model, $C_{\epsilon 1}$ was changed to 1.6 in dissipation (ϵ) equation, for both reacting and non-reacting case. The results of the non-reacting case in [17] with modified k- ϵ model appear to be same as the results in my case without the modification in k- ϵ model. Briggs Jr. [18] performed the investigation with Large Eddy Simulation (LES) model. No further literature for such validation was obtained.

Sydney bluff body is a typical laboratory flame. A ceramic bluff body, burner, with the 3.6 mm bore, for the fuel flow, is surrounded by the co-flowing air. Dally [7] carried out this validation with modified k- ϵ model for both reacting and non-reacting cases with Ethylene as fuel. Dally [8] carried out the same study with modified k- ϵ and RSM model, for both non-reacting and reacting case with all fuels specified in [6]. Dally [7][8] emphasized the fact that turbulence models are not able to predict the accurate enough flow field, due to well known deficiency and modified the k- ϵ model as done by Wild[17] to obtain the accurate results. Studies performed in my case, involved no RSM model, shows that there is no need for the modification in the standard k- ϵ model. Numerical results, specifically for standard k- ϵ model, were in good agreement with the experimental data for non-reacting case.

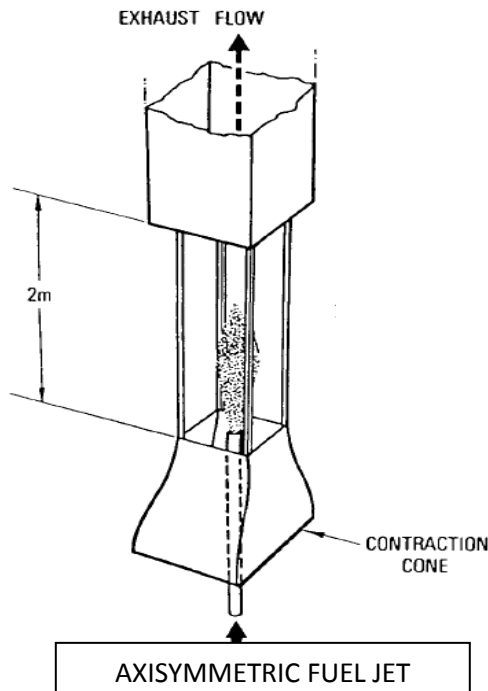
1.2 Objective of the work

The main motivation to carry out these investigations, of Sandia Propane Jet and Sydney Bluff Body, was to obtain a better understanding of the flow structure and mixing process in variable density jets, under non-reacting conditions (also constant density jet flow in case of Sydney Bluff Body). Turbulent mixing in the recirculation zone behind the bluff body is investigated with the different turbulent models of type RANS. These investigations were carried out under non-reacting conditions because the turbulent mixing is decoupled from the complex combustion chemistry and the effects of chemical heat release found in the highly exothermic reacting jets

[1]. This allows us to make appropriate conclusions about the model performance and better address the reasons for the differences appearing to the expected results. Also it is a necessary pre-requisite; to compute the mixing and reactive scalar field, the correct and accurate prediction of the flow and the turbulence field is required [8]. Turbulence models validated in these investigations are available in ANSYS CFX 16.1 and ANSYS Fluent 17.0 software. The simulation results are compared with experimental data [3][6].

2 Experimental Description

The experiment was performed in the Sandia Turbulent Diffusion Flame Facility. A schematic of the experimental setup is shown in Figure 2.1(a). The flow configuration consists of a high-velocity central jet of fuel surrounded by a coflowing airstream. Flow rates are determined from the measured pressure drop across a calibrated venturi meter located upstream of the test section. A honeycomb section located upstream of the contraction cone and a 9:1 area ratio across the contraction cone provide a uniform velocity across the test section entrance with a measured inlet turbulence level of 0.4%. The fuel nozzle is located at the upstream end of the test section and is aligned with the test section centerline. The fuel jet inside diameter D is 5.2 mm with the jet exit preceded by a 2-m length of straight tubing. The test section has a 30-cm square cross section and is 200 cm long. Optical access is provided through the removable glass walls of the test section. The test section and contraction cone are mounted on a traversing mechanism driven by stepping motors to provide positioning in three directions. This allows the optical diagnostics to remain fixed and simplifies the alignment procedure. The propane jet bulk velocity u_j in the present investigation was 53 m/s, giving a Reynolds number based on the jet exit diameter Re of 68,000. The coflowing air velocity u_{co} was 9.2 m/s, giving a ratio of jet to coflow air velocity of 5.76. A boundary layer was also measured along the outer edge of the jet pipe with a thickness of approximately 0.3 jet diameters at the exit plane[2].



Orientation	Vertical
Test Section	30 cm x 30 cm
Jet Tube Exit	0.52 cm (I. D.) 0.90 cm (O. D.)
Length of Fuel Jet Tube	2 m
Prior to Exit	
Propane Jet Velocity	53 m/s (± 0.1 m/s)
Propane Jet Temperature	294 K (± 2 K)
Coflow Air Velocity	9.2 m/s (± 0.1 m/s)
Coflow Air Temperature	294 K (± 2 K)
Reynolds Number (based on jet exit diameter)	68,000
Coflow Air Turbulence	0.4%
Axial Pressure Gradient	6 Pa/m

Figure 2.1(a) & Table 1

The experimental data for the mean and rms mixture fraction was measured using the Rayleigh scattering technique, detailed information about which can be found in [1]. And the measurements for the mean and rms velocity (axial and radial components) has been measured using laser Doppler velocimetry (LDV) twice, once by seeding the jet and once by seeding the co-flow[2].

Figure 2.1(b) shows the 2D axisymmetric experimental setup. The dimensions for the same are mentioned in table below.

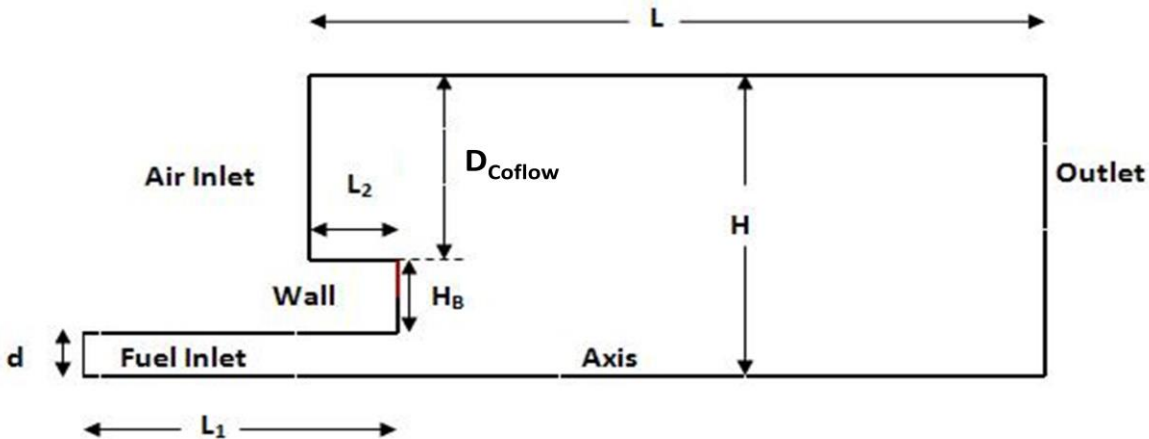


Figure 2.1(b)

Parameter	L	L ₂	d	D _{Coflow}	H _B	H
Values(cm)	30	5	0.26	14.55	0.19	15

Table 2

Characteristic Length and Diameter:

Length of test section	= L
Length of bluff body	= L ₂
Propane jet inlet radius	= d (in reference used as 'D')*
Co-flow air channel width	= D _{Coflow}
Height of the bluff body	= H _B
Height of the test section	= H

*Note: Here $d = 0.26$ [cm] is considered as the radius of the jet for the axisymmetric domain. Consequently the Propane jet diameter D used in the original references for the non-dimensional variables X/D and Y/D is $D = 0.52$ [cm].

Experimental data has been provided for locations $(X/D) = 4, 15, 30, 50$ downstream the jet exit plane. Also the data has been provided for location $y/D = 0$ (centerline), $D = 0.52$ cm (jet exit diameter) is used to normalize the axial and radial locations. The measured flow field quantities are:

1. Mean velocity component (axial & radial), U, V
2. Rms fluctuating velocity components, (u', v')
3. Mean mixture fraction, f
4. Rms fluctuating mixture fraction, f'

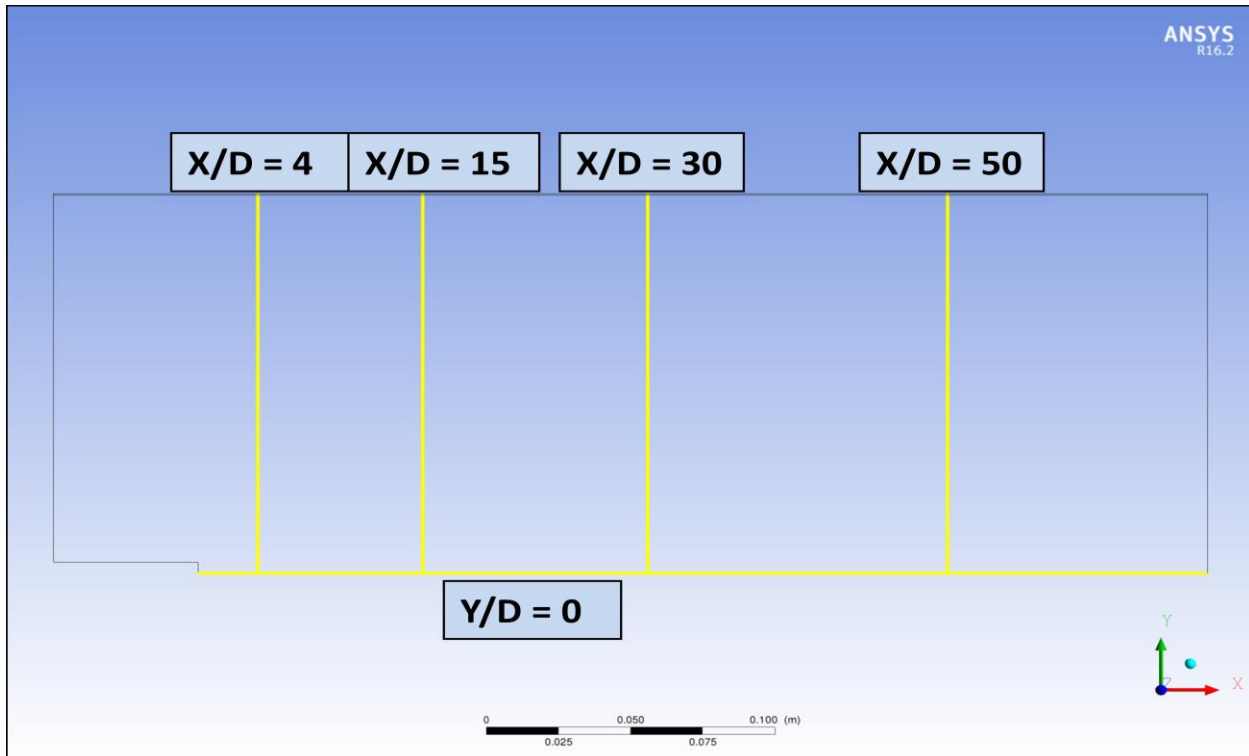


Figure 2.1(c)

3 Computational Domain

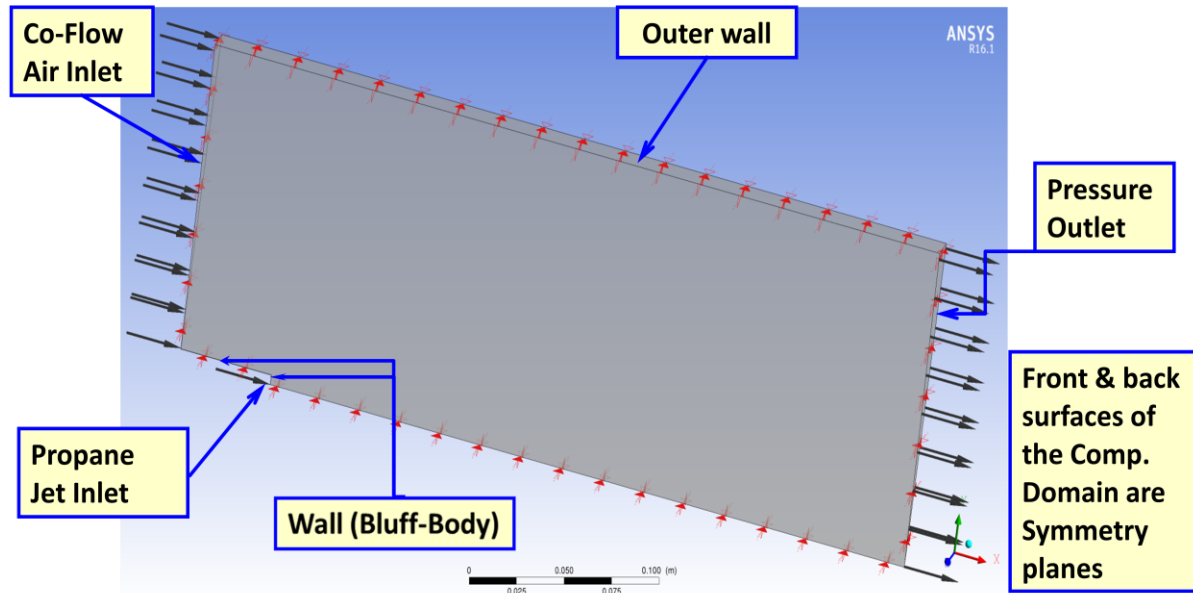


Figure 3.1(a)

Computational domain was chosen to be of axisymmetric type and is generated using ANSYS ICEM CFD 16.1 software. It was meshed with structured, non uniform grid. Since the geometry was a simple one it was meshed using hexahedral elements. Meshing was done using the blocking strategy of ANSYS ICEM CFD software. A block was created covering the entire domain and unnecessary portions of block were removed which allowed the blocks to associate with the respective portions of the geometry. A hierarchy of four, quasi 2D type, meshes was generated with each mesh refined, by a factor half in each direction, compared to their latest coarser mesh.

Initially meshes were generated as 2D radially symmetric meshes, since ANSYS CFX works only with 3D meshes; a small change was made in the meshes. At the time of reading the meshes in to the ANSYS CFX Pre processor, the 2D meshes were extruded by rotating them by 5 degrees in circumferential direction, with one cell in the circumferential direction. Hence a quasi-2D mesh, having hexahedral as well as wedge elements in it, is generated. The expansion ratio of the meshes was controlled to be < 1.2 , in order to have a denser mesh in the region behind the bluff body and in the near field. Mesh was gradually made coarser towards the exit and towards the top as no significant physical changes would be taking place there.

In order to save the unnecessary computation time and resources, fuel jet flow pipe was not considered in the computational domain. Instead a precursor simulation was carried out for the jet inlet pipe. The inflow conditions for the propane jet inlet were provided from the fully developed pipe profile obtained from the precursor simulation of the fuel jet pipe.

The computational domain for the precursor simulation was a thin long pipe, which extended 50D, D=0.52 cm, in the axial direction (X-axis) to have a fully developed pipe flow, as in the experiment [3]. The computational domain for precursor simulation was also of axisymmetric type, with quasi-2D mesh.

Figure 3.1(b) shows the different mesh resolutions to have a visual comparison between them.

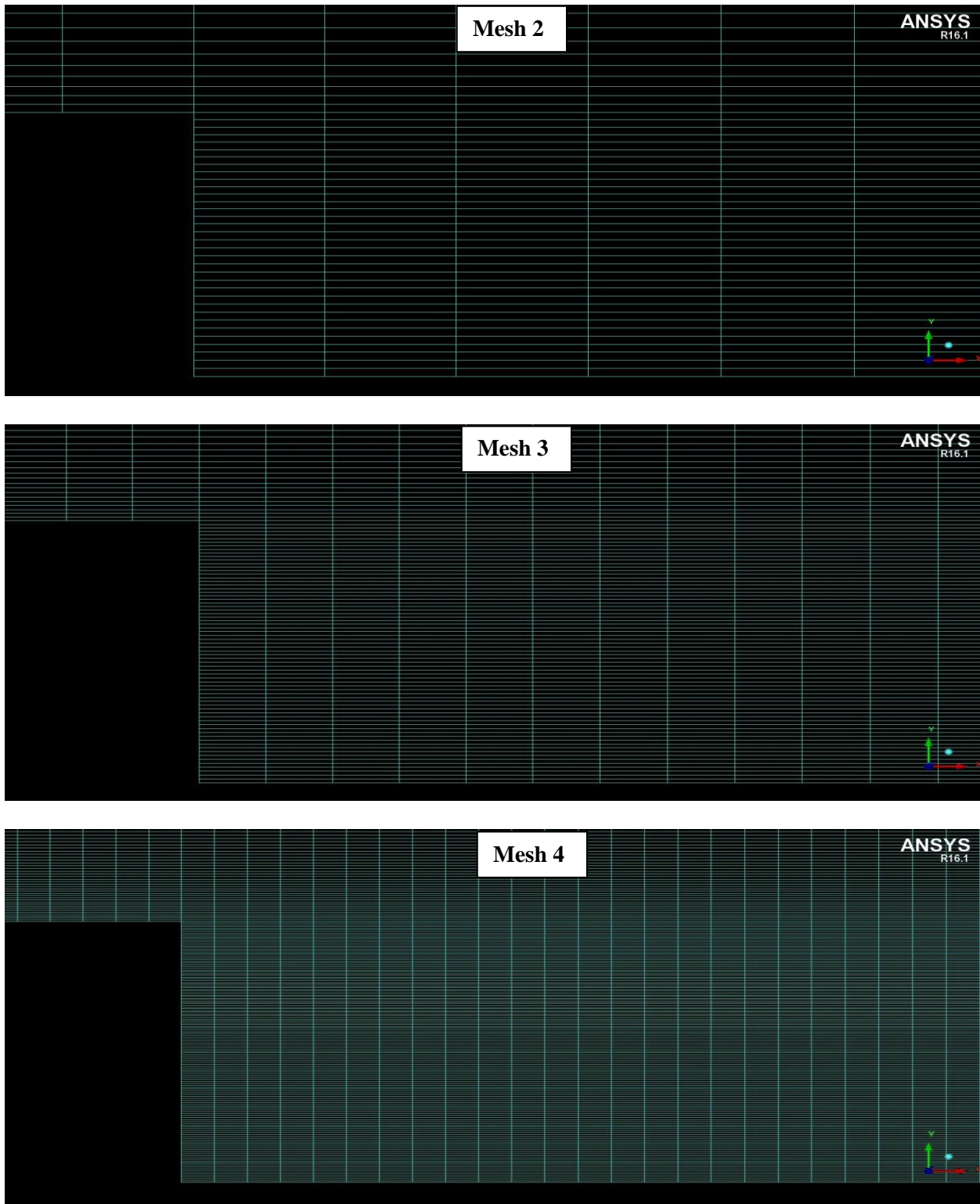


Figure 3.1(b)

The mesh quality plays an important role for the solver to deliver more accurate and faster results. Bad mesh quality can cause the solver to diverge and even deliver inaccurate results. Meshes generated here are of good quality because of the following reasons:

1. The changes in the mesh spacing was continuous over the whole domain, specifically in the region behind the bluff body, where important phenomenon viz. recirculation zone, turbulent mixing between jet and co-flow would take place
2. Aspect ratios in the important regions should be between 20 to 100 as specified in [14]
3. Minimum face angle which should be between ($20 < \text{Min Angle} < 160$) [11]

Table 3 shows the details about the mesh parameters.

Parameter	Mesh 1	Mesh 2	Mesh 3	Mesh 4
Number of nodes	3736	15568	63532	256660
Number of element	7665	31530	127860	514920
Minimum grid angle	90	90	90	90
Maximum aspect ratio	22.57	24.54	25.59	26.52

Table 3

4 Turbulence

Turbulence occurs when the inertia forces in the fluid become significant compared to the viscous forces, and is characterized by the high Reynolds number. Turbulence consists of fluctuations in the flow field in time and space. It is a complex process, mainly because it is three dimensional and unsteady. Rotational flow structures, so called turbulent eddies, with a wide range of length scales are found in turbulent flows. Large turbulent eddies transfer the energy to the small eddies and the small eddies in turn dissipate the energy into thermal energy because of the action of viscous stresses.

In principle Navier-Stokes equations describe both laminar and turbulent flows without the need for additional information. But performing the calculations directly by solving these equations makes this approach, computationally, a lot expensive. An alternative approach to the approach mentioned before would be to have, some mathematical models, turbulence models which can account for all the effects of turbulence without the requirements of fine mesh and avoid solving the navier-stokes equation directly.

The following are the categories of turbulence models:

- i. RANS (Reynolds averaged navier stokes equation) :

Here the attention is focused on the mean flow and the effects of turbulence on mean flow properties. Prior to the application of numerical methods the Navier–Stokes equations are time averaged (or ensemble averaged in flows with time-dependent boundary conditions). Extra terms appear in the time-averaged (or Reynolds averaged) flow equations due to the interactions between various turbulent fluctuations. These extra terms are modeled with classical turbulence models: among the best known ones are the $k-\epsilon$ model and the Reynolds stress model. The computing resources required for reasonably accurate flow computations are modest, so this approach has been the mainstay of engineering flow calculations over the last three decades.

- ii. LES (Large Eddy Simulation):

This is an intermediate form of turbulence calculations which tracks the behavior of the larger eddies. The method involves space filtering of the unsteady Navier–Stokes equations prior to the computations, which passes the larger eddies and rejects the smaller eddies. The effects on the resolved flow (mean flow plus large eddies) due to the smallest, unresolved eddies are included by means of a so-called sub-grid scale model. Unsteady flow equations must be solved, so the demands on computing resources in terms of storage and volume of calculations are large, but (at the time of writing) this technique is starting to address CFD problems with complex geometry.

- iii. DNS (Direct Numerical Simulation):

In this method the simulations compute the mean flow and all turbulent velocity fluctuations. The unsteady Navier–Stokes equations are solved on spatial grids that are

sufficiently fine that they can resolve the Kolmogorov length scales at which energy dissipation takes place and with time steps sufficiently small to resolve the period of the fastest fluctuations. These calculations are highly costly in terms of computing resources, so the method is not used for industrial flow computations [10].

4.1 RANS Models

The continuity and the momentum equations are described as follows:

$$\frac{\partial \rho}{\partial t} + \frac{\partial}{\partial x_j} (\rho U_j) = 0 \quad (4.1)$$

$$\frac{\partial \rho U_i}{\partial t} + \frac{\partial}{\partial x} (\rho U_i U_j) = - \frac{\partial p}{\partial x_i} + \frac{\partial}{\partial x_j} (\tau_{ij}) + S_M \quad (4.2)$$

$$\tau_{ij} = \mu \left(\left(\frac{\partial U_i}{\partial x_j} + \frac{\partial U_j}{\partial x_i} \right) - \frac{2}{3} \delta_{ij} \frac{\partial U_k}{\partial x_k} \right)$$

where, τ_{ij} is the molecular stress tensor, S_M is the momentum source term

When the time scales, which are much larger than the time scales of turbulent fluctuations, are considered the turbulent flow is said to exhibit the average characteristics, but with an additional time-varying and fluctuating component i.e. velocity component may be divided in to an average and a time varying component

$$U = \bar{U}_i + u' \quad (4.3)$$

where the averaged component is given by:

$$\bar{U}_i = \frac{1}{\Delta t} \int_t^{t+\Delta t} U_i dt \quad (4.4)$$

Substituting the averaged quantities, eq (4.3), in the original transport equations, eq (4.1) - (4.2), results in the Reynolds averaged equations given below. In the following equations, the bar is dropped for averaged quantities, except for products of fluctuating quantities:

$$\frac{\partial \rho}{\partial t} + \frac{\partial}{\partial x_j} (\rho U_j) = 0 \quad (4.5)$$

$$\frac{\partial \rho U_i}{\partial t} + \frac{\partial}{\partial x} (\rho U_i U_j) = - \frac{\partial p}{\partial x_i} + \frac{\partial}{\partial x_j} (\tau_{ij} - \rho \bar{u}_i \bar{u}_j) + S_M \quad (4.6)$$

The continuity equation has not been altered but the momentum equation has additional turbulent flux terms in addition to the molecular diffusive fluxes. These terms - $\rho \bar{u}_i \bar{u}_j$ are the Reynolds stresses. They have to be modeled by additional equations of known quantities in order to achieve “closure”. Closure

means that there should be sufficient number of equations for all the unknowns, including the unknowns which appear from the averaging equations.

The most common RANS turbulent models are classified depending on the number of additional equations that are required to be solved along with the averaged transport equations [10]:

No. of additional transport equations	Name
Zero	Mixing length model
One	Spalart-Allmaras model
	k- ϵ
Two	k- ω
	Algebraic stress model
Seven	Reynolds stress model

Table 4

4.1.1 Two equation models

A proposal from boussinesq in 1877 suggested that the reynolds stresses can be related to the mean velocity gradients and turbulent viscosity by the gradient diffusion hypothesis, in a manner analogous to the relationship between the stress and strain tensors in laminar newtonian flow:

$$-\rho \overline{u_i u_j} = \mu_t \left(\left(\frac{\partial U_i}{\partial x_j} + \frac{\partial U_j}{\partial x_i} \right) - \frac{2}{3} \delta_{ij} \left(\rho k + \mu_t \frac{\partial U_k}{\partial x_k} \right) \right) \quad (4.7)$$

where μ_t is the turbulent viscosity which must be modeled and k is the turbulent kinetic energy defined as:

$$k = \frac{1}{2} (\overline{u'}^2 + \overline{v'}^2 + \overline{w'}^2) \quad (4.8)$$

In the equation stating the boussinesq hypothesis oben, δ_{ij} indicates that only the normal components of reynolds stresses will be considered. This implies an isotropic assumption for the normal reynolds stresses. Analogus to the turbulent viscosity hypothesis is the turbulent diffusivity hypothesis, which states that the Reynolds fluxes of a scalar are linearly related to the mean scalar gradient.

$$-\rho \overline{u_i \varphi} = \Gamma_t \frac{\partial \varphi}{\partial x_i} \quad (4.9)$$

where Γ_t is defined as the turbulent diffusivity and it is written as,

$$\Gamma_t = \frac{\mu_t}{Pr_t} \quad (4.10)$$

Or

$$\Gamma_t = \frac{\mu_t}{Sc_t} \quad (4.11)$$

where Pr_t and Sc_t are the turbulence Prantl and Schmidt number respectively

Applying the hypothesis, eq (4.7), to the averaged momentum equation, eq (4.6), becomes:

$$\frac{\partial \rho U_i}{\partial t} + \frac{\partial}{\partial x} (\rho U_i U_j) = - \frac{\partial p'}{\partial x_i} + \frac{\partial}{\partial x_j} \left[\mu_{eff} \left(\frac{\partial U_i}{\partial x_j} + \frac{\partial U_j}{\partial x_i} \right) \right] + S_M \quad (4.12)$$

$$\mu_{eff} = \mu + \mu_t \quad (4.13)$$

$$p' = p + \frac{2}{3} \rho k + \frac{2}{3} \mu_{eff} \frac{\partial U_k}{\partial x_k} \quad (4.14)$$

Similary the scalar transport equations are written as :

$$\frac{\partial(\rho\Phi)}{\partial x} + \frac{\partial(\rho U\Phi)}{\partial x_j} = \frac{\partial}{\partial x_j} \left[\left(\Gamma_\Phi + \frac{\mu_t}{\sigma_\Phi} \right) \frac{\partial\Phi}{\partial x_j} \right] + S_\phi \quad (4.15)$$

4.1.1.1 k- ϵ model

This model uses two additional equations, in the form of turbulence kinetic energy (k) m^2/s^2 and turbulence eddy dissipation (ϵ) m^2/s^3 , defined as the rate at which the velocity fluctuations dissipate. This model uses the assumption, that the turbulence viscosity is linked to the turbulence kinetic energy and dissipation via the relation:

$$\mu_t = C_\mu \rho \frac{k^2}{\epsilon} \quad (4.16)$$

where C_μ is the dimensionless constant.

The transport equations for the k and ϵ , which are obtained by performing certain algebraic manipulations, are shown below:

$$\frac{\partial \rho k}{\partial t} + \frac{\partial}{\partial x} (\rho U_j k) = \frac{\partial}{\partial x_j} \left[\left(\mu + \frac{\mu_t}{\sigma_k} \right) \frac{\partial k}{\partial x_j} \right] + P_k - \rho \epsilon + P_{kb} \quad (4.17)$$

$$\frac{\partial(\rho \epsilon)}{\partial t} + \frac{\partial}{\partial x} (\rho U_j \epsilon) = \frac{\partial}{\partial x_j} \left[\left(\mu + \frac{\mu_t}{\sigma_\epsilon} \right) \frac{\partial \epsilon}{\partial x_j} \right] + \frac{\epsilon}{k} (C_{\epsilon 1} P_k - C_{\epsilon 2} \rho \epsilon + C_{\epsilon 1} P_{\epsilon b}) \quad (4.18)$$

where $C_{\epsilon 1}$, $C_{\epsilon 2}$, σ_k , and σ_ϵ are constants. P_k is the turbulence production term due to the viscous forces. P_{kb} and $P_{\epsilon b}$ represent the influence of the buoyancy forces.

This model does not perform well in the weak shear layers and the spreading rate of the axisymmetric jets in stagnant surroundings is severely over-predicted. Such difficulties can be overcome by modifying the model constant C in eq (4.18). Since this model is based on the boussinesq's assumption, of isotropic eddy viscosity, it delivers poor performance in flows with swirl, with curved boundary layers.

4.1.1.2 Realizable k- ε model

Realizable k- ε model aims to improve the limitations of the standard k- ε model, in certain flow types viz. flows with high strain rates. The formulation of this model differs from the standard k- ε model in the following aspects:

New eddy-viscosity formula, involving a variable C_μ , which was originally proposed by reynolds [13]. New model equation for the dissipation (ε) based on the dynamic equation of the mean-square vorticity fluctuation

The realizability here implies positivity of the normal stresses and fullfilling the Schwarz inequality for the shear stresses [13]. It is achieved by the first aspect of the realizable k- ε model. This reliability is only achieved by the realizable k- ε model and not by the other, previously discussed, types of k- ε model.

The two equations for k and ε for this model are as shown below:

$$\frac{\partial \rho k}{\partial t} + \frac{\partial}{\partial x} (\rho U_j k) = \frac{\partial}{\partial x_j} \left[\left(\mu + \frac{\mu_t}{\sigma_k} \right) \frac{\partial k}{\partial x_j} \right] + G_k - \rho \varepsilon + G_b \quad (4.19)$$

$$\frac{\partial(\rho \varepsilon)}{\partial t} + \frac{\partial}{\partial x} (\rho U_j \varepsilon) = \frac{\partial}{\partial x_j} \left[\left(\mu + \frac{\mu_t}{\sigma_\varepsilon} \right) \frac{\partial \varepsilon}{\partial x_j} \right] + \rho C_1 S \varepsilon + - \rho C_2 \frac{\varepsilon^2}{k + \sqrt{v \varepsilon}} + C_{1\varepsilon} \frac{\varepsilon}{k} C_{3\varepsilon} G_b \quad (4.20)$$

where $C_1 = \max \left[0.43, \frac{\eta}{\eta+5} \right]$, $\eta = S \frac{k}{\varepsilon}$, $S = \sqrt{2S_{ij}S_{ij}}$, G_k represents the production of the turbulent kinetic energy, G_b is the generation of turbulence kinetic energy due to buoyancy. One limitation of this model is that it produces non-physical turbulent viscosities in situations where the rotating and stationary fluid zones exist.

4.1.1.3 Standard k- ω model

This model does not require complex non-linear damping function, as required in the k- ε model, which makes it more robust and accurate. This model assumes that the turbulent viscosity is associated with the turbulence kinetic energy and turbulence frequency via the relation :

$$\mu_t = \rho \frac{k}{\omega} \quad (4.21)$$

In this model the two equations used are turbulence kinetic energy (k) and turbulence eddy frequency (ω) respectively:

$$\frac{\partial \rho k}{\partial t} + \frac{\partial}{\partial x} (\rho U_j k) = \frac{\partial}{\partial x_j} \left[\left(\mu + \frac{\mu_t}{\sigma_k} \right) \frac{\partial k}{\partial x_j} \right] + P_k - \beta' \rho k \omega + P_{kb} \quad (4.22)$$

$$\frac{\partial(\rho \omega)}{\partial t} + \frac{\partial}{\partial x} (\rho U_j \omega) = \frac{\partial}{\partial x_j} \left[\left(\mu + \frac{\mu_t}{\sigma_\omega} \right) \frac{\partial \omega}{\partial x_j} \right] + \alpha \frac{\omega}{k} P_k - \beta \rho \omega^2 + P_{\omega b} \quad (4.23)$$

β' , α , β , σ_k and σ_ω are constants

The problem with this model is its strong sensitivity towards the free-stream condition. Also depending on the value of ω at inlet, a significant variation in the results was obtained and which was not desirable in case of external aerodynamics and aerospace [12].

4.1.1.4 Shear stress transport model (SST)

Considering the better performance of $k-\epsilon$ model in the free stream and better performance of the standard $k-\omega$ model in the near wall region it was suggested in the literature [22] to have an hybrid model:

- i. Transformation of the $k-\epsilon$ model to $k-\omega$ model in the near wall region
- ii. Standard $k-\epsilon$ model in the fully turbulent region far from the wall

In this model a series of modifications have been suggested by Menter [22] in order to optimize the performance of the SST model. It included modification in the model constants, Blending functions and proper limiters. Blending function was implemented in such a fashion that in the near wall region it turned to 1, means $k-\omega$ is activated there, and 0 in the free stream region, means $k-\epsilon$ model is activated there.

4.1.2 Reynolds Stress Models (RSM)

These models do not use the boussinesq's hypothesis, but solves the transport equations for each and every reyolds stress component. They are based on solving of all the stress component equations along with the dissipation equation. Exact production term and modelling of stress anisotropies makes these models suited to more complex flows. But they are not always good compared to the two equation model [10].

Reynolds Stress Models are considered to be the 'simplest' type of model with the potential to describe all the mean flow properties and Reynolds stresses without case-by-case adjustment. Apart from that, model is known for its large computing costs i.e. solving seven extra PDE's (3D) and five (2D). Models face the problem in converging for e.g. in flows with axisymmetric jets and unconfined recirculating flows

4.1.2.1 Base line reynolds stress ω based (BSLRSM)

In this model Omega and BSL reynolds stress model are related wih each other. The reynolds stress – ω model is the reynolds stress model based on the ω -equation [12]. The advantage of the ω based formulation here is a better near wall treatment.

The modeled equation for the reynolds stresses is as follows:

$$\frac{\partial \rho \overline{u_i u_j}}{\partial t} + \frac{\partial}{\partial x} (U_j \rho \overline{u_i u_j}) = P_{ij} - \frac{2}{3} \beta' \rho \omega k \delta_{ij} + \Phi_{ij} + P_{ij,b} + \frac{\partial}{\partial x_k} \left[\left(\mu + \frac{\mu_t}{\sigma_k} \right) \frac{\partial \overline{u_i u_j}}{\partial x_k} \right] \quad (4.24)$$

Here $\overline{u_i u_j}$ indicates the reynolds stresses, P_{ij} and $P_{ij,b}$ indicate the shear and bouyancy turbulence production terms of the reynolds stresses respectively, Φ_{ij} is the pressure strain tensor.

The Omega reynolds stress model

$$\frac{\partial \rho \omega}{\partial t} + \frac{\partial}{\partial x_k} (U_k \rho \omega) = \alpha \rho \frac{\omega}{k} P_k + P_{\omega b} - \beta \rho \omega^2 + \frac{\partial}{\partial x_j} \left[\left(\mu + \frac{\mu_t}{\sigma_k} \right) \frac{\partial \omega}{\partial x_j} \right] \quad (4.25)$$

where $\sigma^* = 2$, $\sigma = 2$, $\beta = 0.075$, $\alpha = \frac{\beta}{\beta'} - \frac{k^2}{\sigma(\beta)^{0.5}} = \frac{5}{9}$ are all defined as constants

The BSL Reynolds stress model

The coefficients α and β of the ω -equation, as well as both the turbulent Prandtl numbers σ^* and σ , are blended between values from the two sets of constants, corresponding to the ω -based model constants and the ε -based model constants transformed to an ω -formulation:

$$\begin{aligned} \frac{\partial \rho \omega}{\partial t} + \frac{\partial}{\partial x_k} (U_k \rho \omega) &= \alpha_3 \frac{\omega}{k} P_k + P_{\omega b} - \beta_3 \rho \omega^2 + \frac{\partial}{\partial x_k} \left[\left(\mu + \frac{\mu_t}{\sigma_{\omega 3}} \right) \frac{\partial \omega}{\partial x_k} \right] \\ &\quad + (1 - F_1) 2 \rho \frac{1}{\sigma_2 \omega} \frac{\partial k}{\partial x_k} \frac{\partial \omega}{\partial x_k} \end{aligned} \quad (4.26)$$

There are two set of constants for the ω -zone and ε -zone:

Set 1 (SMC ω -zone):

$$\sigma_1^* = 2, \sigma_1 = 2, \beta_1 = 0.075, \alpha_1 = \frac{\beta}{\beta'} - \frac{k^2}{\sigma(\beta)^{0.5}} = 0.553$$

The values of β correspond to the value from $k - \omega$ model.

Set 2 (SMC ε -zone):

$$\sigma_2^* = 1.0, \sigma_2 = 0.856, \beta_2 = 0.0828, \alpha_2 = \frac{\beta}{\beta'} - \frac{k^2}{\sigma(\beta)^{0.5}} = 0.44$$

The blending of the coefficients is done by the following equation:

$$\Phi_3 = F \cdot \Phi_1 + (1 - F) \Phi_2 \quad (4.27)$$

where $F = \tanh(\arg^4)$

$$arg = \min \left\{ \max \left(\frac{\sqrt{k}}{\beta' \omega y}, \frac{500v}{y^2 \omega} \right), \frac{4\rho k}{CD_{k\omega} \sigma_{k-\varepsilon} y^2} \right\}$$

and

$$CD_{k\omega} = \max \left(2\rho \frac{1}{\sigma_{k-\varepsilon} \omega} \frac{\partial k}{\partial x_j} \frac{\partial \omega}{\partial x_j}, 10^{-10} \right) \quad (4.28)$$

4.1.2.2 Explicit Algebraic Reynolds stress (EARSM) model

Explicit Algebraic Reynolds stress models (EARSM) represent an extension of the standard two-equation models. They are derived from the Reynolds stress transport equations and give a nonlinear relation between the Reynolds stresses and the mean strain-rate and vorticity tensors. Due to the higher order terms, many flow phenomena are included in the model without the need to solve transport equations. The EARSM enables an extension of the current ($k - \varepsilon$ and BSL) turbulence models to capture the following flow effects [12]:

- Secondary flows
- Flows with streamline curvature and system rotation

In calculations the EARSM formulation was used with the BSL model (BSL EARSM).

5 Additional Theories

5.1 Turbulent Schmidt number (Sc_t)

For a multi-component fluid, scalar transport equations, ref Eq (4.15) , are solved for velocity, pressure, temperature and other quantities of the fluid. However, additional equations must be solved to determine how the components of the fluid viz. propane mass fraction and other species are transported within the fluid. The additional turbulent transport equations which are solved for the components of fluid are of the form:

$$\frac{\partial(\rho\varphi)}{\partial x} + \nabla \cdot (\rho U \varphi) = \nabla \cdot \left(\left(\rho D_\Phi + \frac{\mu_t}{Sc_t} \right) \nabla \varphi \right) + S_\varphi \quad (5.1)$$

where,

- U is the fluid velocity
- ρ is the mixture density, mass per unit volume
- Φ is the conserved quantity per unit volume, or concentration
- $\varphi = \Phi/\rho$, is the conserved quantity per unit mass
- S_φ is a volumetric source term, with units of conserved quantity per unit volume per unit time
- Sc_t is the Turbulent Schmidt number
- D_Φ is the kinematic diffusivity for the scalar

Since the turbulent transport of momentum, heat or mass is due to the same mechanism – eddy mixing - we expect that the value of the turbulent diffusivity Γ_t is fairly close to that of the turbulent viscosity μ_t . This assumption is known as Reynolds analogy [10].Hence turbulent diffusivity is expressed by $\Gamma_t = \frac{\mu_t}{Sc_t}$. The molecular diffusion term is expressed by $\Gamma_i = \rho D_\Phi$.

Turbulent diffusivity is added to the molecular diffusivity, but the time scale at which the molecular diffusion occurs is different from that in the diffusion of momentum (viscosity), thus Sc_t is introduced as a proportionality factor for the turbulent diffusivity. Generally the value of Sc_t is found between 0.7 - 0.9 in most CFD software's [23].

5.2 Round jet anomaly

The standard k- ϵ model with the standard coefficients delivers the velocity field quite accurately in two-dimensional plane jet, but large errors occur for the axisymmetric jets. Specifically, the spreading rate of round jet is overestimated by 40% [5]. The reason for this “round jet/ plane jet anomaly” is the considered mainly due to the modeled dissipation (ϵ) equation, refer eq (4.18). Several modifications of constants, in the dissipation equation, have been suggested in the literature by Pope [5]. This shows the non-universality of turbulence [4].

6 Quality Assurance

In this section the descriptions are provided for the different conducted studies with which we can assure the correctness of the results available from the simulations

6.1 Iteration Error Study

These errors occur due to the difference between a fully converged solution of a finite number of grid points and a solution that has not fully achieved convergence. Discretized equations are iteratively solved. It is expected that progressively better estimates of the solution are generated as the iteration step proceeds and ideally satisfies the imposed boundary conditions and equations in each local grid cell and globally over the whole domain. However, if the iterative process is terminated prematurely then errors arise. Convergence errors therefore can occur because of either being impatient to allow the solution algorithm to complete its progress to the final converged solution or applying too large convergence tolerances (criterion) to halt the iteration process when the CFD solution may still be considerably far from its converged state. MAX is the residual type chosen to specify the value for the convergence target. MAX Residuals were monitored after every iteration to check whether they reach the specified convergence target. To avoid such type of errors calculations were performed with MAX Residual $< 10^{-3}$ to 10^{-6} and compared with each other and corresponding experimental data.

6.2 Spatial discretisation errors

After the iteration or convergence error is taken care of the numerical errors arising will be concerning the spatial discretisation error. If not taken care of they have a tendency to accumulate through computational processes that may yield unphysical CFD solutions. Hence controlling it will be a crucial step towards obtaining a reliable and meaningful CFD solution.

Spatial discretisation errors are primarily concerned with the approximations of convective terms of the governing transport equations. These errors occur due to the difference between the exact solution of the modeled equations and a numerical solution with a limited spatial resolution. They arise because an exact solution to the equation being solved is not obtained, but numerically approximated. This phenomenon of approximation is termed as differencing scheme and the accuracy of this scheme depends on the form of the algebraic relationship and also on the location of participating grid points (Stencils). As an example of the Taylor series expansion is shown for accuracy of 1st order

$$\left(\frac{\partial \phi}{\partial x} \right) = \frac{\phi_{i+1,j} - \phi_{i,j}}{\Delta x} + O(\Delta x) \quad (6.1)$$

where $O(\Delta x)$ is called the truncation error.

The formulation $O(\Delta x^2)$ has the truncation error of order 2 and is therefore second order accurate and so on in the fashion $O(\Delta x^n)$. Halving the elements using the first order scheme will reduce the numerical error by a factor 2 and halving it for the second error scheme will reduce the numerical error by a factor 4. Thus by reducing the number of cells in the grid can reduce the numerical error.

This study was performed to achieve grid independence, which means that the grid needs to be refined by increasing the number of grid points until a solution is achieved where no significant

changes in the results occur. This indicates that the discretisation error is reduced to an acceptable error and grid independence is reached. In order to achieve that a hierarchy of 4 meshes have been prepared, by doubling the number of mesh elements, in both direction, per level.

6.3 Additional Quality Assurance studies

6.3.1 Test of turbulent inlet boundary conditions

This test was performed to check, whether using some different turbulent inlet boundary conditions, apart from turbulent kinetic energy (K), turbulent dissipation (ϵ) and turbulent eddy frequency (ω) obtained from the interpolated fully developed flow profile at the jet exit plane, improves the comparison with experimental data or not. Also the reason to perform this test was improper documentation of the boundary conditions in literature. In this test turbulent kinetic energy (k) and length scale were used as the turbulent inlet boundary condition for both fuel jet and co-flow inlet. The famous round jet anomaly phenomenon was also addressed in this study, in terms of modification of coefficient $C_{\epsilon 1}$ of the turbulent dissipation (ϵ) equation in standard $k-\epsilon$ model. At co-flow inlet the inflow conditions were provided with an inlet flow profile, obtained from the experimental measurements. Turbulent kinetic energy was calculated for both co-flow and jet inlet, refer eq (4.8), using the experimental data available at the location $X/D = 0$ and $X/D = 4$ respectively. For the length scales it was assumed equal to one tenth of the diameter of the respective inlets.

For the purpose of comparison, two new non-dimensionalised quantities were introduced to compare the jet spread and velocity decay.

Velocity u invariant (U invar)

$$\left(\frac{U_{cl} - U_{air}}{Velocity\ u - U_{air}} \right) \quad (6.2)$$

where, U_{cl} is the centerline velocity, U_{air} is the constant velocity of co-flow air 9.2 m/s, *velocity u* is the result obtained from the numerical calculation.

Propane mass fraction invariant (PMF invar)

$$\left(\frac{1}{Propane\ mass\ fraction} \right) \quad (6.3)$$

6.3.2 Turbulent Schmidt number study

This study was conducted to check the sensitivity of the jet towards the Sc_t number and to identify which number predicts the results closest to the real flow. Simulations were performed with the sequence of Sc_t numbers ranging from 0.6-0.9 with mesh 4 resolution and $K-\omega$ SST model and the results were compared with the experimental data.

6.4 Inspection of the results

Along with the convergence target a separate parameter called conservation target was monitored to decide upon the convergence of the simulation. Conservation target can be further understood as the global imbalances over the entire domain for the conserved quantities i.e. mass, momentum etc. Conservation target is specified as a single value and each conserved quantity has to achieve that value. Further information can be found under [12]

Monitoring points were placed in the domain at the specific locations to track how the flow progresses i.e. when does the mass fraction of fuel reach at a certain location and at what number iteration. At every monitoring point the concentration of various species, velocity components, turbulence quantities etc is tracked. Also looking at the monitoring points we can confirm whether any physical changes are occurring in the domain or not.

7 CFD Model setup

7.1 Boundary conditions

Precursor simulation was carried out with normal velocity of 53 m/s at the inlet [3], average static pressure = 0 Pa at outlet, outer wall defined as no slip wall, symmetry 1&2 defined as symmetry. The propane jet inflow conditions were provided by a precursor simulation of the fully developed pipe flow profile of the propane jet inlet pipe. The inflow conditions for the co-flow air inlet were also provided with an inlet flow profile, obtained from the experimental measurements. The fully developed flow profile for propane jet inlet included the flow variables velocity u, v, and w along with turbulence quantities k, ω and ε . For co-flow inlet the profile the flow quantities velocity u, v and w were provided. Turbulent inlet boundary conditions for co-flow inlet were taken, as Fractional Intensity = 5%, Eddy viscosity ratio = 10, as per mentioned in the literature [3]

Boundary	ANSYS CFX	ANSYS Fluent
Co-flow inlet	Cartesian velocity components provided from Inlet profile Turbulence Intensity = 5% Eddy viscosity ratio = 10	Cartesian velocity components provided from Inlet profile Turbulence Intensity = 5% Eddy viscosity ratio = 10
Jet inlet	Cartesian velocity components along with turbulence inlet boundary condition provided from the fully developed flow profile	Cartesian velocity components along with turbulence inlet boundary condition provided from the fully developed flow profile
Bluff body	No slip wall	No slip wall
Symmetry 1 & 2	Symmetry	Symmetry
Outer wall	Free slip wall	Free slip wall
Outlet	Avg. static pressure = 0 Pa	Gauge pressure = 0 Pa

Table 5

7.2 Material properties

Pure propane was used as fuel in the precursor simulation. Pure propane is injected in to the domain through the jet inlet and air at constant velocity flows through co-flow inlet. Here air is used as a mixture comprising of Ar (1.28 %), O₂ (23.18%), N₂ (75.53%), CO₂ (0.0035%) of gas phase combustion material. For this investigation a mixture has been created with propane and above mentioned gases which constitute air, defined as a variable composition mixture. N₂ is defined as a constraint [12]. Kinematic diffusivity has been defined same for all the species of mixture = 1.2045×10^{-5} m²/s obtained from [16]. Mass fraction of propane was defined as 1 and for others to be 0 at jet inlet.

7.3 Initialization

Before starting the solver to compute, initialization of all the solution variables is a pre-requisite. A realistic initial guess improves solution stability and accelerates convergence. Poor initial guess may cause the solver to even fail during the first few iterations.

ANSYS CFX 16.1

In order to have the identical experimental conditions in the simulation it was decided to initially fill the domain with air. Global initialization [12] option was used. Velocity was specified in terms of all three components velocity $u = 9.2$ m/s, v and $w = 0$ m/s. Static pressure and turbulence boundary conditions were chosen to be of default solver value. The mass fractions of the species were only specified for all the gases which constitute air, except propane.

ANSYS Fluent 17.0

In fluent no such option as in CFX is available for initialization. Rather initialization was done using the option called hybrid initialization [13]. This is the default initialization method in Fluent which provides a quick approximation of the flow field, by a collection of methods.

7.4 Numerical Settings

ANSYS CFX 16.1

The advection scheme and the turbulent numerics were chosen to be of High Resolution method [12]. Time scale for all the simulations was chosen to be Auto Timescale, which is the default option available in ANSYS CFX 16.1. Auto timescale control is a fluid timescale control option which uses an internally calculated physical time scale based on the boundary conditions, flow conditions, physics and domain geometry [12]. The residual type MAX (maximum) with the target of 10^{-5} was chosen as the convergence target and conservation target of 10^{-3} . The maximum number of iterations for all simulations was chosen to be 500.

ANSYS Fluent 17.0

Flow analysis chosen here is of steady state type with pressure-based [13] solver. In all simulations Coupled method [13] is chosen for the pressure-velocity coupling. The gradient approximation is done by Least Squares Cell Based method [13]. For pressure PRESTO [13] method has been used. For momentum second order upwind scheme is used. Turbulent numerics have been approximated by using the First order upwind scheme. For all the species transport again a second order upwind scheme is used. Pseudo transient and higher order term relaxation [13] has also been selected. The residual type RMS (Root mean square) with a target of 1e-07 is selected for each solution variable. Time step method was chosen to be automatic with 500 as the maximum number of iterations for all the simulations

7.5 Post-Processing

Post-processing of the results have been carried in ANSYS CFD Post 16.1 using the pearl scripts and gnuplot scripts, for plotting the data extracted from CFD Post for comparison with the experimental data and for creating various images.

8 Results

8.1 ANSYS CFX 16.1

8.1.1 Iteration or Convergence Error

The results shown here are calculated on mesh 2 resolution with sequence of convergence targets MAX Residuals $< 10^{-3}$ to 10^{-6} . Propane mass fraction, velocity u and v profiles were compared with experimental data. Here the results are only shown for location X/D = 15.

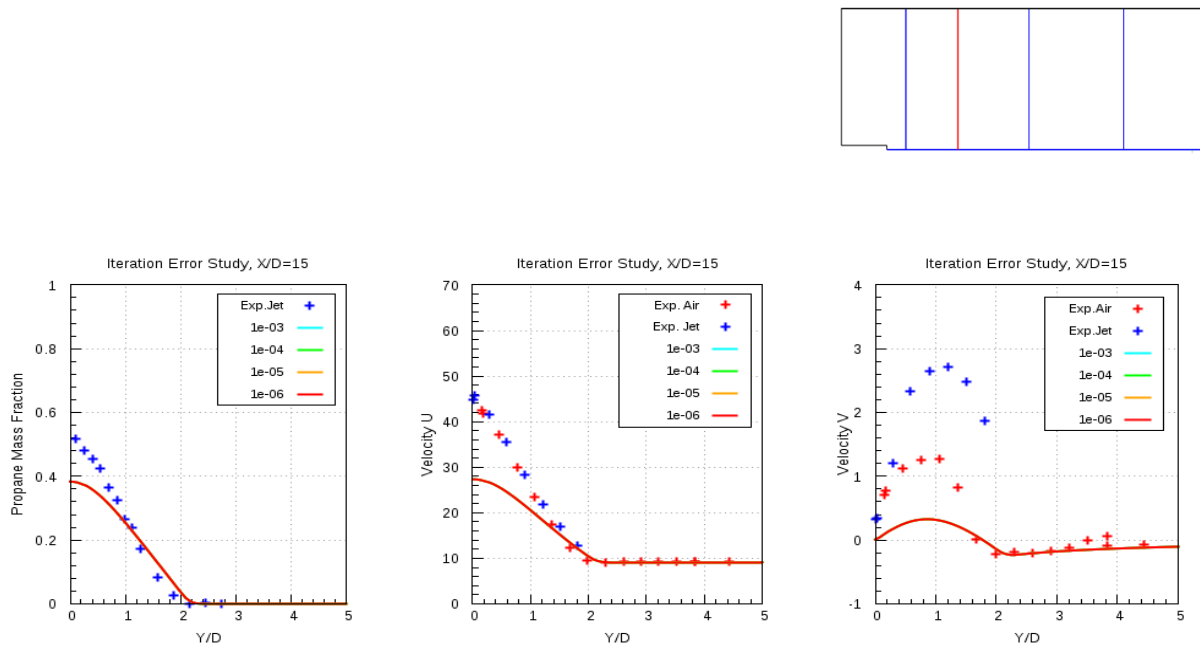


Figure 8.1(a)

Figure 8.1(a) shows the comparison of the, radial propane mass fraction, axial (U) and radial (V) velocity component profiles, obtained from numerical results with experimental data. It is seen from the plots that the results of every convergence target overlap over each other and thus not allowing us to decide an appropriate convergence target. Thus, differences in the propane mass fraction values amongst different convergence targets have been carried out in ANSYS CFD Post 16.1.

Propane mass fraction difference between convergence targets 10^{-5} and 10^{-6} showed the smallest difference and thus convergence criteria 10^{-5} was decided to be appropriate enough. In the profile plots for the mean axial velocity component there exists a noticeable difference between the numerical results and experimental data. This can be explained due to insufficient mesh resolution in mesh 2.

8.1.2 Spatial discretization error

For this study the convergence criterion of 10^{-5} along with the conservation target of 10^{-3} were used. The simulations were carried out with k- ω SST model on all mesh resolutions with auto timescale. The following figures show the comparison of the numerically obtained results with the experimental data.

Figure 8.2(a) shows the variable values plotted against the accumulated time step. These plots show the residual convergence history of the simulations carried out on mesh 3 and mesh 4. It is seen that for mass and all momentum components the specified convergence target of 10^{-5} , is achieved. Figure 8.2(b) shows the imbalances in the conserved quantities plotted against the accumulated time step. Conservation criteria specifies that there are no imbalances existing in the conserved quantities. This assures that our flow physics has been resolved completely. It is seen from the figure that the propane mass fraction imbalance at beginning of the simulation is 100% at the outlet, as there is no propane there. After some 50 iterations it is seen that the propane mass fraction reduces and hence after 50 iterations the propane reaches the outlet. The mass fraction of propane gradually reduces towards the specified conservation target and so does the other quantities. Thus the simulations are accepted as converged only when both the criteria specified are achieved by all the fuel components and flow field quantities. All meshes achieve the convergence criteria.

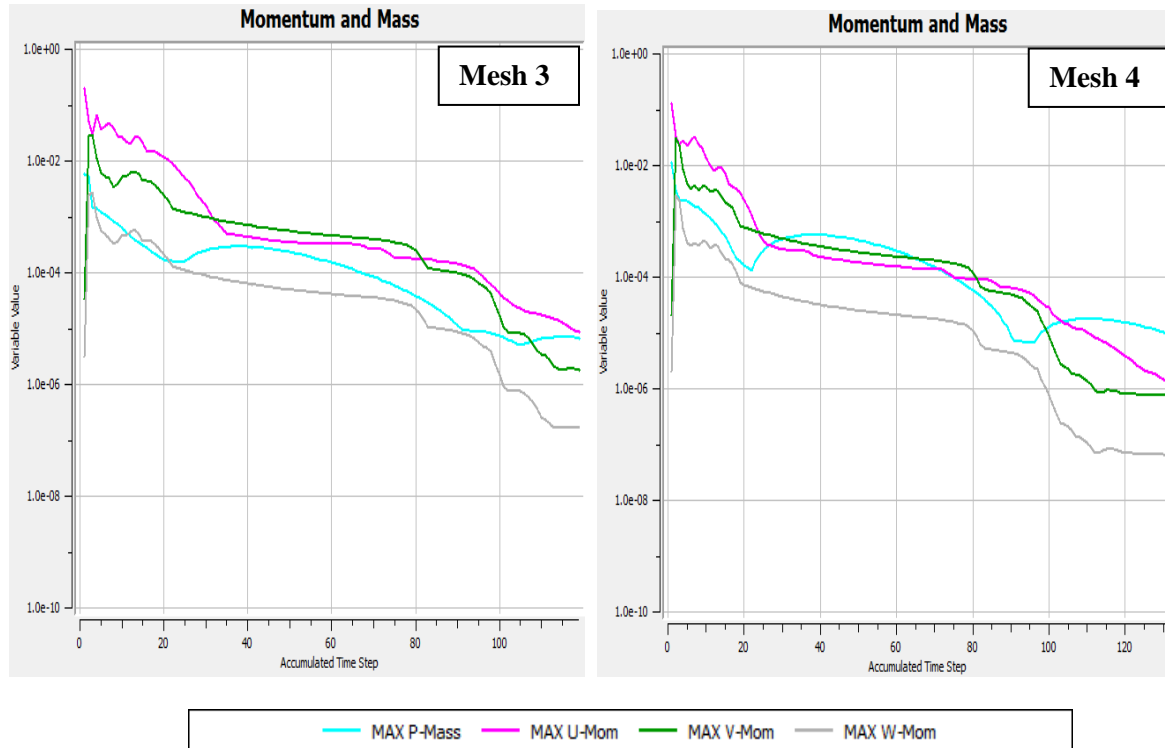


Fig. 8.2 (a)

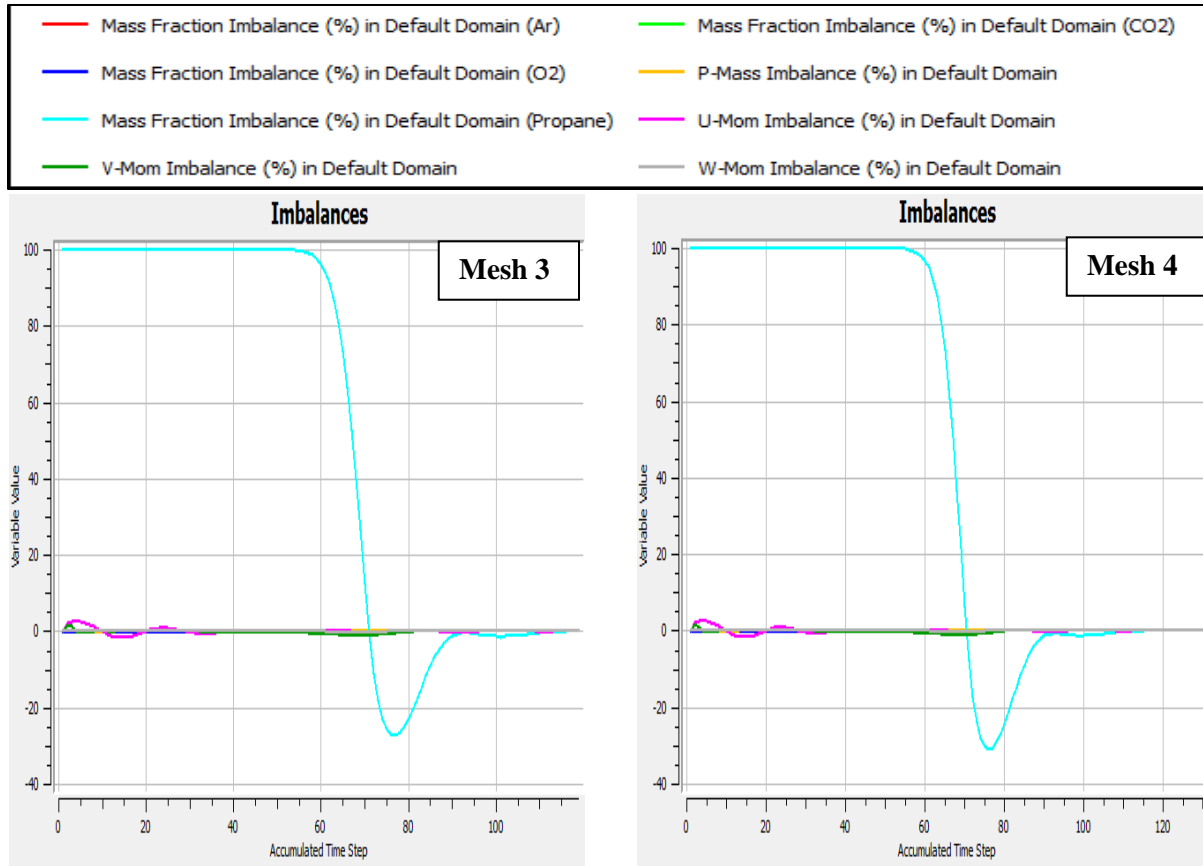


Fig. 8.2 (b)

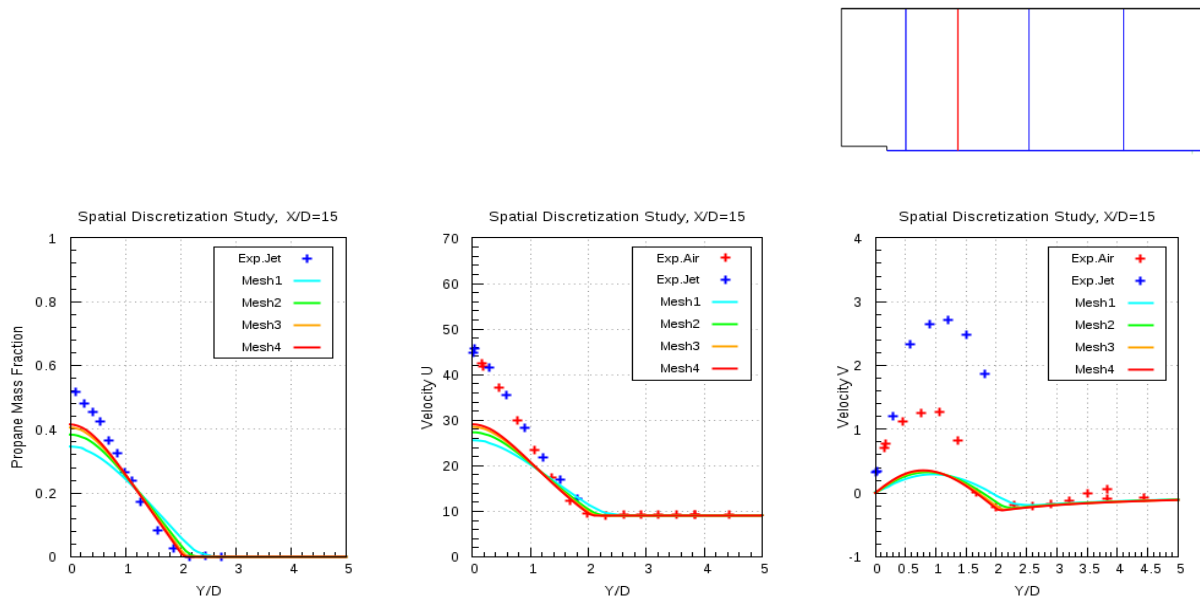


Fig. 8.2 (c)

Figure 8.2(c) shows the propane mass fraction and velocity profiles, of all meshes, compared with the experimental data. From the comparison plots shown above it is clearly seen that with the refinement of meshes the results progressively tends towards the mesh independent results. Specifically from the results of mesh 3 and 4 it is clear that on resolution of mesh 4, mesh independent solution is achieved. Important thing to notice here from the velocity profiles is that the jet loses momentum faster as compared to the experimental jet at location $X/D = 15$ downstream the bluff-body. This might have occurred due to the improper assumption of turbulence inlet boundary condition at jet inlet. As initial turbulent boundary conditions are considered to one of the factors which affect the downstream characteristics of the jet in a co-flow of air. Thus a study with different turbulent inlet boundary conditions at jet inlet has been carried out.

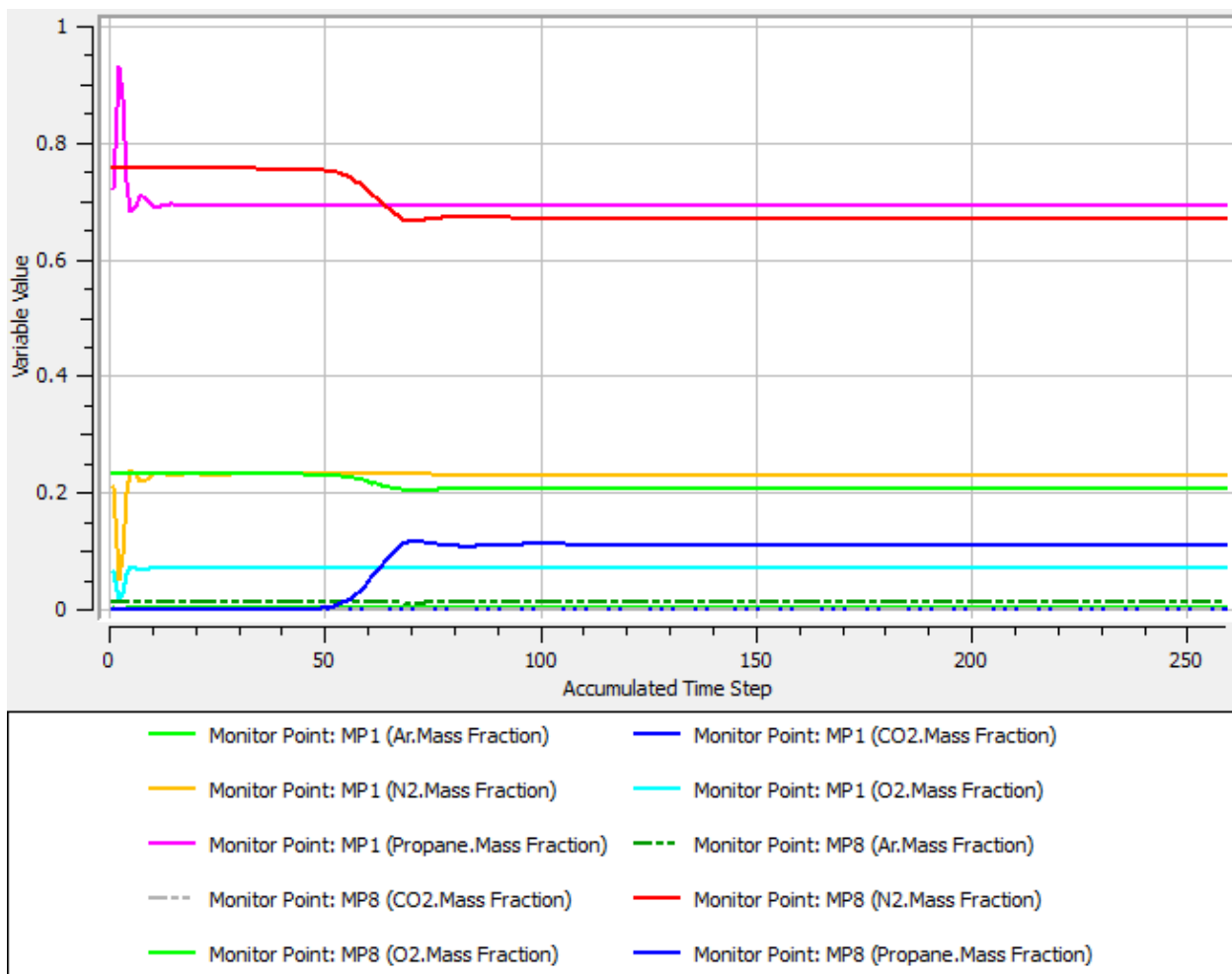


Figure 8.2 (d)

Figure 8.2(d) shows from the lines of the monitoring points that after 120 iterations they are straight, which indicates that no physical changes are occurring in the domain. This assures that no physical phenomenon, occurring at the small time scales, goes unresolved.

8.1.3 Turbulence inlet boundary condition (TIBC)

Test name	Turbulence model	TIBC, jet inlet	TIBC, co-flow inlet
CSV_SST	SST	K and ω	Fractional Intensity & Eddy Viscosity ratio
CSV_KEpsilon [#]	K- ϵ	K and ϵ	Fractional Intensity & Eddy Viscosity ratio
KLS_SST	SST	K and LS	K and LS
KLS_KEpsilon [#]	K- ϵ	K and LS	K and LS
PA CSV SST	SST	K and ω	Fractional Intensity* & Eddy Viscosity ratio

Table 6

CSV_SST – It indicates that turbulence inlet boundary conditions have been used from interpolated profile of fully developed flow at fuel jet inlet, **KLS_SST** – It stands for the case where turbulent kinetic energy (K) and Length scale (LS) have used, as TIBC, by calculating them from the experimental data, # - indicates that the constant $C_{\epsilon 1}$ in the dissipation equation (ϵ) of the standard k- ϵ model is modified from 1.44 to 1.6 [5], to address the round jet anomaly phenomenon, **PA CSV SST** – indicates that the inlet profiles have been used both at co-flow and fuel jet inlet along with the new value of turbulence intensity

Figure 8.3 (a) shows the axial profiles obtained from numerical results for velocity u invariant and propane mass fraction invariant compared with the experimental data. In case of velocity invariant profile it is seen that profiles with k- ω SST model over-predict the velocity decay compared to the experimental profiles, after the axial location $X/D = 6$. From the propane mass fraction invariant profiles it is seen that the profiles with k- ω SST are in good agreement with the experimental data. Also the change in the inlet boundary conditions with k- ω SST model shows no big influence on to the profiles for both invariants. In the case with inflow velocity profile at co-flow provides the solution with no changes in the results. Modified k- ϵ model from velocity u invariant plot predicts that the velocity decay which is in exact agreement with the experimental data, but at the same time under predicts the propane mass fraction decay as seen from the propane mass fraction invariant plot.

Figure 8.3(b) shows the radial profiles obtained from the numerical results, of propane mass fraction, axial and radial velocity components, compared with the experimental data. As observed for the axial profiles of k- ω SST model shows no sensitivity towards the turbulent boundary conditions. Modified k- ϵ model predicts the exact centerline velocities and at the same time under-predicts the mixing of jet as seen from the propane mass fraction profiles. Other radial velocity profiles can be found in appendix.

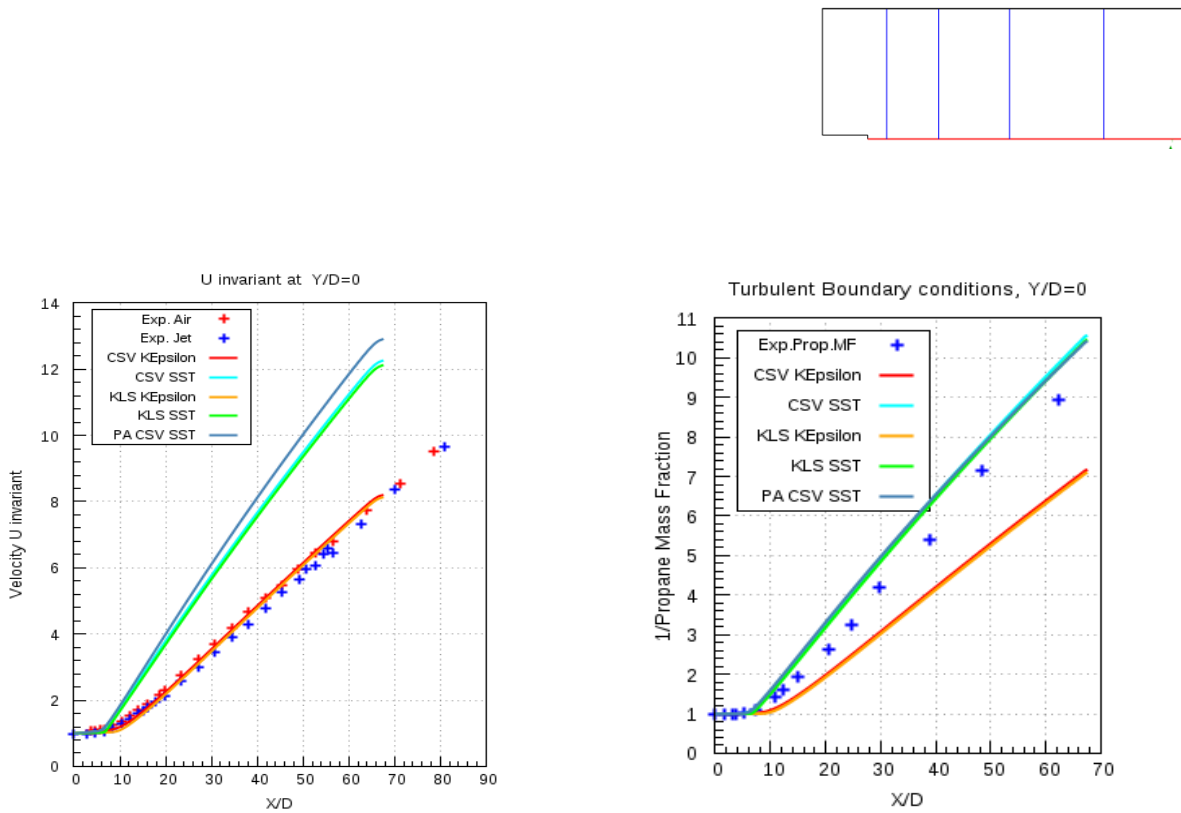


Fig.8.3 (a)

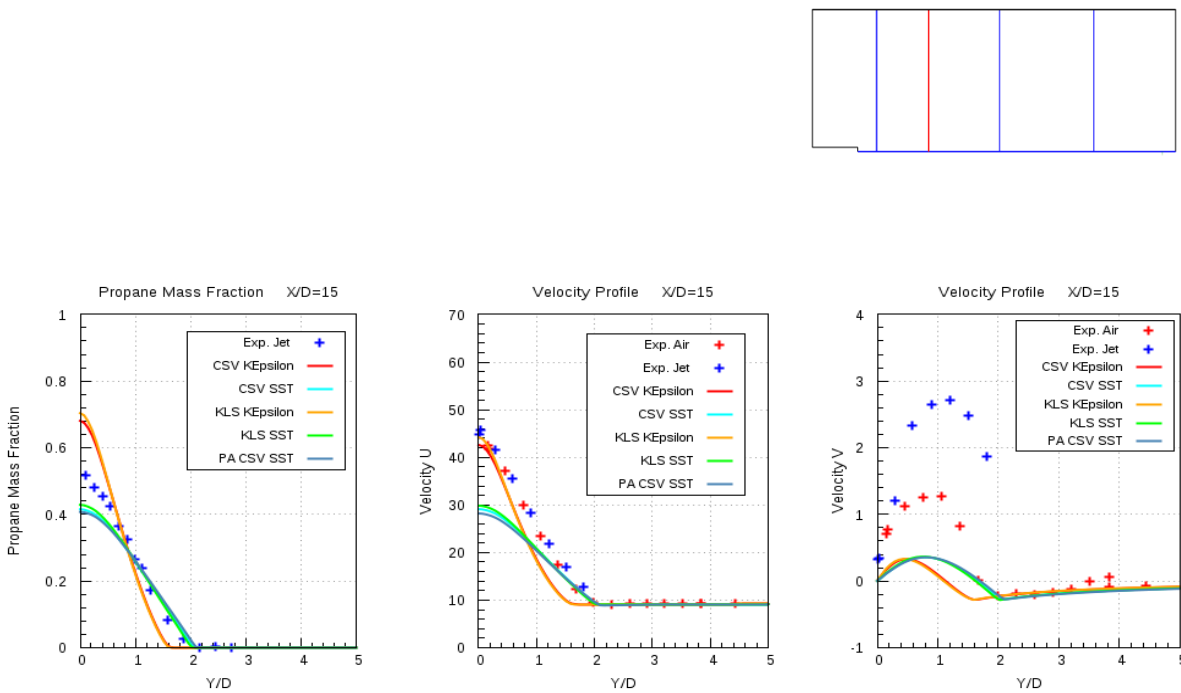


Figure 8.3 (b)

8.1.4 Turbulent Schmidt number (Sc_t)

The results presented here were calculated with k- ω SST model, mesh 4, auto timescale and convergence criteria as decided before. In this test simulations were carried out with four different Sc_t numbers ranging from 0.6 to 0.9. Comparison of axial and the radial propane mass fraction profiles have been made with the corresponding experimental data.

Figure 8.4(a) shows the axial propane mass fraction and propane mass fraction invariant profiles for different Sc_t , compared with the experimental data. Looking at both the profiles it is clear that the Sc_t of 0.9 is in good agreement with the experimental data and delivers the most accurate result.

Figure 8.4(b) shows the radial propane mass fraction profiles, at $X/D = 4, 15 & 30$, compared with the experimental data. It is seen that the Sc_t 0.9 is in very good agreement with the experimental data.

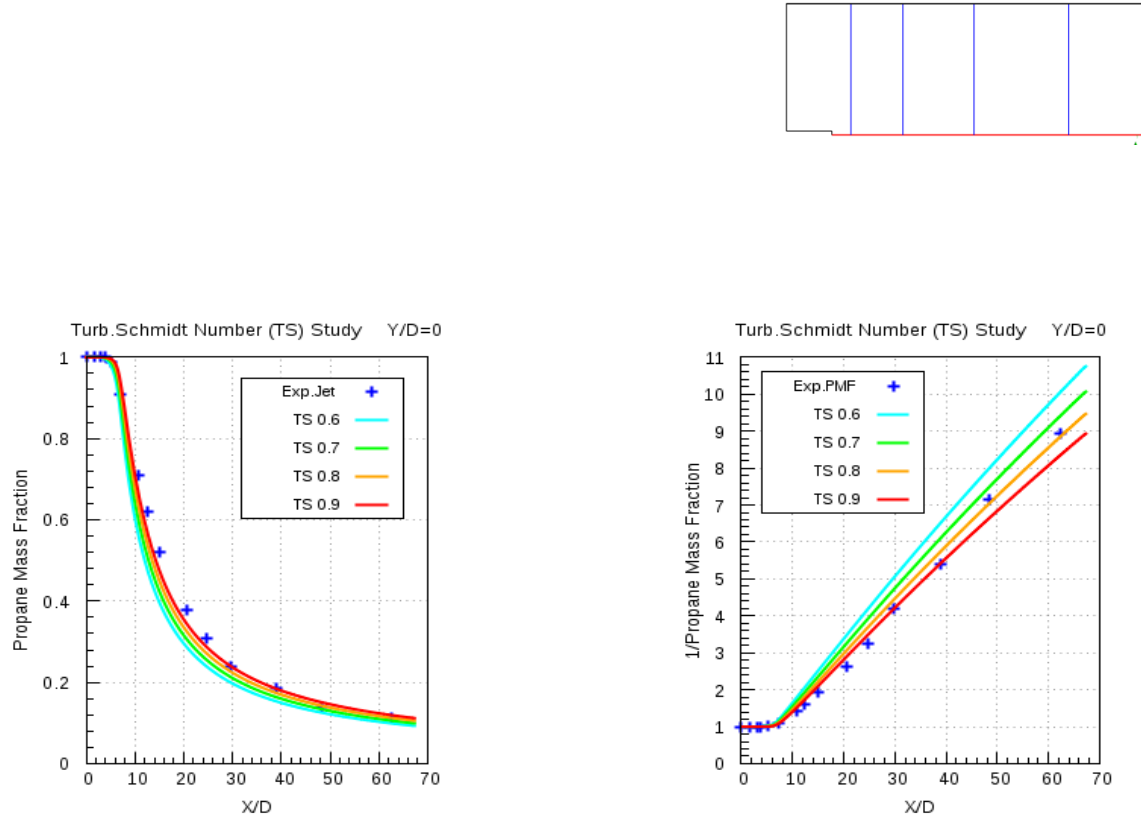


Figure 8.4 (a)

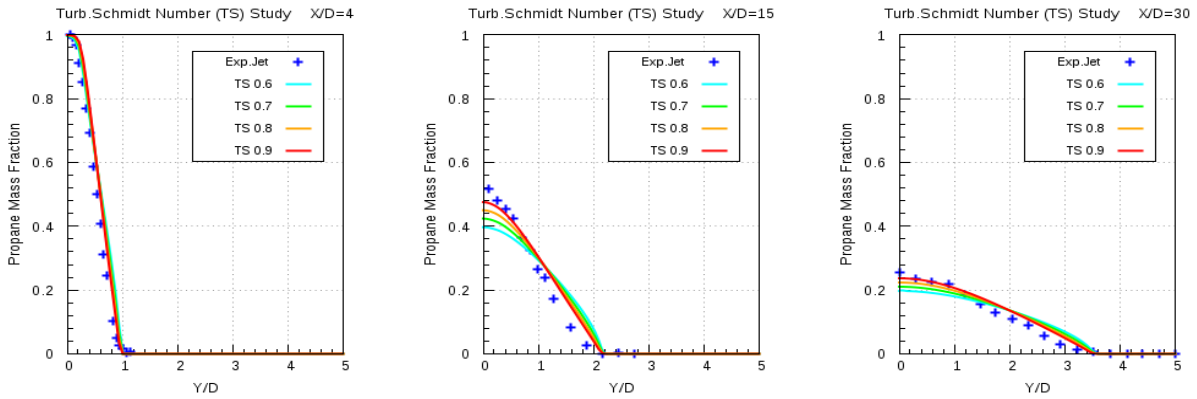


Figure 8.4(b)

8.1.5 Model Error Study

In this study all turbulence models as mentioned before have been used in combination with different mesh resolutions. The propane mass fraction and the velocity profiles obtained from the numerical results are compared with the experimental data. The comparison is shown here for the calculations carried out with mesh 4 resolution and different turbulence models. Every calculation performed satisfied all the convergence criteria. For BSL RSM model results from mesh 3 were used, as solver failed on performing calculations on mesh 4. Some additional efforts had been applied, i.e. increasing maximum number of iterations, reducing the convergence target value and reducing the time step to a smaller value, to achieve converged solutions when models BSL RSM and EARSM were used for calculations.

Figure 8.5(a) shows the axial propane mass fraction, propane mass fraction and velocity invariant profiles compared with the experimental data. It is seen from the propane mass fraction profiles that the modified k- ϵ model (KEpsilonmod) under-predicts the propane mass fraction decay and at the same time profiles from other models are in good agreement with the experimental data. From the profiles it is clear that k- ω SST over-predicts the velocity decay and the modified k- ϵ model is in good agreement with the experimental data. From the propane mass fraction invariant profiles it is seen that the modified k- ϵ model under-predicts the propane mass fraction decay, while other models are in good agreement with the experimental data.

Figure 8.5(b) shows the radial propane mass fraction and velocity profiles compared with the experimental data at location X/D = 15. It is seen from the comparison plots that the modified k- ϵ model is in good agreement with the experimental data, in case of velocity profiles, and it under-predicts propane mass fraction decay. k- ω SST and k- ϵ model are providing consistent results with each other and are in good agreement with the experimental data.

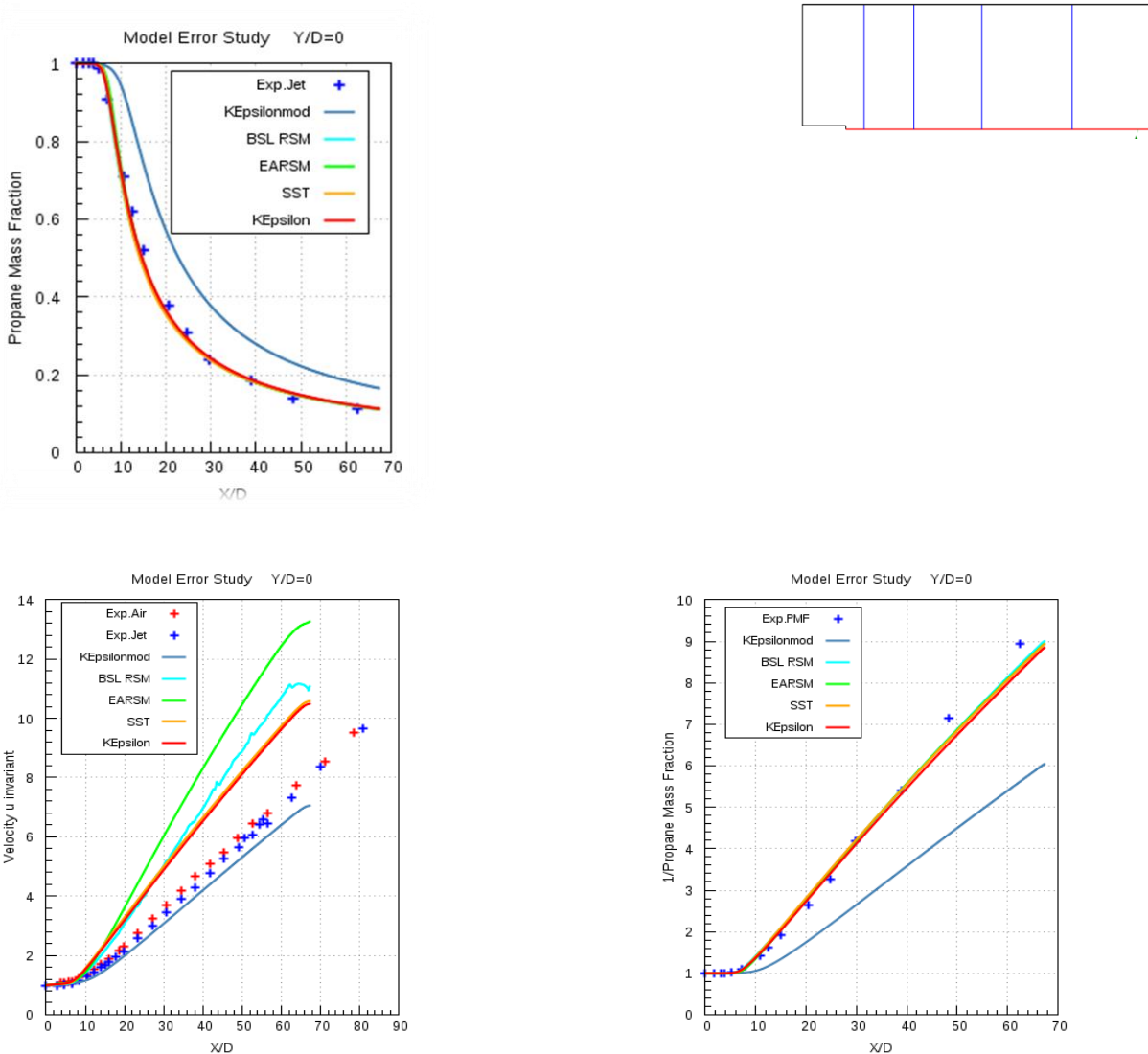


Figure 8.5(a)

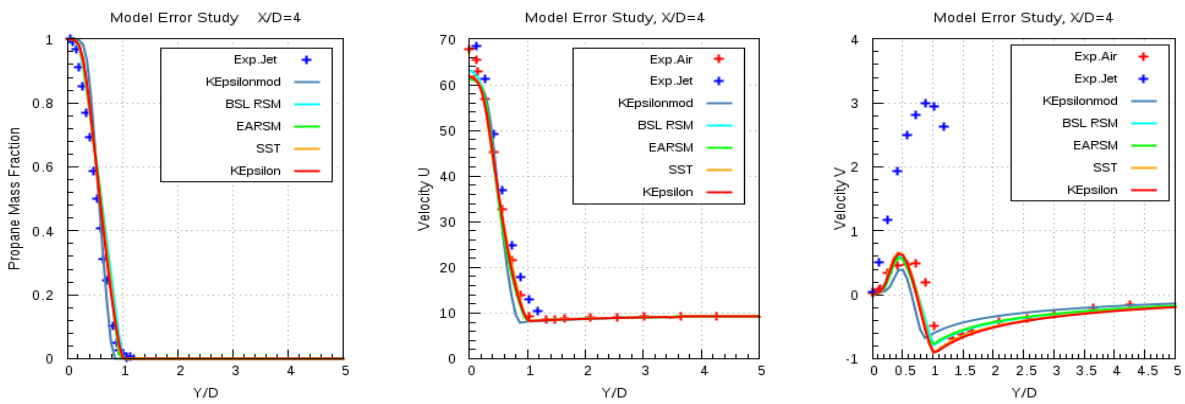


Figure 8.5(b)

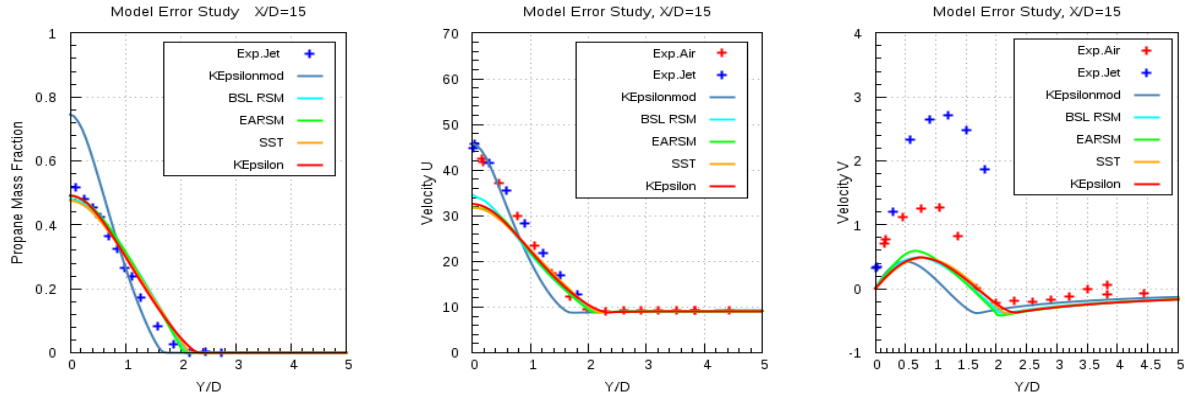
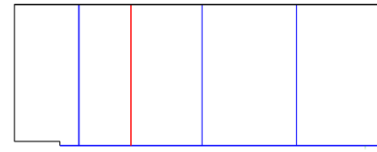


Figure 8.5(c)

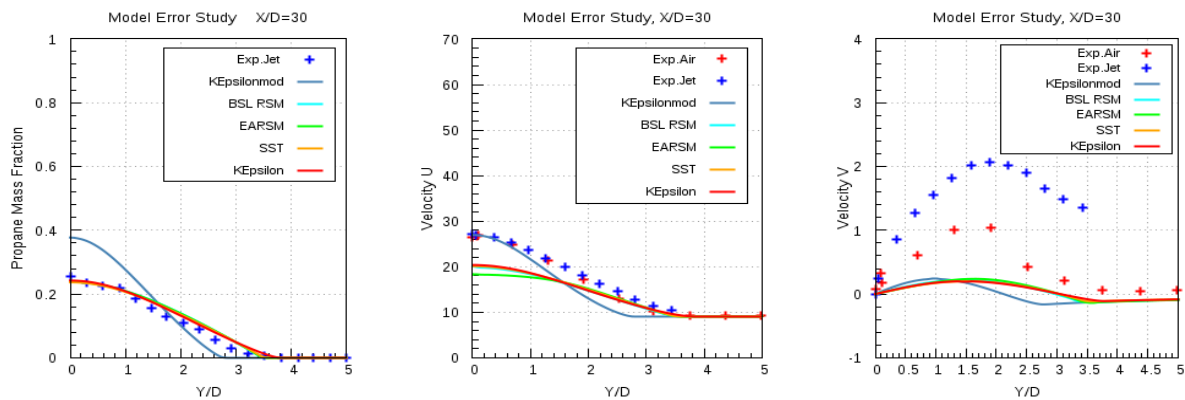


Figure 8.5(d)

8.2 ANSYS Fluent 17.0

Similar studies as in ANSYS CFX 16.1 have been performed with ANSYS Fluent 17.0. The iteration or convergence target has been chosen as 10^{-7} for ANSYS Fluent 17.0 and mesh 4 is the chosen mesh resolution for all the simulations that have been carried out. Sc_t was also modified to 0.9, which is 0.7 by default in ANSYS Fluent 17.0. Also in order to have a fair comparison with ANSYS CFX 16.1, the kinematic diffusivity has been also modified to the same value as in ANSYS CFX 16.1. Simulations were performed with standard k- ϵ , realizable k- ϵ , k- ω SST and standard k- ω turbulence models.

8.2.1 Model Error Study

In this study the turbulence models were combined with the different methods of defining kinematic diffusivity and also with different mesh resolutions. As per discussed results of only mesh 4 will be compared with the experimental data.

Results only for the $X/D = 15$ will be shown here

Figure 8.6(a) shows the comparison of the radial profiles of propane mass fraction and velocity obtained from numerical results with experimental data. Refer Table 7, for the naming convention of legends. Combination of different turbulence models with the two diffusivities are also compared with each other, apart from comparison with the experimental data. From the profile plots it was observed that same turbulence model with different diffusivities delivered the same results and hence their profiles are overlapping each other. Standard k- ω model delivers some different results as it was having some different implementation in ANSYS Fluent software. Apart from that k- ω SST and standard k- ϵ delivers almost consistent results with each other and they are in good agreement with the experimental data. Other comparison plots are shown in Appendix.

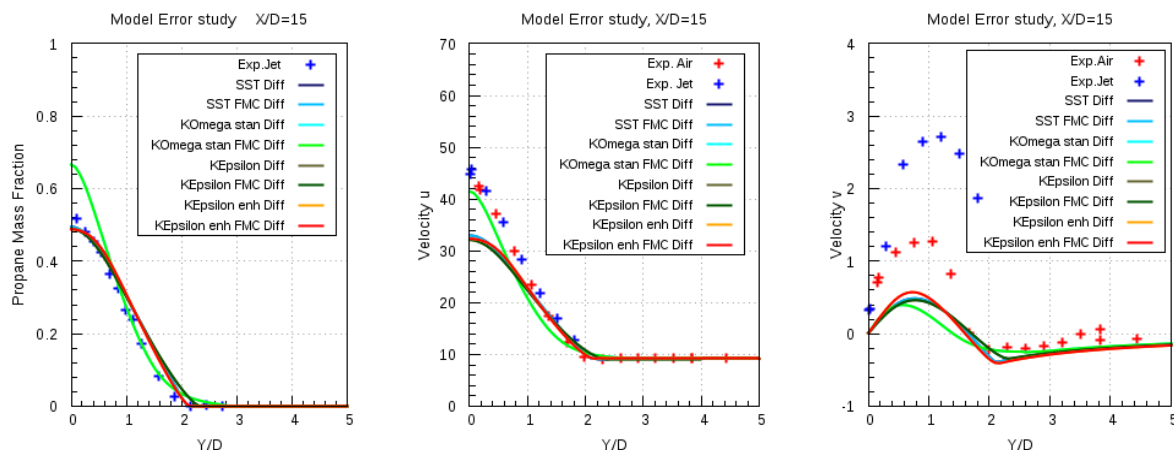


Figure 8.6(a)

8.3 Solver Comparison between ANSYS CFX 16.1 & ANSYS Fluent 17.0

In this study a cross comparison of the results obtained from the different turbulence models of the two solvers has been carried out with the experimental data. Turbulence models used here are mentioned below:

ANSYS CFX 16.1	ANSYS Fluent 17.0
K- ω SST	K- ω SST with constant diffusivity (K- ω SST Diff) K- ω SST with full multi-component diffusivity (K- ω SST FMC Diff)
K- ε	K- ε constant diffusivity (K- ε SST Diff) K- ε SST with full multi-component diffusivity (K- ε SST FMC Diff)

Table 7

K- ω SST:

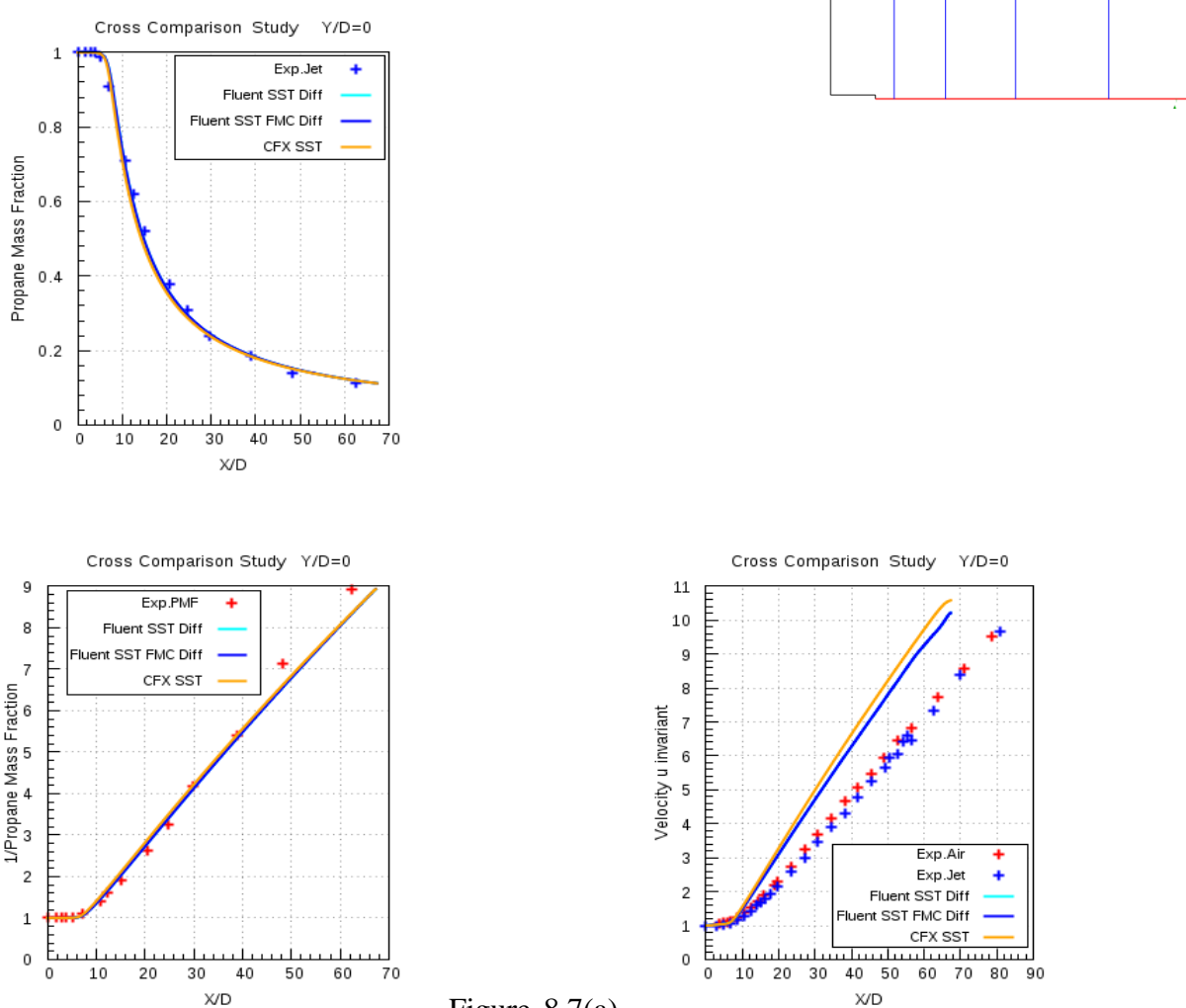


Figure 8.7(a)

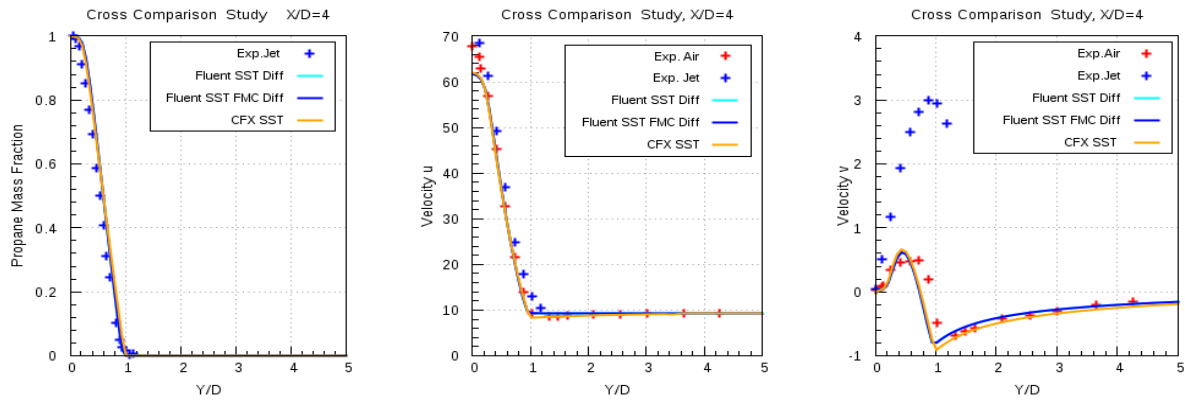
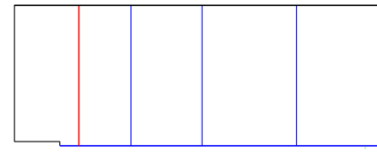


Figure 8.7(b)

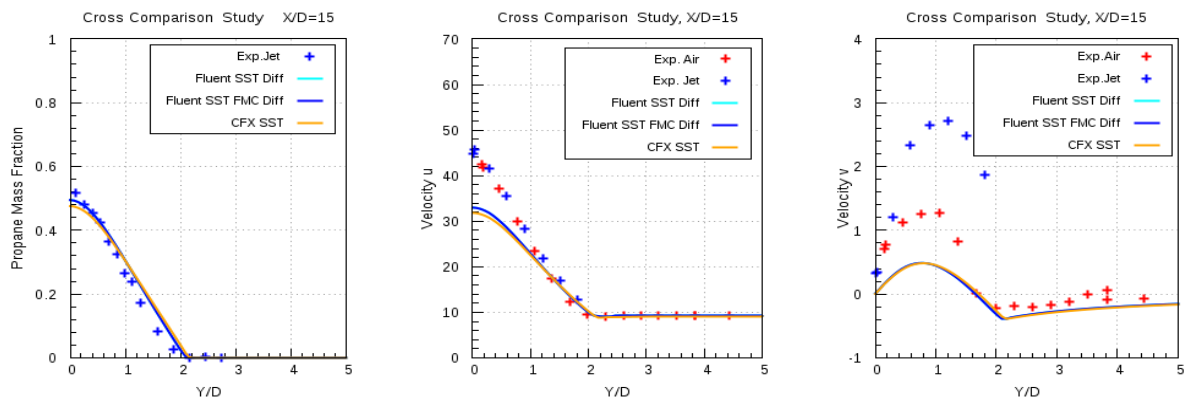


Figure 8.7 (c)

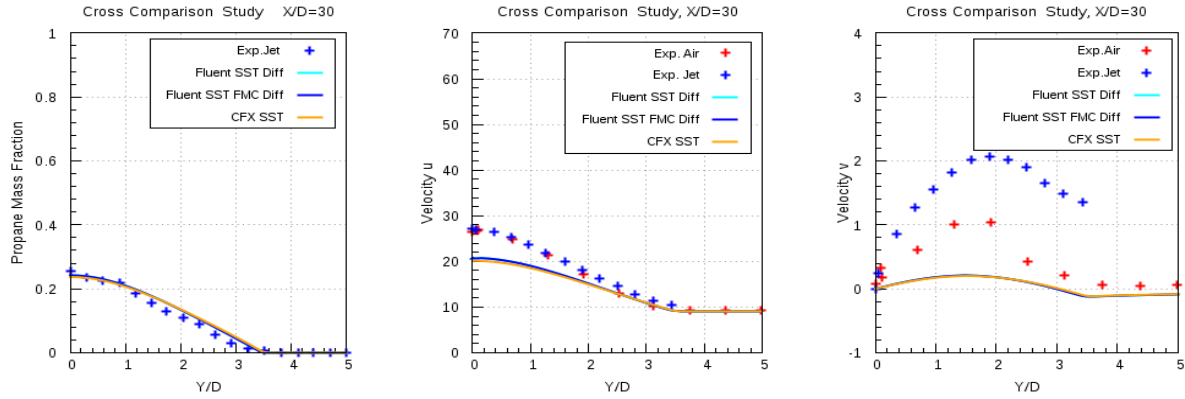
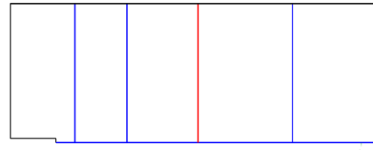
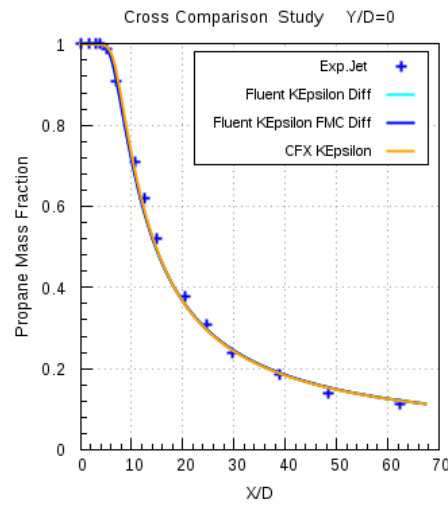


Figure 8.7 (d)

Figures 8.7(a) & 8.7(b)-(d), shows the axial and the radial profiles obtained numerically are compared with the experimental data for the $k-\omega$ SST model of both the solvers. It is seen that $k-\omega$ SST model for both the solvers are in good agreement with each other and also with the experimental data.

K- ϵ model:



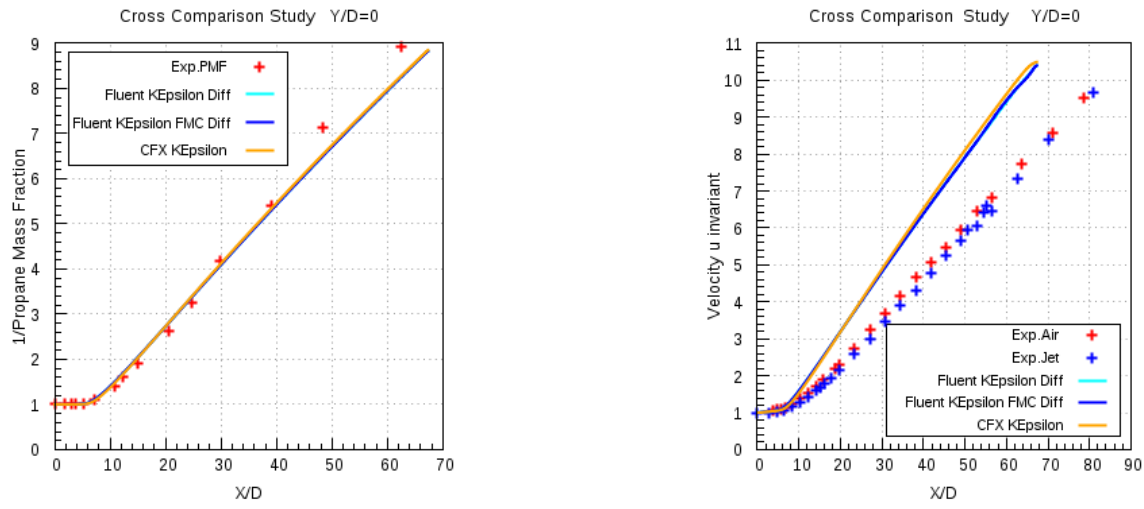


Figure 8.8 (a)

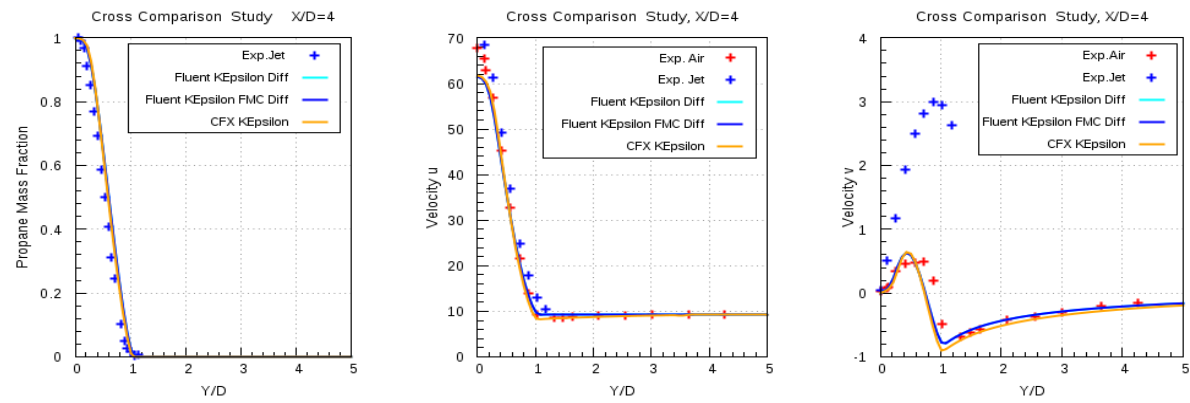


Figure 8.8 (b)

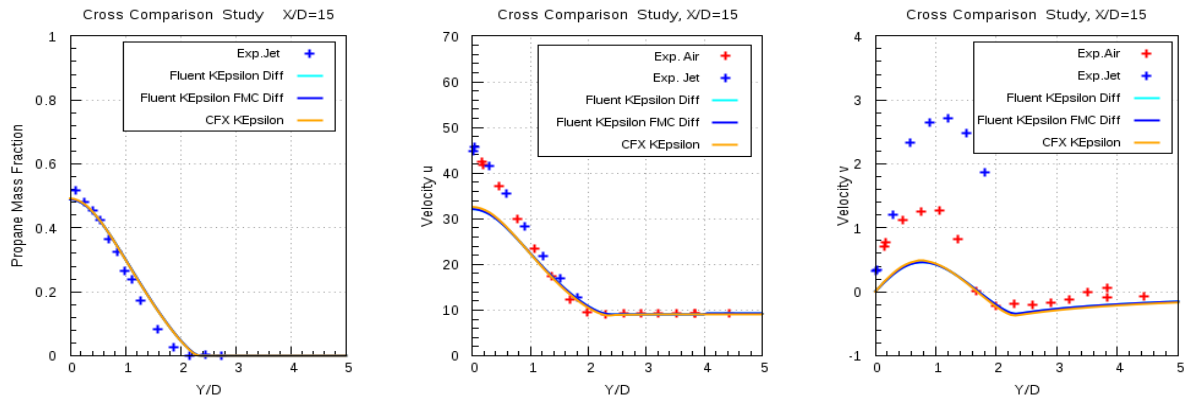


Figure 8.8 (c)

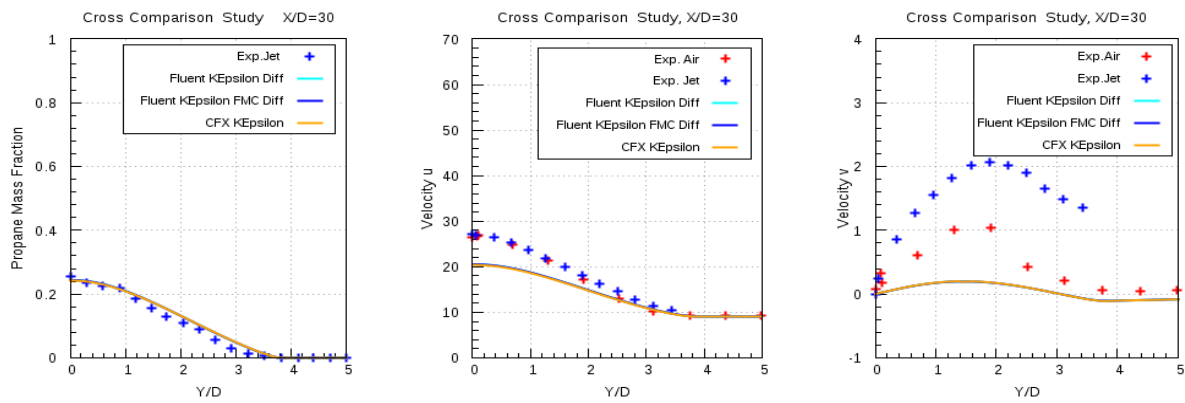
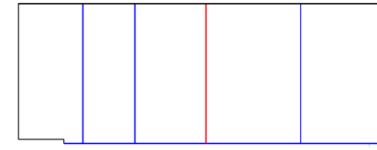


Figure 8.8(d)

Figures 8.8(a) & 8.8(b)-(d), shows the axial and the radial profiles obtained numerically are compared with the experimental data for the k- ϵ model of both the solvers. It is seen that k- ϵ model for both the solvers are in good agreement with each other and also with the experimental data.

9 Experimental Description

Measurements are performed in the well defined recirculation zone which is established downstream of an axisymmetric bluff body. A schematic of the burner and the flow field is shown in figure 9.1(b) [7]. The bluff body has an outer diameter of $D_B = 50$ mm and a jet diameter of $D_J = 3.6$ mm. The co-flow air velocity is fixed at 20 m/s for all experiments. The turbulence intensity of the co-flowing air is low, at ~2%, and it is assumed to have a minimal effect on the highly turbulent recirculation zone. The laser Doppler velocimetry (LDV) technique is used to measure, simultaneously, the axial and radial velocity components. The mixture fraction measurements were made using imaging of Rayleigh scattering technique. For the measurement of flow field data, which comprises of the mean and rms fluctuations of axial and radial velocities, the experiment was performed with using pure air at both fuel jet & co-flow inlets. Flow field data is provided in the form of three data-sets.

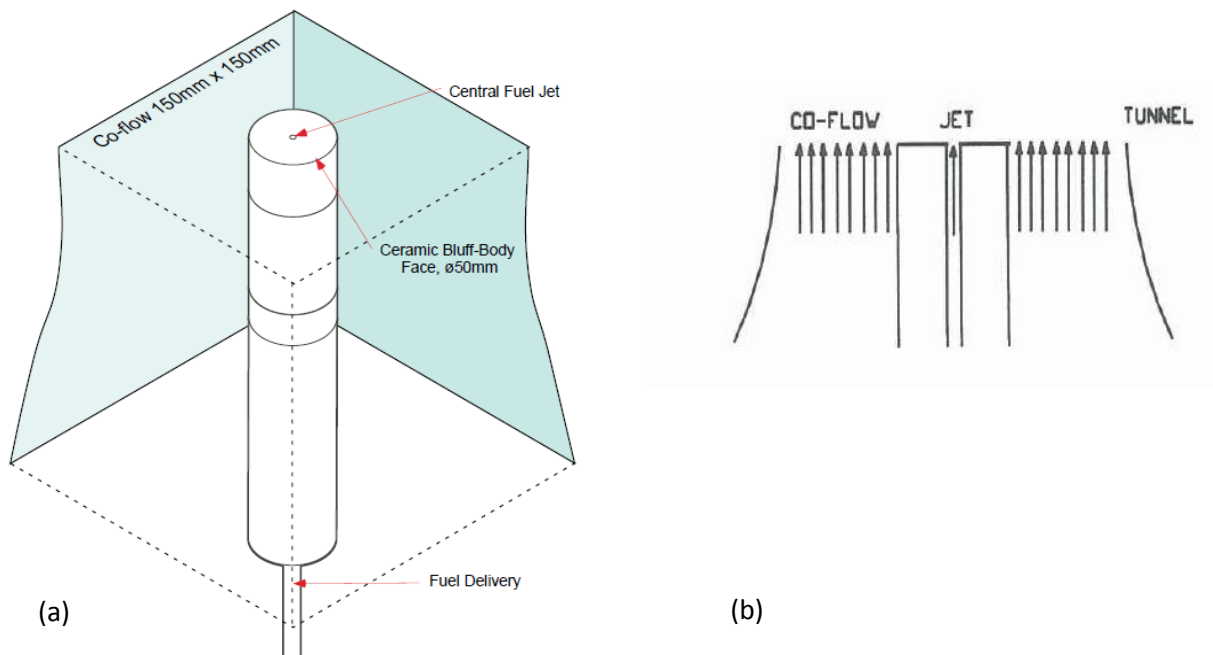


Figure 9.1

Mixing field data, which comprises of mean and rms fluctuations of mixture fraction, have been measured by carrying out experiments using different fuels with different velocities at the fuel jet inlet[6]. The fuel jet velocity is varied in order to investigate the dependence of the flow pattern on the momentum of the jet. The table below lists the fuels used with different velocities:

Fuel	CNG	Ethylene	LPG
Velocity (m/s)	50	85	70

Table 8

Both flow & mixing field data were measured at the axial (X-axis) and radial (radius r) locations behind the bluff body. The bluff body diameter, $D_B = 50$ mm, was used to normalize the axial location (X/D_B) and the bluff body radius, $R_B = 25$ mm, was used to normalize the radial location (r/R_B). The following quantities have been measured:

1. Mean axial and radial velocity components (U,V)
2. Mean mixture fraction component
3. RMS Fluctuating axial and radial components (u' , v')
4. RMS Fluctuating mixture fraction component

The locations at which the flow field data have been measured are shown below:

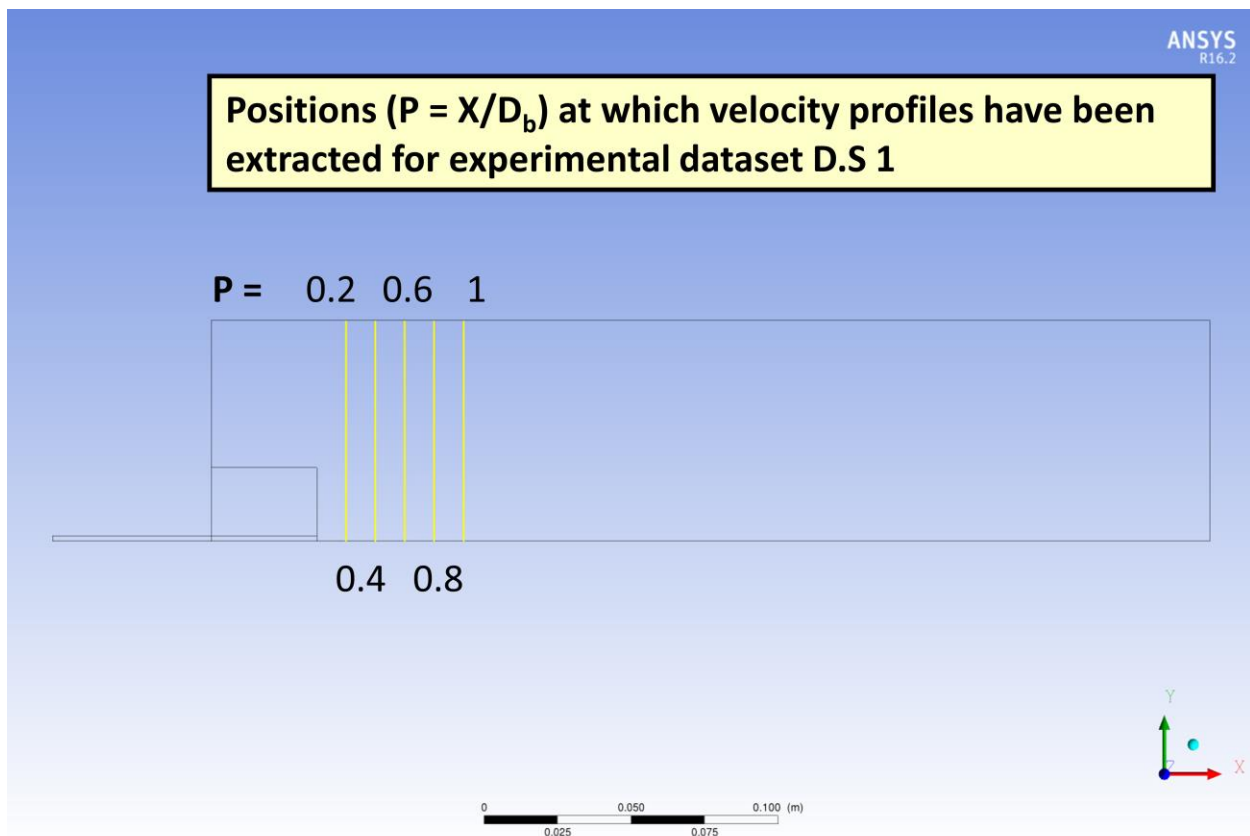


Figure 9.1(c)

Figure 9.1(e) shows the locations in between which the mixture fraction data was measured. The mixture fraction measurements have been performed, at every 1 mm interval, in between the yellow and red lines

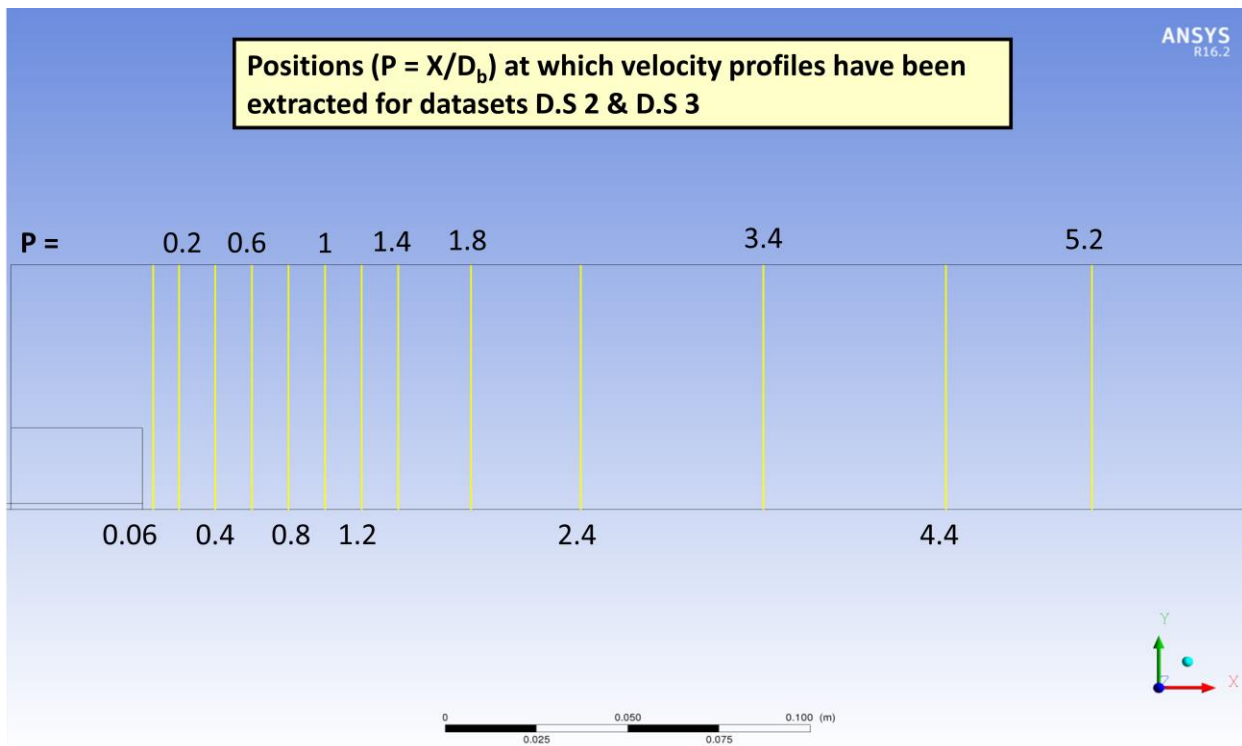


Figure 9.1(d)

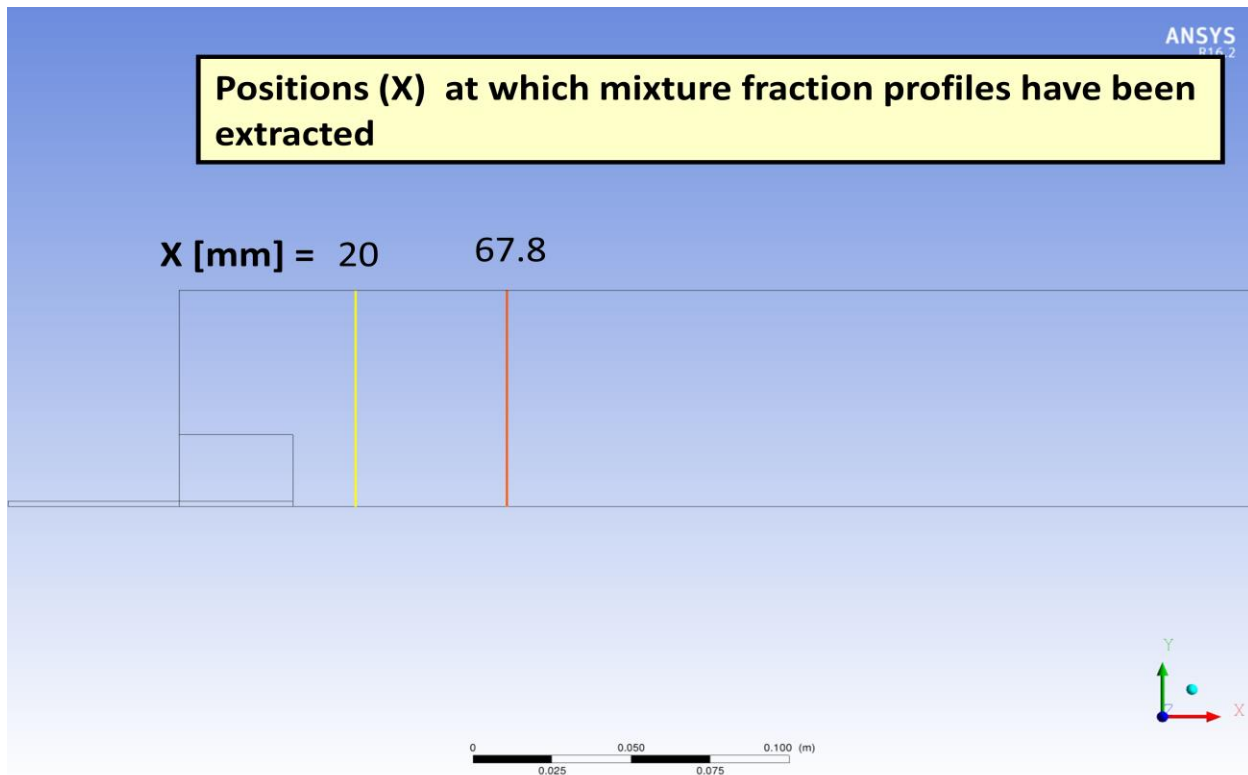


Figure 9.1(e)

10 Computational Domain

A full 3D computational domain was meshed with a non-uniform, hexahedral grid using ANSYS ICEM-CFD 16.1.

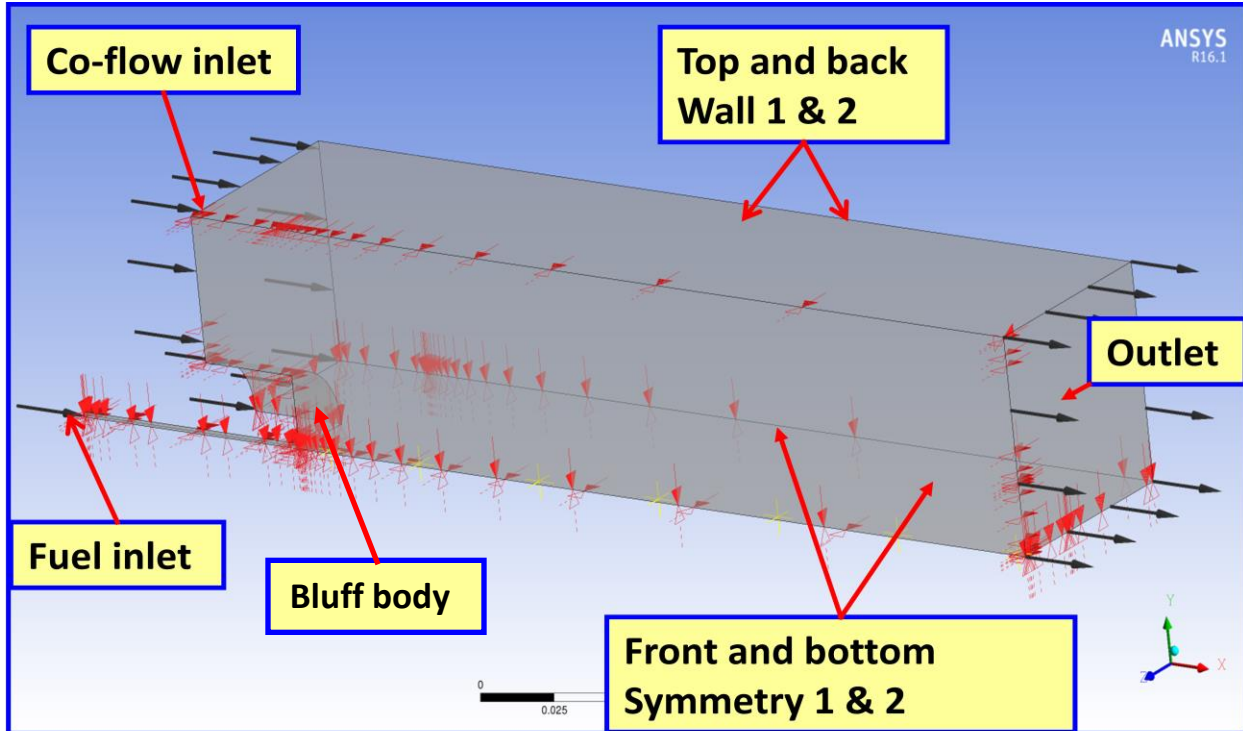


Figure 10.1(a)

A 90° symmetry sector has been taken from the complete domain, shown in figure 9.1(a), as the computational domain. In this case the blocking was done with a top-down approach [11] using O-Grid[11]. Internal O-Grid was generated for the whole domain and was merged & splitted, as per required, for certain locations in the domain which assured very good quality meshes there itself specifically at locations i.e. Fuel inlet, bluff body surface. A hierarchy of 3 meshes were constructed for this validation viz. Mesh 1, Mesh 2 and Mesh 3. The cell size for Mesh 2 was reduced to one half in each direction, compared to Mesh 1, and for Mesh 3 the cell size was reduced to one third in each direction, compared to Mesh 2. The grid refinement was concentrated close to the body so that the near wall effects can be resolved appropriately and also to capture the important physical phenomenon occurring behind the bluff-body. The grid was coarsened gradually towards the outlet.

From figure 10.1(b)[15], it is seen that the computational domain extends $6.08D_B$ downstream the face of bluff body and it ensured that the outlet boundary is sufficiently far enough in order that it doesn't interfere in the flow development. The fuel jet pipe extended 90 mm upstream from the face of bluff body to ensure that the velocity profile and turbulence quantities were fully developed at the exit plane, as in the experiment. The domain extended $1.5D_B$ in the radial direction so that the wall effects are negligible on to the flow development behind the bluff body. Also it extends $1.5 D_B$ in the negative z-direction.

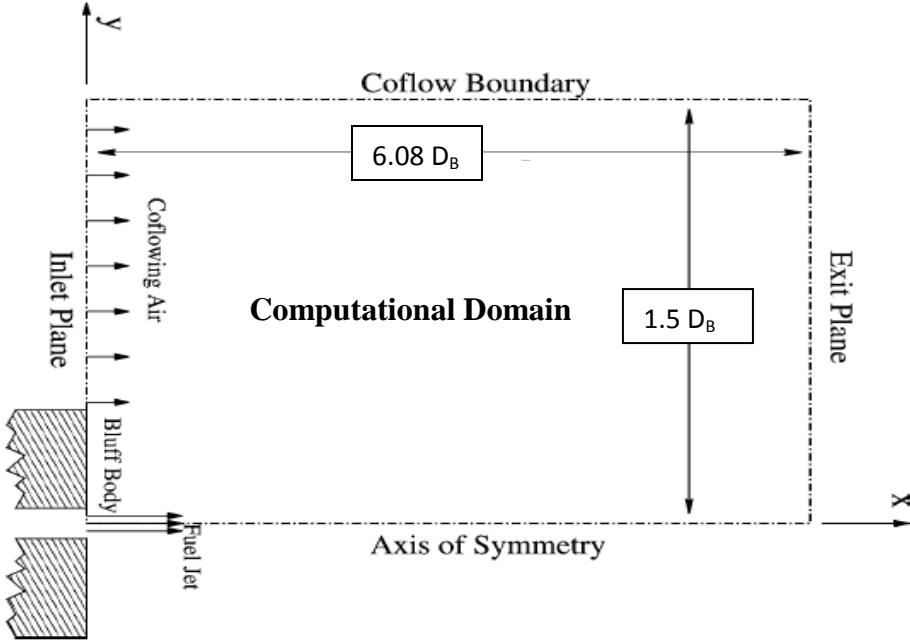


Figure 10.1(b)

Figure 10.1 (b) shows the 2d symmetric impression of the computational domain. Following table shows the details of the mesh heirarchy:

Parameter	Mesh 1	Mesh 2	Mesh 3
Elements	445779	3649862	12367909
Nodes	477248	3773055	12648672
Maximum Aspect Ratio	665	1864	3046
Minimum Grid Angle	45°	44.19°	40.95°
Max Y ⁺ on bluff body	6.23	3.08	2.01

Table 9

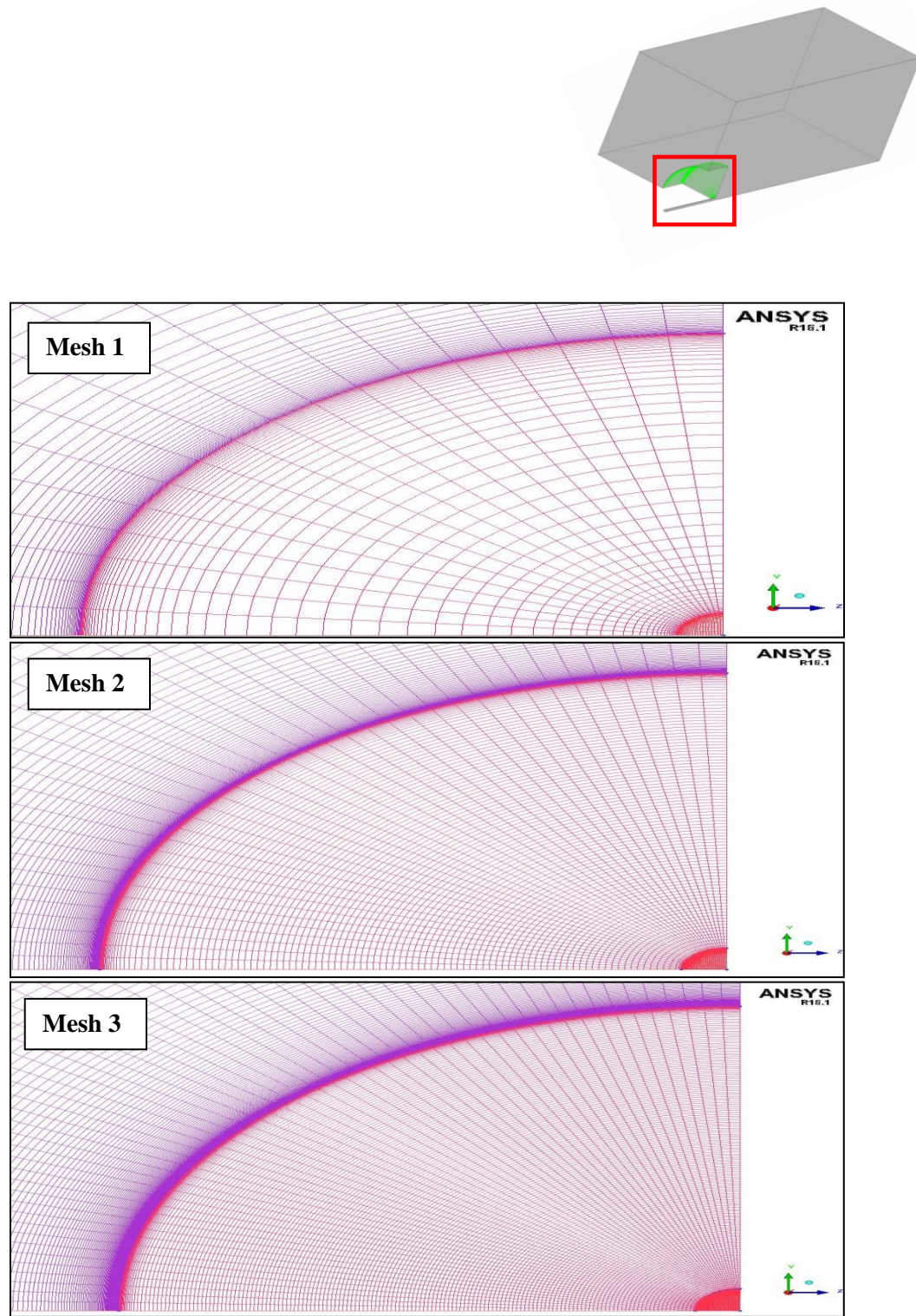


Figure 10.1(c)

Figure 10.1(c) shows the visual comparison of the three mesh resolution. The quality assurance studies and the inspection of the results performed here are similar to that mentioned in chapter 6, but additional quality assurance criteria were not performed here.

11 CFD Model Setup

11.1 Boundary conditions

In this test case the experiments were performed separately to measure flow and mixture field data. In order to compare the flow field data, obtained from simulations, with the experimental data air is used at both fuel jet and co-flow inlets with velocities 61 & 20 m/s respectively. For the simulations carried out to measure mixture field data different fuels with different velocities, as mentioned in the literature [6], have been used at the fuel jet and pure air at co-flow inlet.

11.1.1 Boundary conditions (Flow field)

Inlet velocities and turbulent inlet boundary conditions have been utilised as per specified in the literature [6]. Air at 25°C with constant properties was used as fuel at both jet & co-flow inlets.

Name	ANSYS CFX 16.1	ANSYS Fluent 17.0
Co-flow inlet	Normal Velocity = 20 m/s	Normal Velocity = 20 m/s
	Turbulent Intensity = 2%, Eddy Viscosity Ratio = 10	Turbulent Intensity = 2%, Eddy Viscosity Ratio = 10
Jet inlet	Normal Velocity = 61 m/s	Normal Velocity = 61 m/s
	Turbulent Intensity = 5%, Eddy Viscosity Ratio = 10	Turbulent Intensity = 5%, Eddy Viscosity Ratio = 10
Outlet	Relative Pressure = 0 Pa	Gauge Pressure = 0 Pa
Bluff body	No slip wall	No slip wall
Fuel pipe	No slip wall	No slip wall
Wall 1& 2	No slip wall	No slip wall
Symmetry 1&2	Symmetry	Symmetry

Table 10

11.1.2 Boundary conditions (Mixing field)

The boundary conditions for the mixing field except the jet inlet will remain the same as shown in the Table 9

Name	ANSYS CFX 16.1	ANSYS Fluent 17.0
Jet inlet	Normal Velocity = 50* m/s	Normal Velocity = 50* m/s
	Turbulent Intensity = 5%, Eddy Viscosity Ratio = 10	Turbulent Intensity = 5%, Eddy Viscosity Ratio = 10

Table 11

*Note : The velocity at the fuel jet inlet will vary depending on the experiment performed as mentioned in the literature [6].

11.2 Material Properties

11.2.1 ANSYS CFX 16.1

Flow field:

Air at 25°C with constant properties was used at both fuel jet & co-flow inlets.

Mixing field:

For the mixing field measurement, three different mixtures were prepared:

1. Mixture Air was defined as a Fixed composition mixture[12] of Ar(1.28%), O₂ (23.15%), N₂ (75.52%) and CO₂ (0.0035%).
2. Mixture Fuel was defined as a Fixed composition mixture of CNG, Ethylene and LPG. Composition of which can be found in the literature [6].
3. Air-Fuel Mixture was defined as a Variable composition mixture[12] of Mixture Air and Mixture Fuel, where mixture air was defined as constraint.

The composition of the fuels, used at the fuel jet inlet, are used as per mentioned in the literature[6].The purpose for using three different mixtures is to avoid the calculation of the additional transport equations for all the species. Hence only one additional equation will be solved for the entire mixture. Mass fraction of the fuel is defined as 1, at fuel inlet, and zero at co-flow inlet.

11.2.2 ANSYS Fluent 17.0

Material used for the Flow Field calculations was same as in ANSYS CFX 16.1

Mixing Field

Here only one mixture was made with all the component species of fuel and air respectively. Care was taken to have the same material properties i.e. density, dynamic viscosity etc for species in ANSYS CFX and Fluent.

11.3 Initialization

11.3.1 ANSYS CFX 16.1

In ANSYS CFX the initialization has been done by using the global initialization option. The domain is initially filled with air. The initial velocity field is provided with cartesian velocity components, as u = 20 m/s, v & w = 0. Initial turbulence conditions are chosen of type medium, turbulent intensity = 5% and Eddy viscosity ratio = 10. Mixture fraction of fuel is defined as zero here.

11.3.2 ANSYS Fluent 17.0

Initialization is done using the hybrid initialisation option available in ANSYS Fluent. In some cases the initialization was done using the interpolation of the results obtained from the coarser mesh on to the next finer mesh, to achieve converged solutions. See Interpolation option in [13].

11.4 Numerical Settings

11.4.1 ANSYS CFX 16.1

The convergence target was set to type MAX Residuals $< 10^{-4}$ and the conservation target was set to 5.10^{-4} . The discretization scheme used was high resolution [12] and the turbulent numerics scheme was also set to high resolution [12]. Auto timescale was the option used for the time step control. Maximum number of iterations was set to a value of 500*.

11.4.2 ANSYS Fluent 17.0

Flow analysis chosen here is of steady state type with pressure-based [13] solver. In all simulations Coupled method [13] is chosen for the pressure-velocity coupling. The gradient approximation is done by Least Squares Cell Based method [13]. For pressure second order method has been used. For momentum second order upwind scheme is used. Turbulent numerics have been approximated by using the First order upwind scheme. For all the species transport again a second order upwind scheme is used. Pseudo transient and higher order term relaxation [13] has also been selected. The residual type RMS (Root mean square) with a target value of 10^{-6} is selected for each solution variable. Time step method was chosen to be automatic with 800** as the maximum number of iterations for all the simulations

* , ** :In some cases to achieve converged results, for both the solvers ANSYS CFX 16.1 and ANSYS Fluent 17.0, the maximum number of iterations were increased and time step was reduced to a smaller value.

12 Results

12.1 ANSYS CFX 16.1

12.1.1 Iteration Error Study

This study was performed with mesh 1 and the series of convergence targets ranging from 10^{-3} to 10^{-6} . k- ω SST was the turbulence model used for the simulations. The simulations used pure air at fuel jet & co-flow inlet. Comparison of the velocity component profiles for different convergence targets along with the experimental data is shown in figure 12.1(a)-(d).The experimental flow field data has been provided in the form of three data sets, but the comparison of the velocity profiles with the experimental data will only be shown for the data set 2.

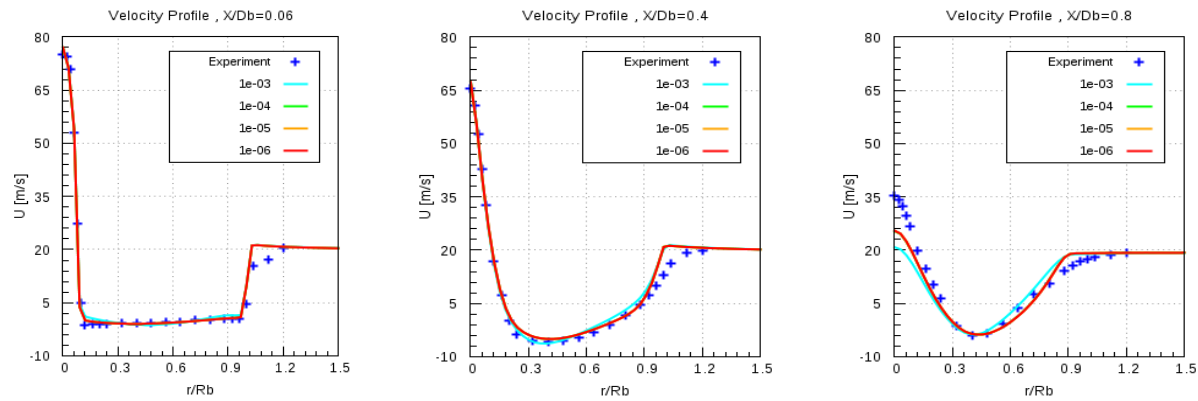


Figure 12.1(a)

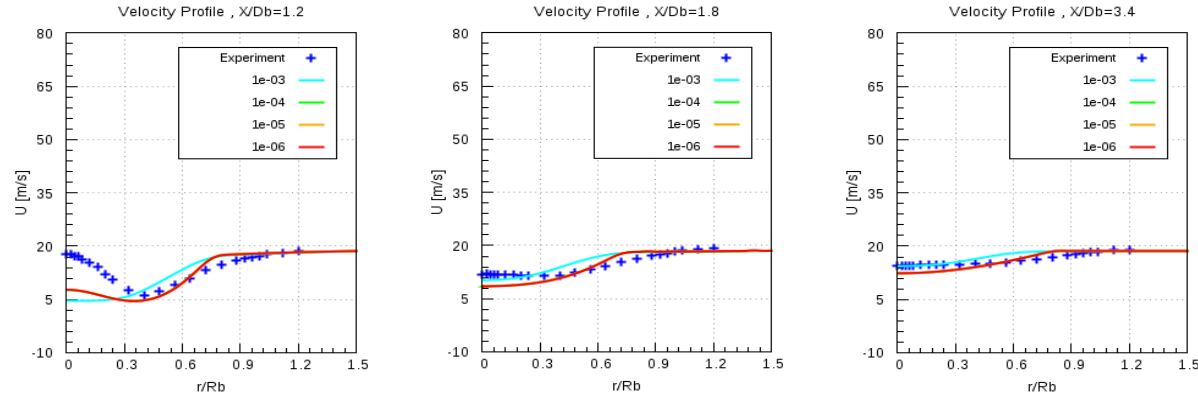


Figure 12.1(b)

Figure 12.1(a) & (b) shows the axial velocity component profile, plotted against the normalised radial locations, compared with the experimental data. It is seen from the figures above, that velocity profiles for all, except for convergence target of 10^{-3} , overlap over each other and makes it difficult to decide which is the sufficient convergence level. Hence the magnitude of velocity, for different convergence levels, was compared in ANSYS CFD Post. Depending on the smallest velocity difference, between the convergence targets, it was decided to have 10^{-4} as the appropriate convergence level.

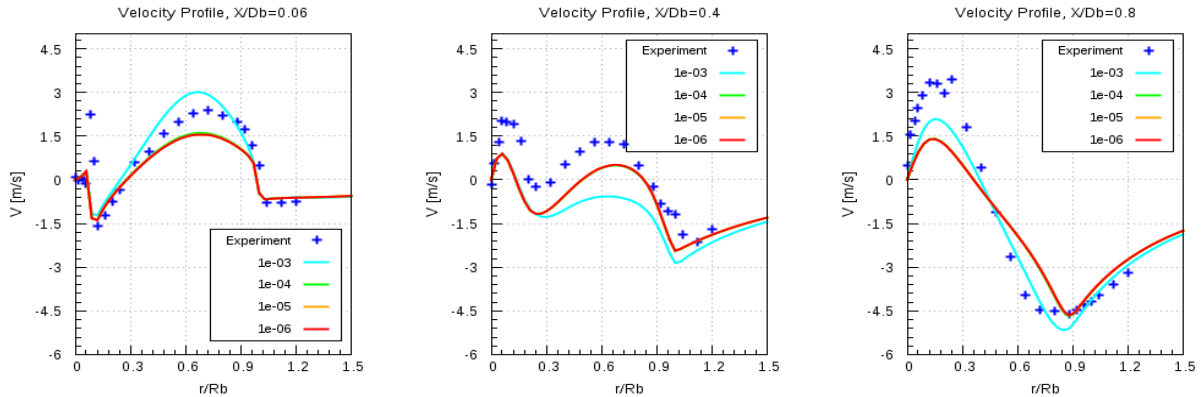


Figure 12.1(c)

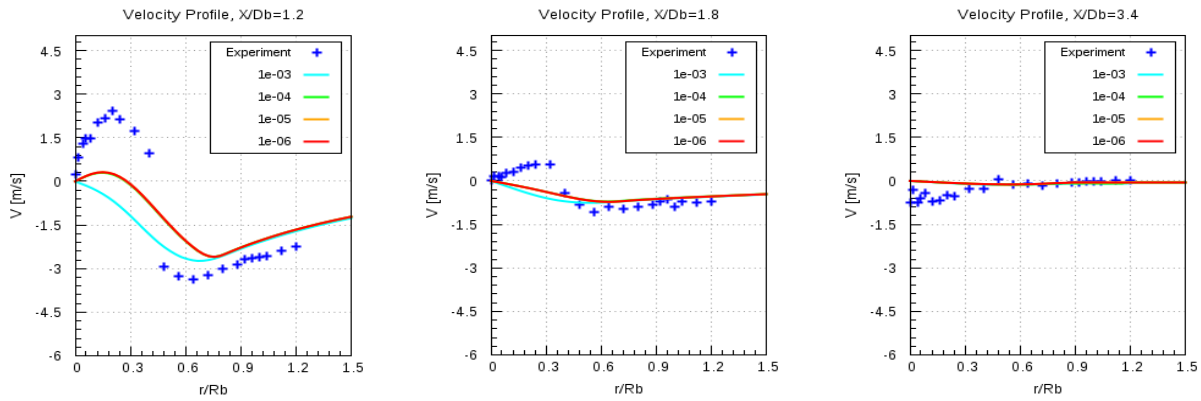


Figure 12.1(d)

Figure 12.1(c) & (d) shows the radial velocity component profiles, plotted against the normalised radial locations, compared with the experimental data. The same behaviour is seen here with the radial velocity component profiles, as pointed out above.

12.1.2 Spatial Discretization Error (Flow field)

This investigation was carried out with the mesh 1, 2, 3 and $k-\omega$ SST model. Pure air was used at both fuel jet and co-flow inlets. The purpose of this study was to obtain the mesh independent results. Conservation and convergence targets were $5 \cdot 10^{-4}$ and 10^{-4} respectively. Results obtained from the simulations, velocity profiles, were compared with the experimental data. Results will only be shown for the data set 2.

Figures 12.2(a) & (b) shows the comparison of the axial velocity component profiles with the experimental data. Here also the comparison does not allow us to select an appropriate mesh resolution. It was decided to choose mesh 2 as the final resolution considering mesh 1 to be too coarse and mesh 3 to be too fine. All meshes deliver mesh independent results. This spatial discretization study has been performed for the Flow field and before choosing the final mesh resolution a spatial discretization study has to be performed for Mixing field.

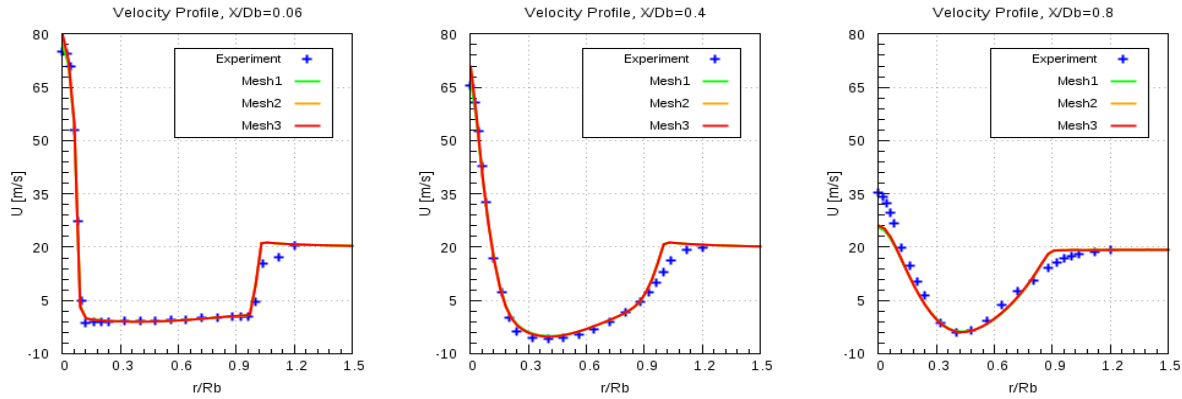


Figure 12.2(a)

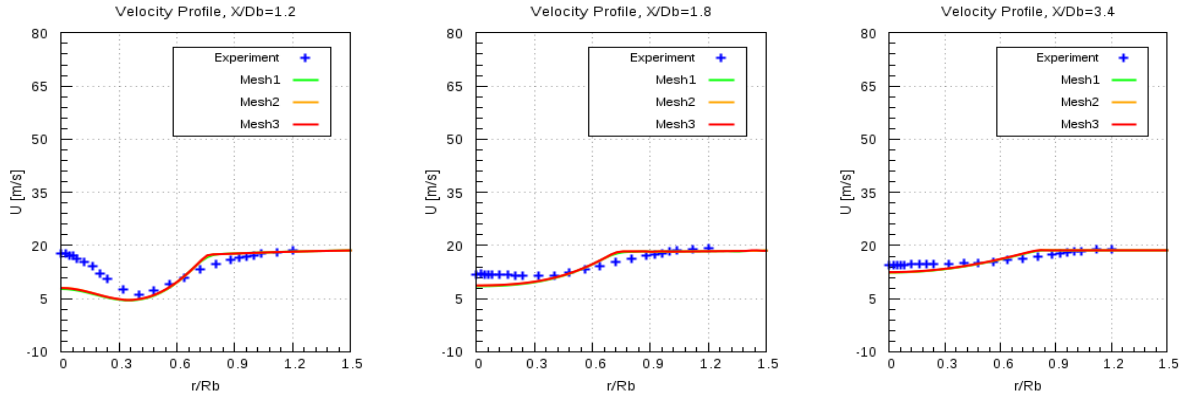


Figure 12.2(b)

12.1.3 Spatial Discretization study (Mixing field)

In this study a combination of different fuels with same velocity 50 m/s have been used at the fuel jet inlet with air flowing at 20 m/s through the co-flow. Mesh 1, 2, 3 and $k-\omega$ SST turbulence model are used for the calculations. The same convergence criteria as mentioned in the previous study has been used here. The comparison of the numerical results will be done with the experimental data for mixing fraction profiles. Table shows the different fuels that were used at fuel jet inlet.

CNG :

In order to obtain correct and trustworthy results a great care was applied to confirm that all the prescribed convergence criteria viz. convergence and conservation target were achieved. Figure 12.3(a) shows the residual values plotted against the number of iterations. Maximum was chosen as the type of residuals. It is seen from the plot that for every quantity the residuals drop even less than the level of 10^{-5} , which is less than what has been a specified criterion of 10^{-4} .

Figure 12.3(b) shows the (%) imbalance in the conserved quantities plotted against the number of iterations. Mass fraction imbalance for fuel is 100 % at outlet, in the beginning, since there is no

fuel at outlet. After 50 iterations the fuel reach the outlet and the imbalances start to reduce and then gradually it will approach to a specified smaller value of conservation target.

In this case the solver will stop only after it either reaches a maximum number of iterations or will achieve all the convergence criteria and stop. Here the residual convergence history and Imbalance monitors are only shown for mesh 2. For other meshes it can be found in Appendix.

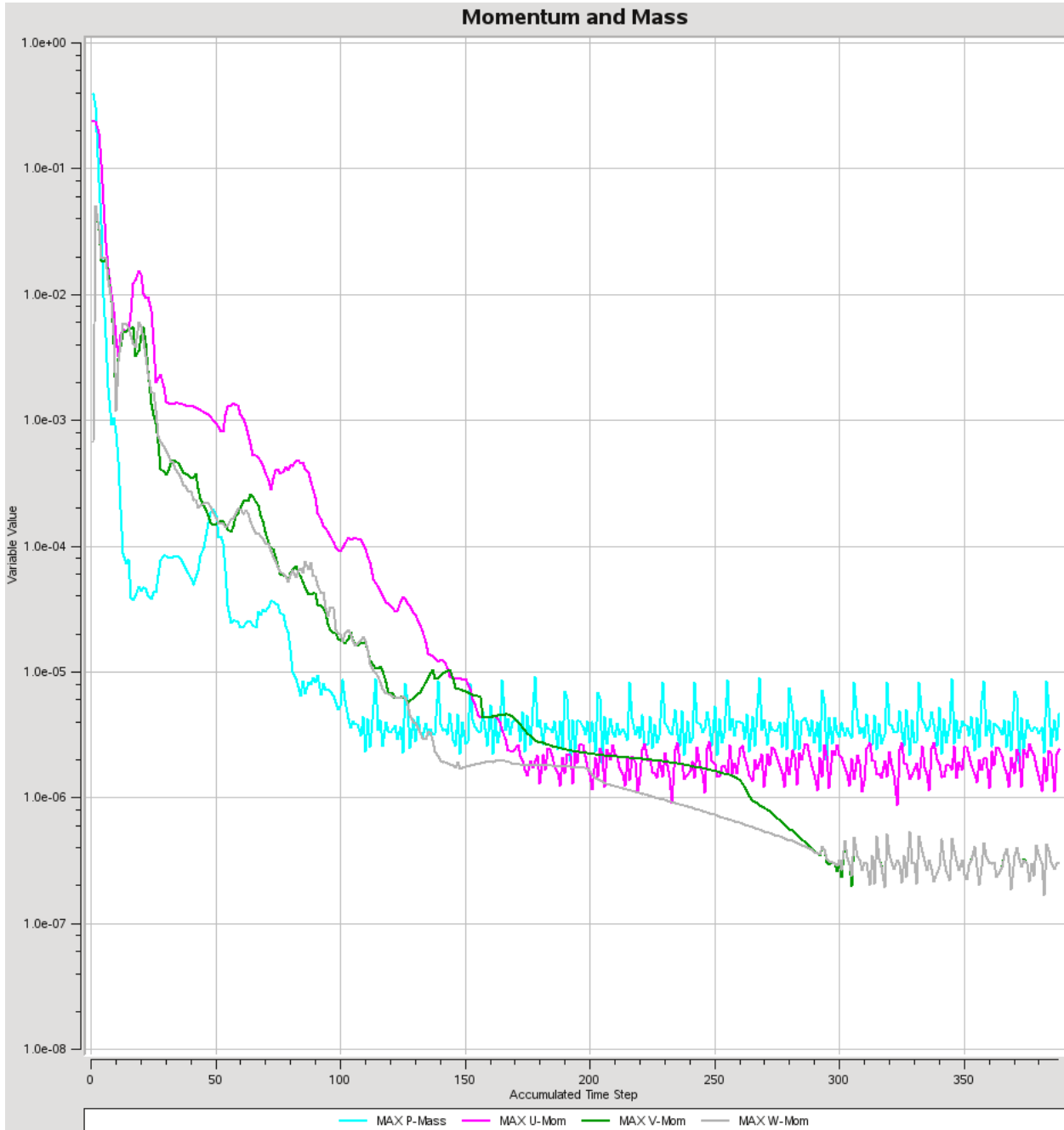


Figure 12.3(a)

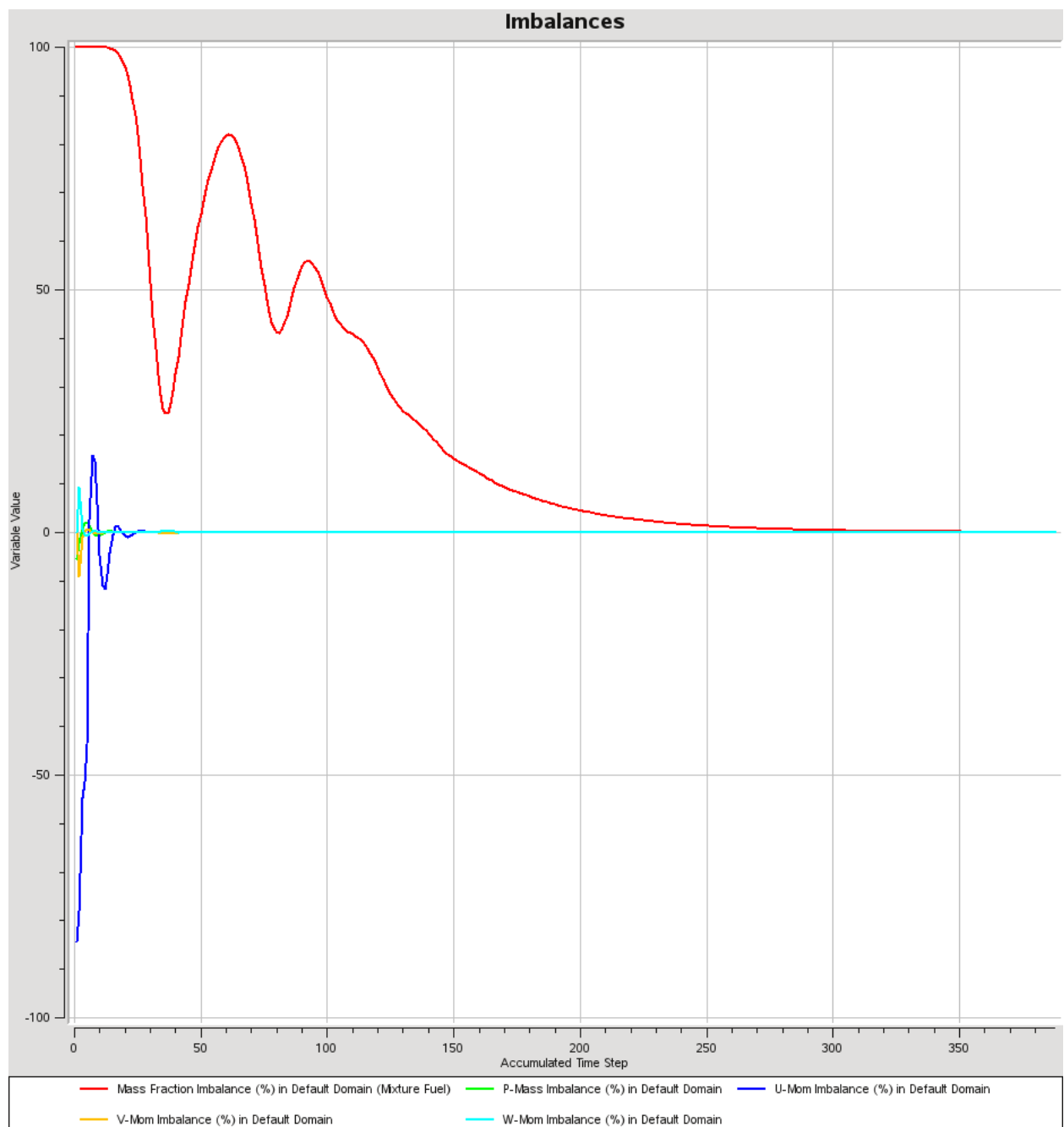


Figure 12.3(b)

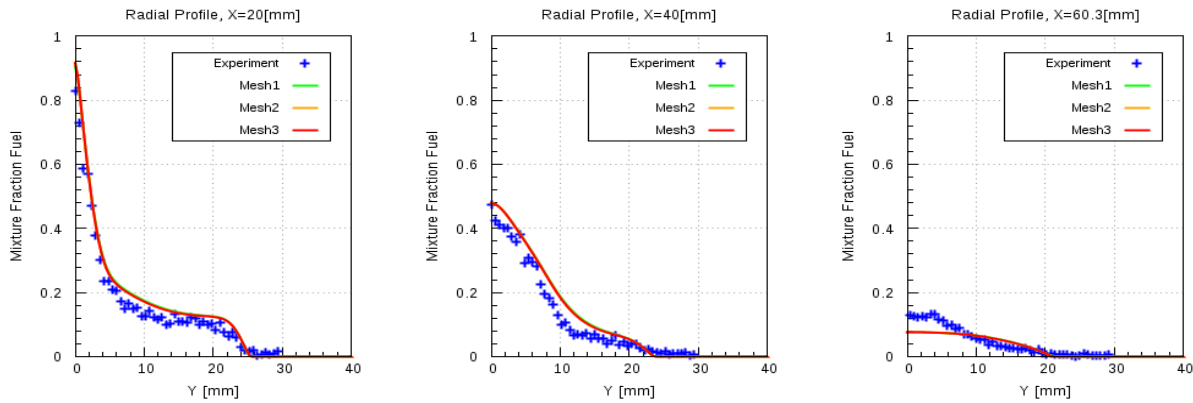


Figure 12.3(c)

Ethylene:

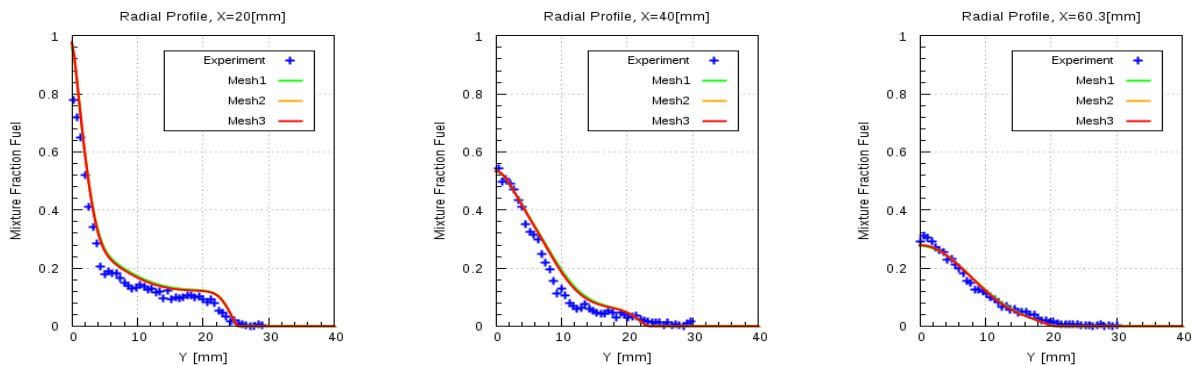


Figure 12.3(d)

LPG:

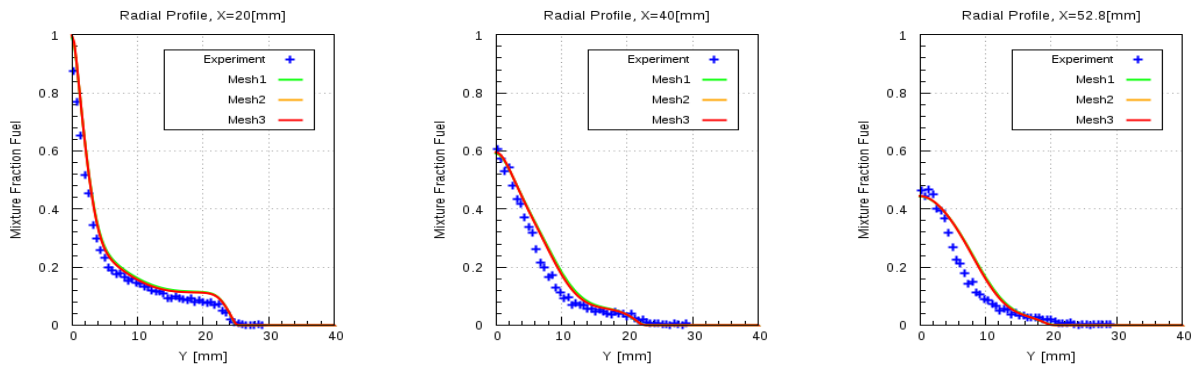


Figure 12.3(e)

Figure 12.3(c)-(e) shows the comparison of the mixture fraction profiles obtained from numerical results and are compared with the experimental data. The mixture fraction profiles of all meshes overlap over one another. All meshes achieved the specified convergence criteria. For the same reasons mentioned in the previous spatial discretization study applies here also and mesh 2 was chosen to be the final mesh resolution to carry out further investigation.

12.1.4 Model Error Study

The following table shows the array of the simulations that had been carried out, for all mesh resolutions, in this study.

Model	Fuels	Velocity
k- ω SST, Standard k- ϵ	CNG	50
		85
		143
	Ethylene	50
	63	
	80	
	LPG	50
	70	

Table 12

Model Error study was performed with k- ω SST and standard k- ϵ turbulence models. The comparison of the radial mixture fraction profiles obtained from the numerical results will be compared with the experimental data and will be shown only at the locations X = 20, 40 and 60.3 [mm]. Here the comparison will only be shown for the mesh 2, which is the selected mesh resolution, for fuels CNG and Ethylene with $U_J = 50$ m/s. Other comparisons can be found in Appendix. All simulations achieved the specified convergence criteria.

CNG:

$$U_J = 50 \text{ m/s}$$

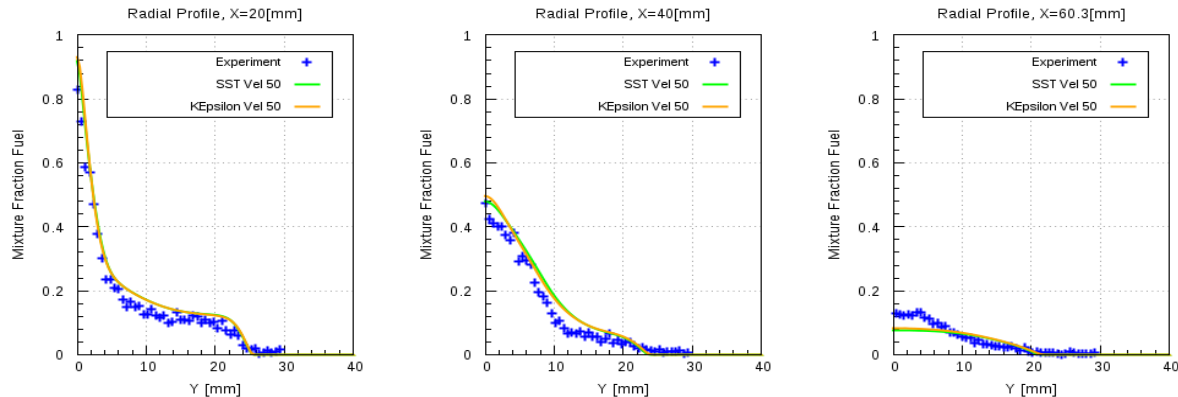


Figure 12.4(a)

Figure 12.4(a) shows the comparison of the radial mixture fraction profiles for the numerical results of CNG fuel at $U_J = 50$ m/s and experimental data. The numerical mixture fraction profiles for both models are in good agreement with each other as well as with the experimental data, but at certain intermediate locations in the domain a noticeable difference between the two models was observed. Figure 12.4(b) shows the locations, between which the differences in the model prevails. Figures 12.4(c)-(e) shows the plots where this difference was observed.

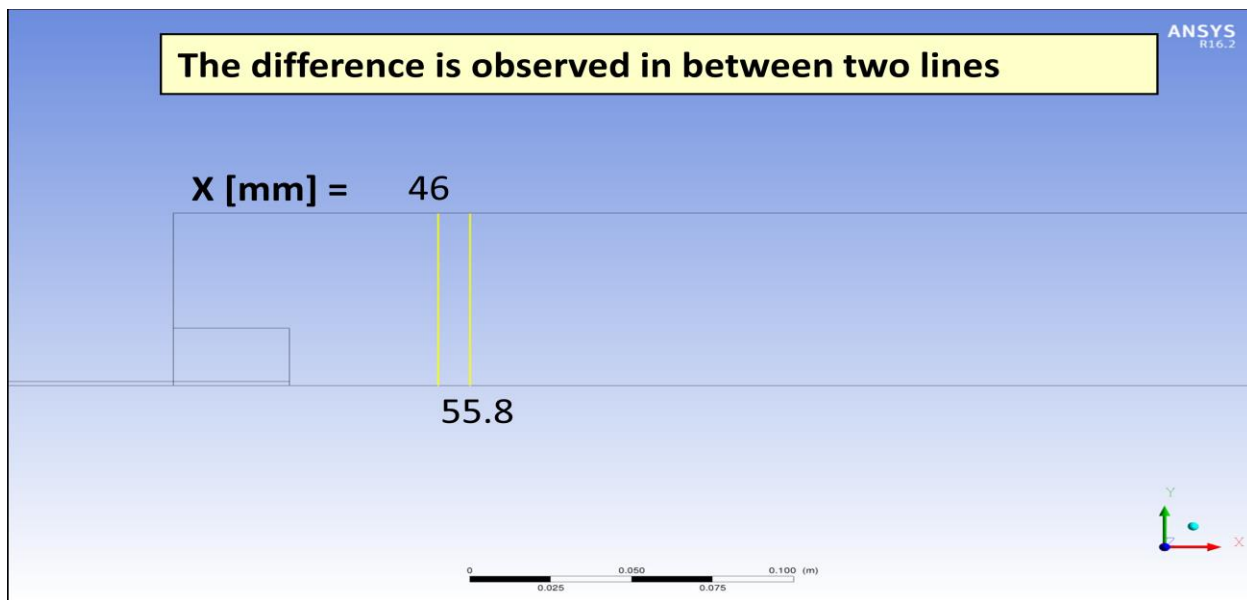


Figure 12.4(b)

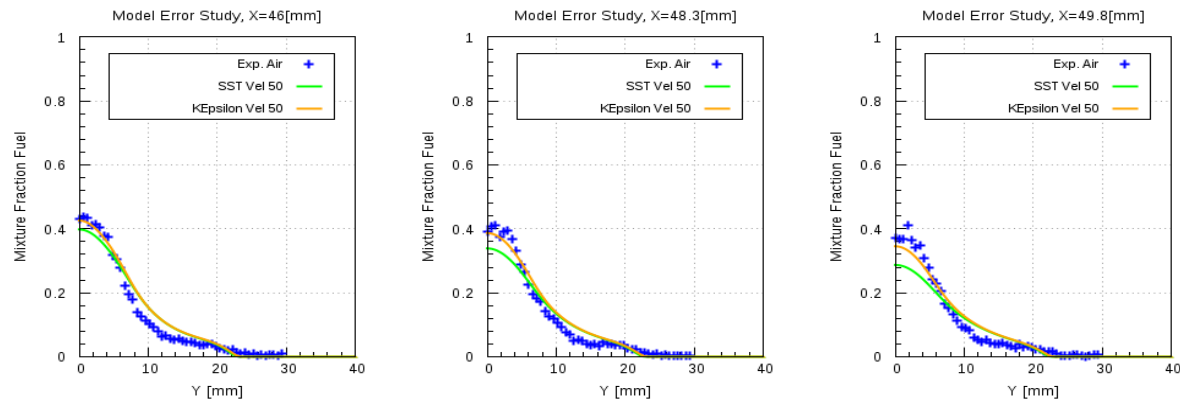


Figure 12.4(c)

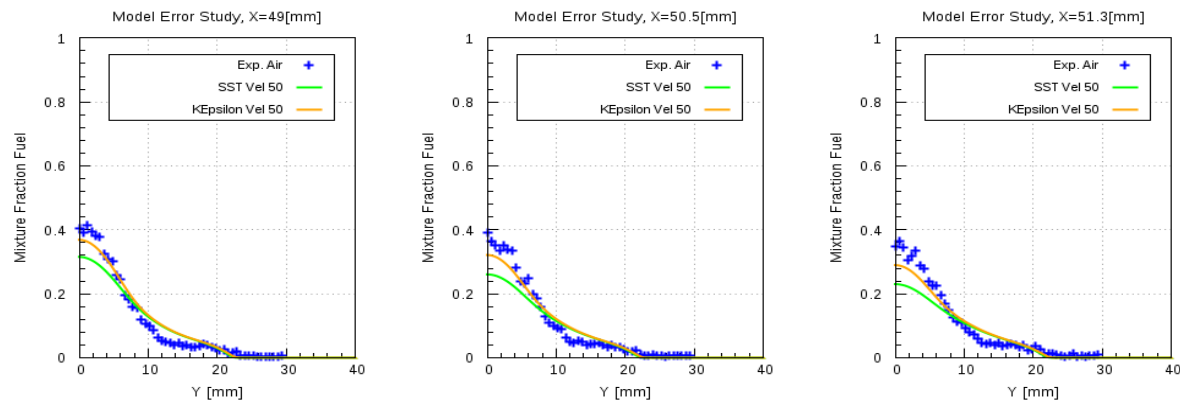


Figure 12.4(d)

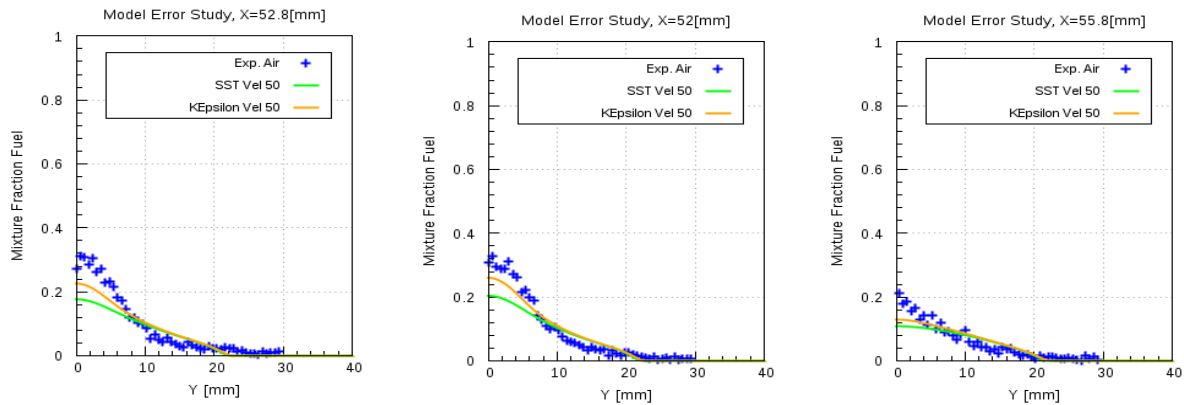


Figure 12.4(e)

It is seen from the figures that the difference is existing at certain locations, but then it continues to reduce further on to deliver almost identical profiles.

From the figure 12.4(f), a double-vortex structure is seen in the recirculation zone which controls the flow and mixing patterns: an inner vortex near to the fuel jet and an outer vortex which lies in between the inner vortex and the co-flow air. The outer vortex is larger and extends up to 70% of the bluff-body diameter radially and around one bluff-body diameter axially. The inner vortex is narrower and its centre core shifts downward with the change of the flow conditions at fuel jet inlet.

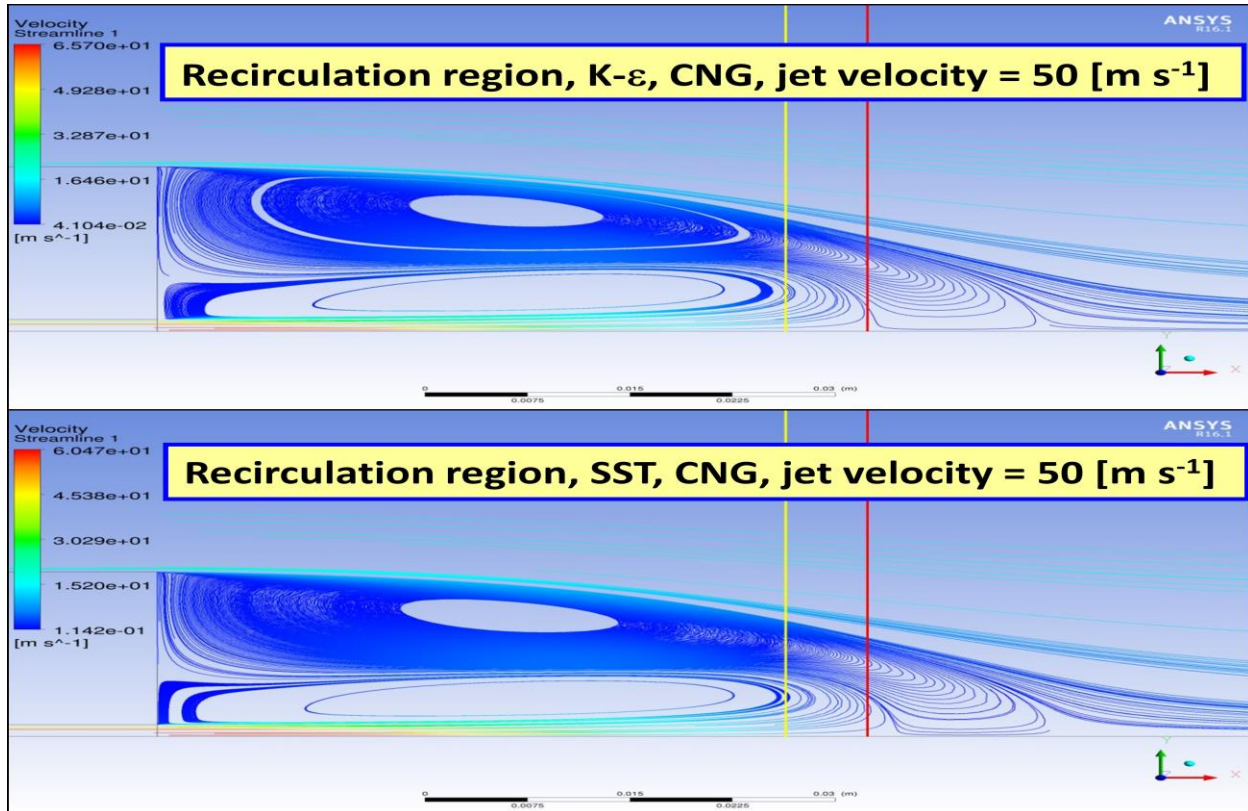


Figure 12.4(f)

Figure 12.4(f) also shows the comparison of the streamlines for k- ω SST, standard k- ϵ model along with the locations at which the differences were observed. The comparison of the streamlines for both the models showed that they predict different length of recirculation zone, defined as the axial location at which the co-flowing air reaches a stagnation point [8]. Yellow and red lines indicate the beginning and the end of the region in between which both the models showed noticeable differences in the mixture fraction profiles. It can be seen that for the same measurement location different values of mixture fraction are predicted and the reason is the k- ϵ model predicts a bit longer recirculation region as compared to the k- ω SST model. Fig. 12.4 (g) shows the comparison of the mass fraction contours for k- ω SST and standard k- ϵ model. It is seen from the plots that the mixing is slightly overpredicted by the k- ω SST model compared to the standard k- ϵ model. Overprediction is seen only in a small region in between yellow and red line.

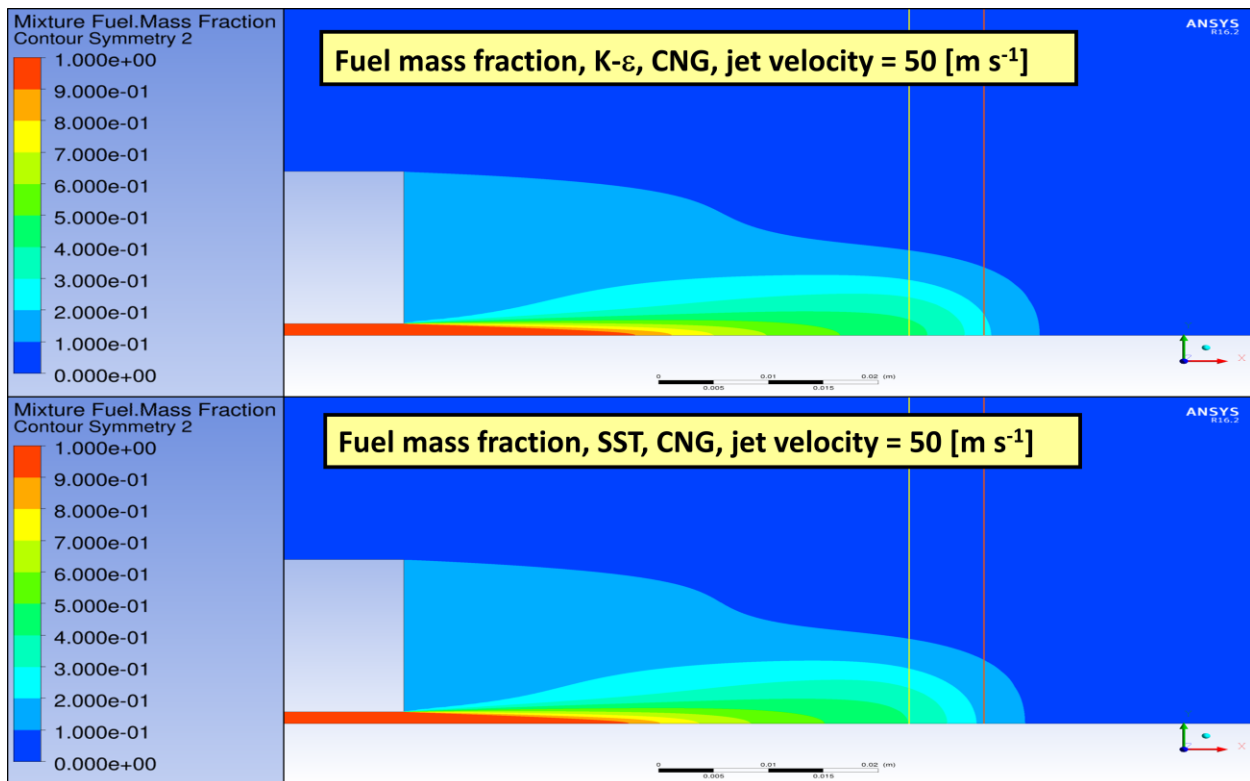


Figure 12.4(g)

Ethylene

Figure 12.4(h) shows that the radial mixture fraction profiles of k- ω SST and standard k- ϵ models compared with the experimental data. Ethylene is used as fuel at jet inlet with $U_J = 50$ m/s. Both models show good agreement to the experimental data and are consistent with each other as well. Figure 12.4(i) shows the comparison with the streamlines generated from the experimental data and the streamlines obtained from numerical results using two different turbulence models. It is seen from the plots that the mixture fraction profiles are in good agreement with each other as well as the experimental data.

$$U_J = 50 \text{ m/s}$$

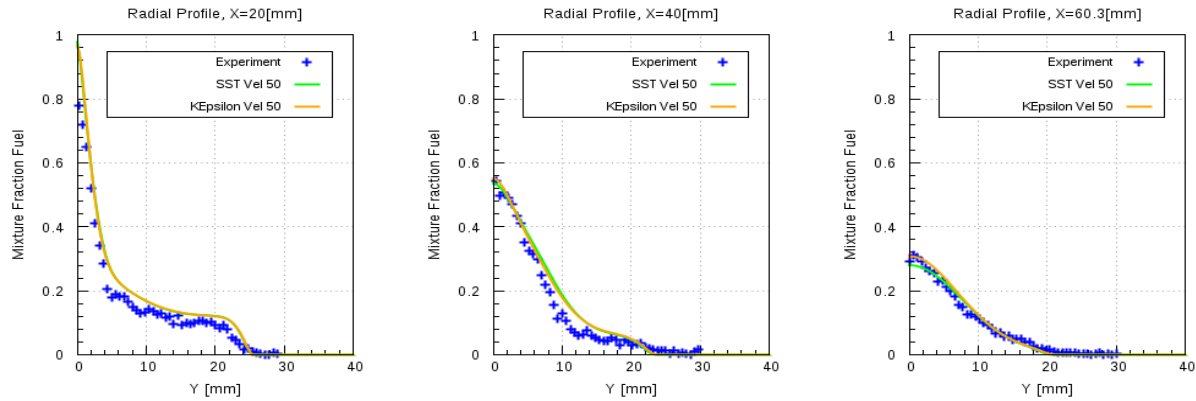


Figure 12.4(h)

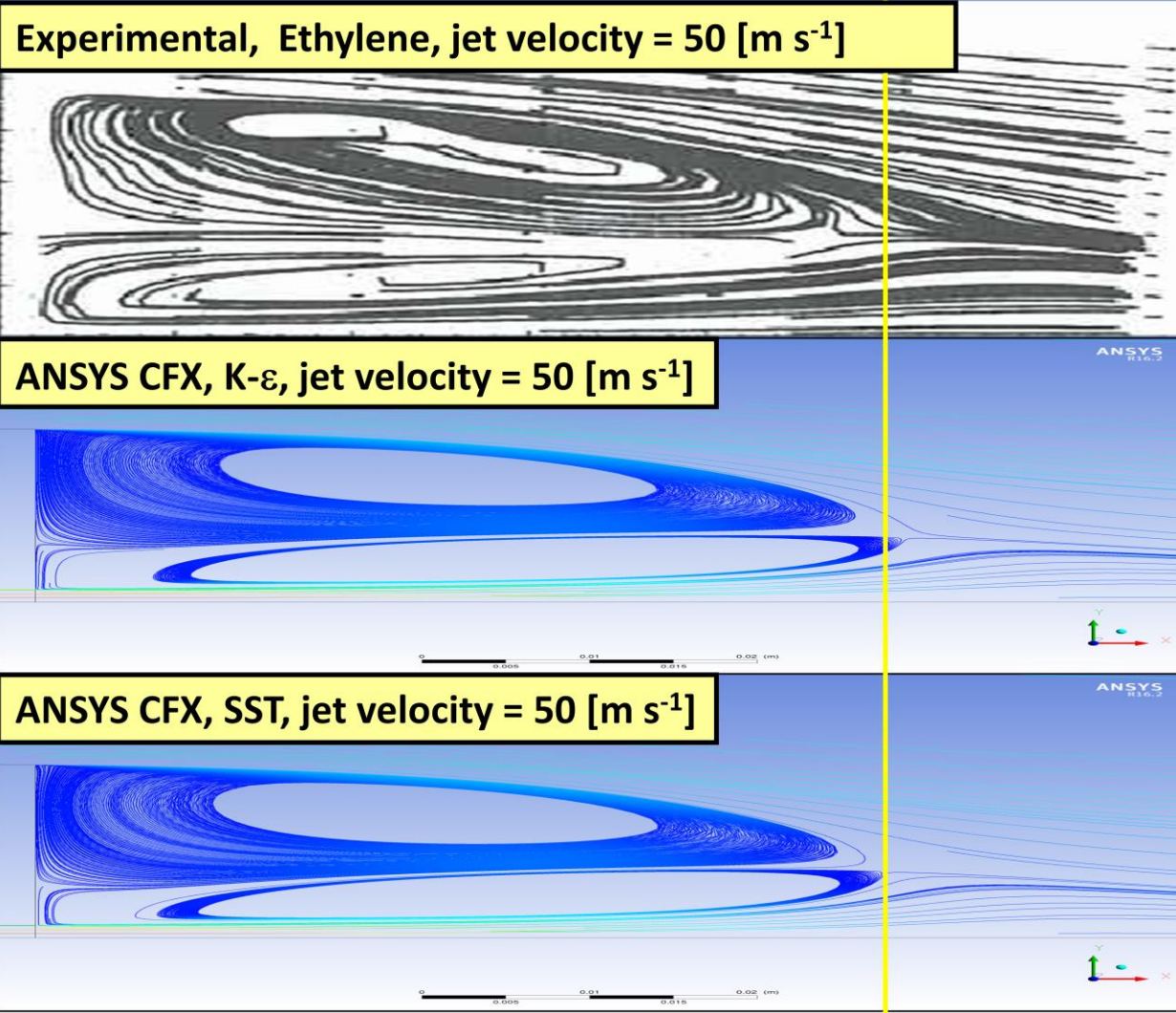


Figure 12.4(i)

Comparison in figure 12.4(i) shows two fully developed vortices in the recirculation zone and mainly they are showing the same orientation as shown by the experimentally generated vortices, a little bit over-predicted in case of k- ϵ model. The length of the recirculation zone extends upto one D_B [7] and the same is being observed from the numerical results.

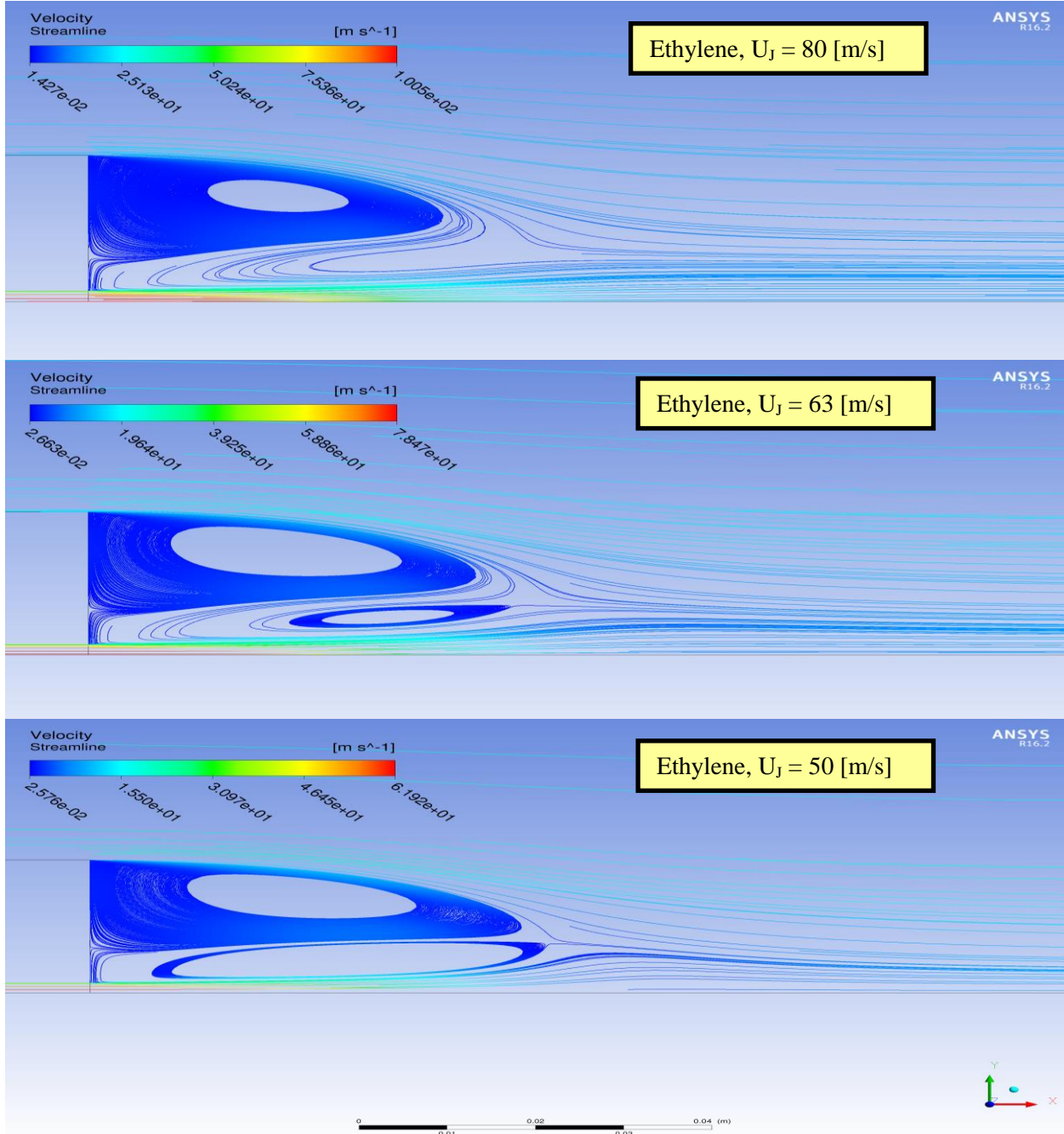


Figure 12.4(j)

Figure 12.4(j) shows the comparison of streamlines generated with different fuel jet velocities viz. 50, 63 and 80, with fuel Ethylene. It is apparent that the flow field in the lower (50 m/s) and

intermediate jet velocity (63 m/s) flows shows a double-vortex structure in the recirculation zone, while in the high-velocity (80 m/s) case the inner vortex has almost lost its circulation pattern. In the intermediate jet velocity case, the central core of the inner vortex shifts downstream the bluff body, and in the high jet velocity case this shift continues until the inner vortex disappears and part of the gases circulated back by the outer vortex is convected downstream. The same phenomenon occurs for other fuel mixtures and the transition from double- to single-vortex structure occurs at different jet velocities.

12.2 ANSYS Fluent 17.0

The same studies as in ANSYS CFX 16.1 were carried out with ANSYS Fluent 17.0. From the iteration and spatial discretization error study, RMS Residual $< 10^{-7}$ was chosen as the convergence criteria and mesh resolution of mesh 2 respectively. Here only the results of model error study will be discussed.

12.2.1 Model Error Study

This study was carried out with $k-\omega$ SST model, standard $k-\epsilon$ and realizable $k-\epsilon$ model, the results were compared with each other as well as with the experimental data. The results shown here would be only for the mesh 2. Table shows the array of simulations carried out for this study.

Model	Fuels	Velocity
k- ω SST, standard k- ϵ , realizable k- ϵ model	CNG	50
		85
		143
Ethylene	Ethylene	50
		63
		80
		50
		70
LPG	LPG	50
		70

Table 13

CNG:

$$U_J = 50 \text{ m/s}$$

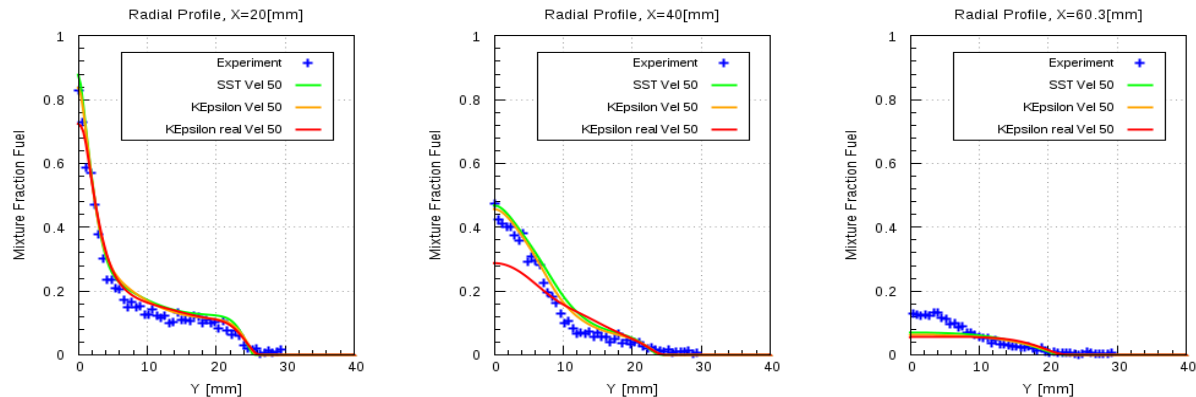


Figure 12.5(a)

Figure 12.5(a) shows that the comparison of the radial mixture fraction for the numerical data for CNG at $U_J = 50$ m/s, compared with the experimental data. Mixture fraction profiles for $k-\omega$ SST and standard $k-\epsilon$ are in good agreement with the experimental data and consistent with each other, but realizable $k-\epsilon$ model over-predicts the mixing significantly downstream $X > 40$ [mm]. It predicts that jet has sufficiently mixed with the surrounding air by downstream location $X = 46$ [mm]. Figure 12.5(b) shows the locations where the mixing is over-predicting by the realizable $k-\epsilon$ model. The difference start to reduce between the profiles, when the other models start to predict that the jet has sufficient mixed or the diffusion of jet has occurred.

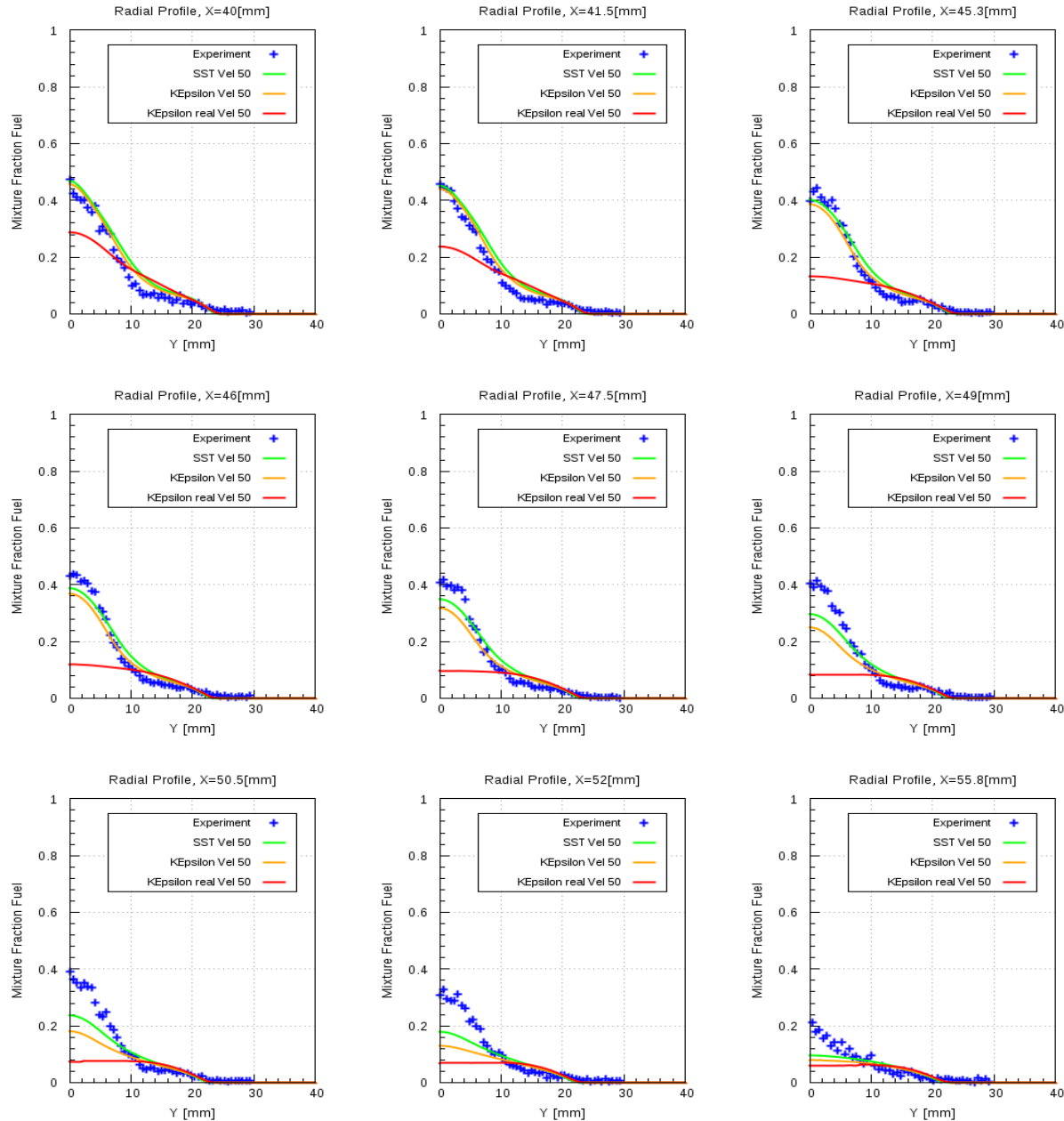


Figure 12.5(b)

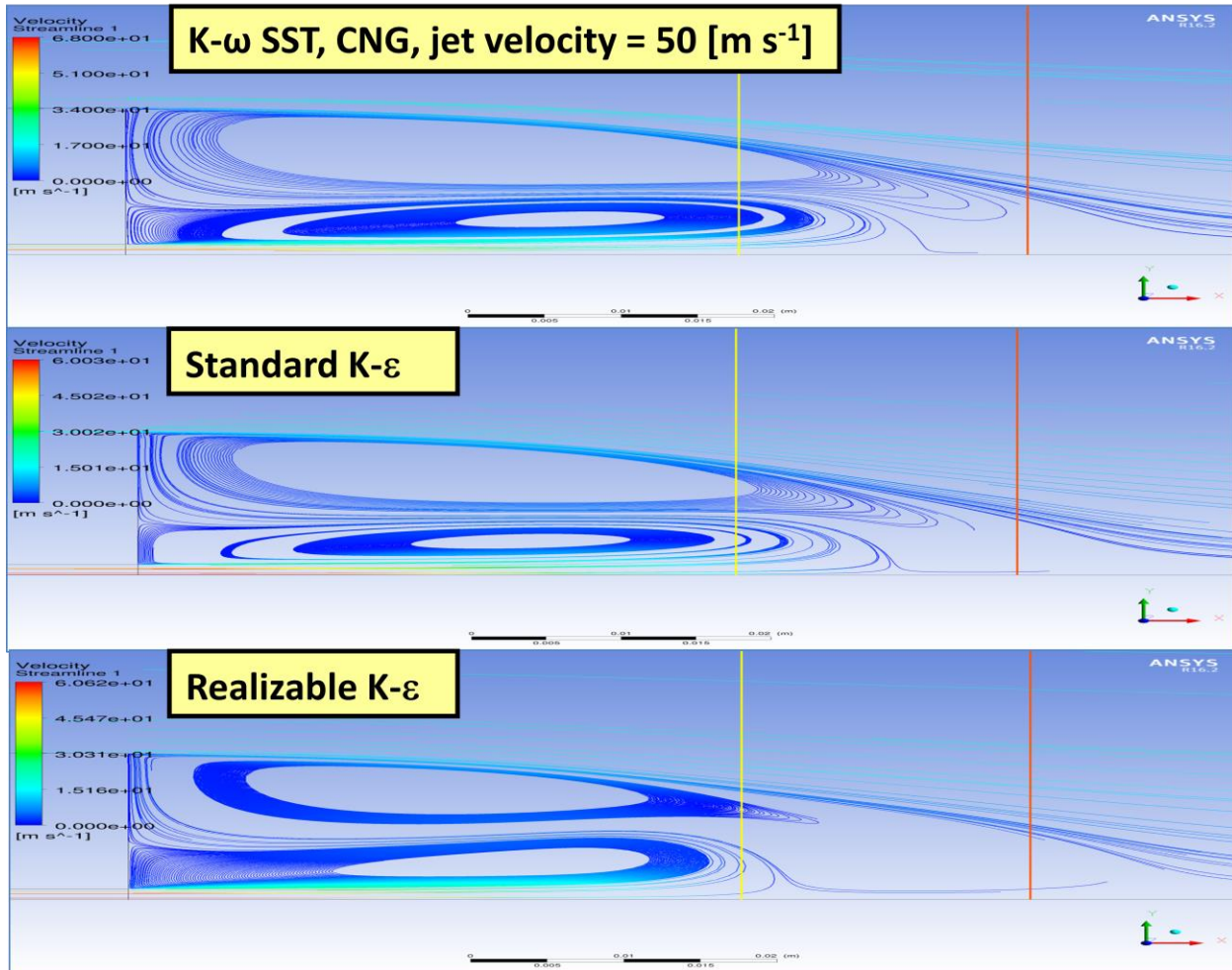


Figure 12.5(c)

Figure 12.5(c) shows the comparison of the stream lines for all three models. Yellow and red lines indicate the region in between which the differences in the mixture fraction profiles are observed.

All three models predict different length of recirculation zones. As seen the realizable k- ϵ model Predicts the smallest length of recirculation zone compared to the other two models. Also the orientation of the smaller vortex near the jet is tending more upwards, rather than extending in the downstream direction.

Figure 12.5(d) shows the comparison of the mass fraction contour plots for all three models. It is seen from the comparison that standard k- ϵ model over-predicts the mixing slightly, but realizable k- ϵ model over-predicts the mixing significantly.

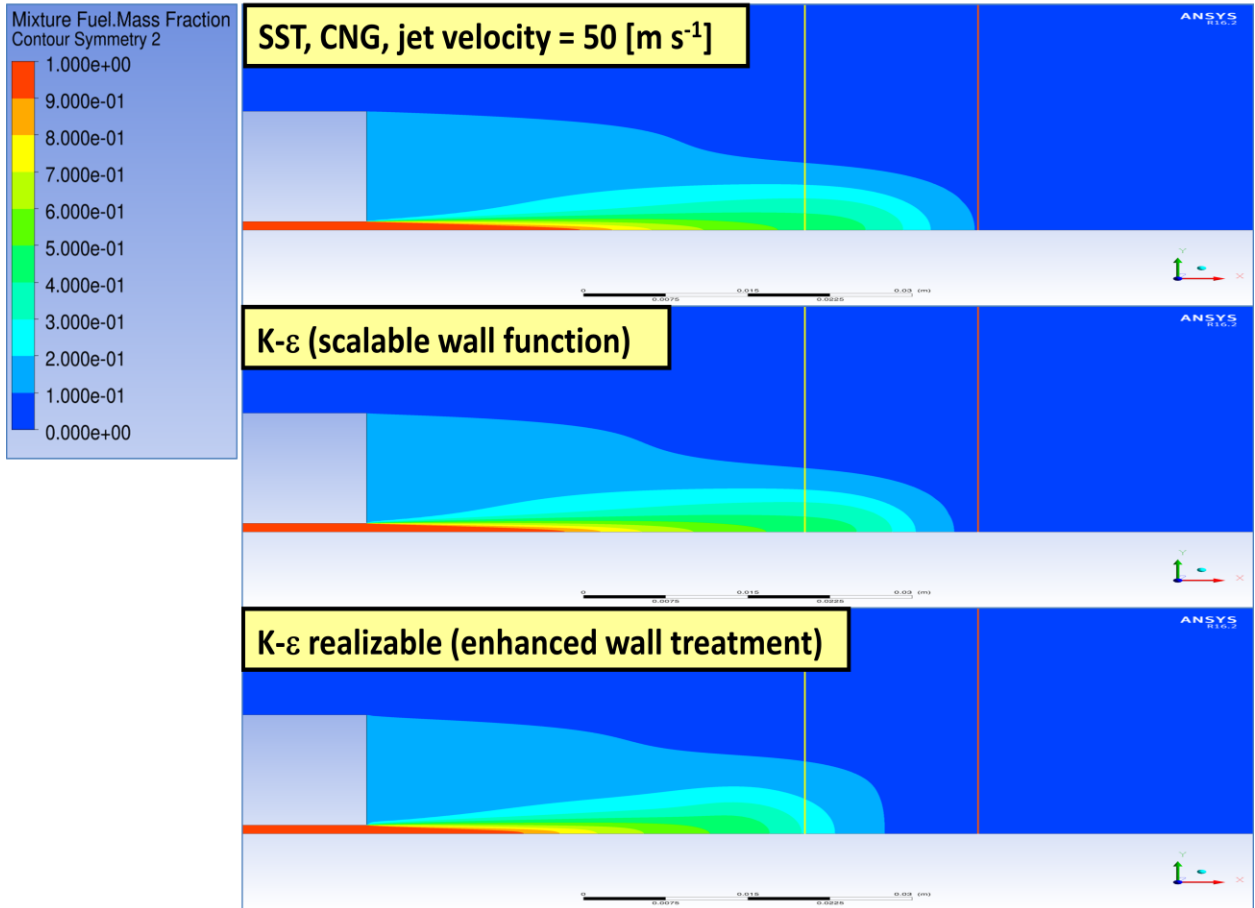


Figure 12.5(d)

Ethylene

Figures 12.5(e)-(g) shows radial profiles of the mean mixture fraction at different axial locations for the low (50 m/s), intermediate (63 m/s) and highest (80 m/s) jet velocity flows. Simulations from the all the three turbulence models are also plotted for the same axial locations. The agreement between measurements and computations, with intermediate and highest jet velocities is similar to that observed for the low-velocity jets.

From figure 12.4(j), it is clear that the transition from double to single vortex in the recirculation zone occurs between these intermediate and highest jet velocities. However, from figures 12.5(e)-(g) it is also apparent that the changes in the structure of the flow pattern in the recirculation zone and the downward shift of the inner vortex have minor effects on the mixing field close to the bluff-body i.e. the jet with the highest velocity is sharper compared to the other two velocities. It is worth noting that the transition from the closed to the open vortex structure by itself does not have a major effect on the flow and mixing fields. The same can be observed for fuel LPG, from figures 12.5(h)-(i) where the comparison of the mean mixture fraction with the experimental data is done. Apart from that in all cases realizable k- ϵ model over-predicts the mixing in comparison to the other models and the experimental data as well.

$U_J = 50 \text{ m/s}$

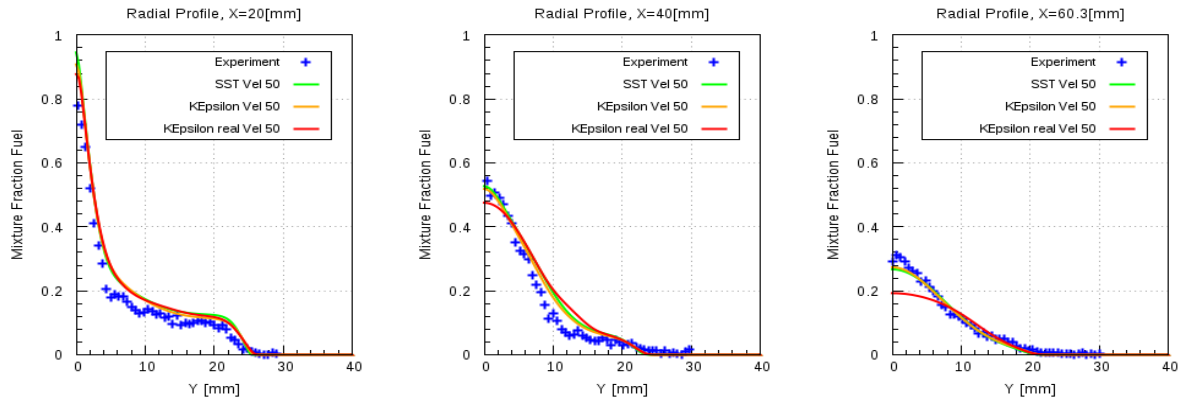


Figure 12.5(e)

$U_J = 63 \text{ m/s}$

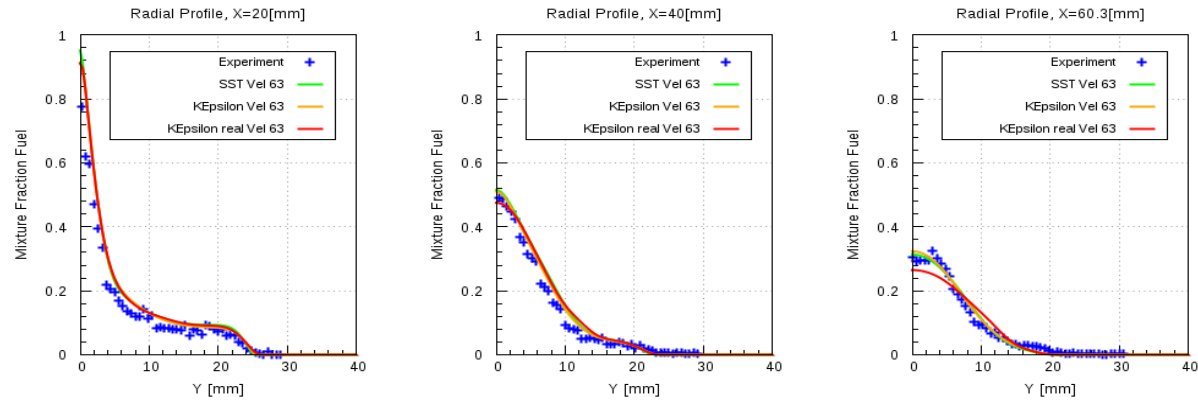


Figure 12.5(f)

$U_J = 80 \text{ m/s}$

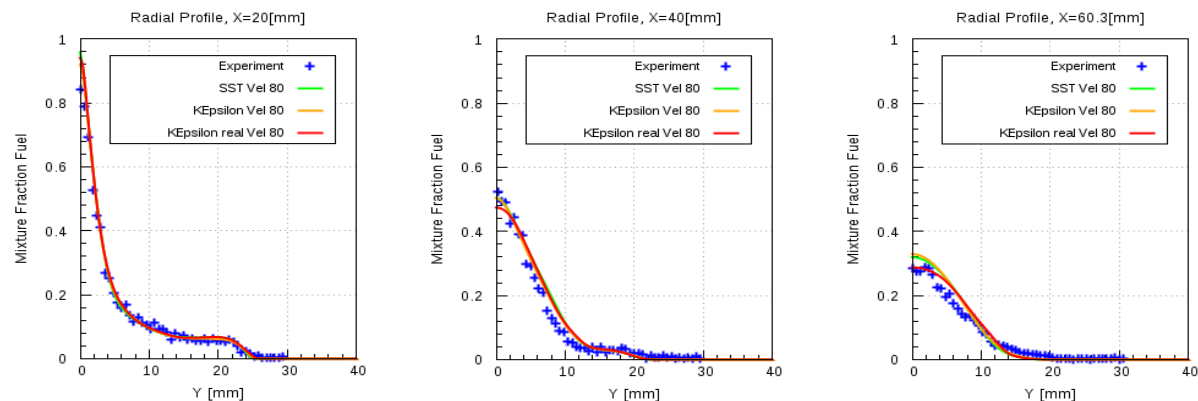


Figure 12.5(g)

LPG

$U_J = 50 \text{ m/s}$

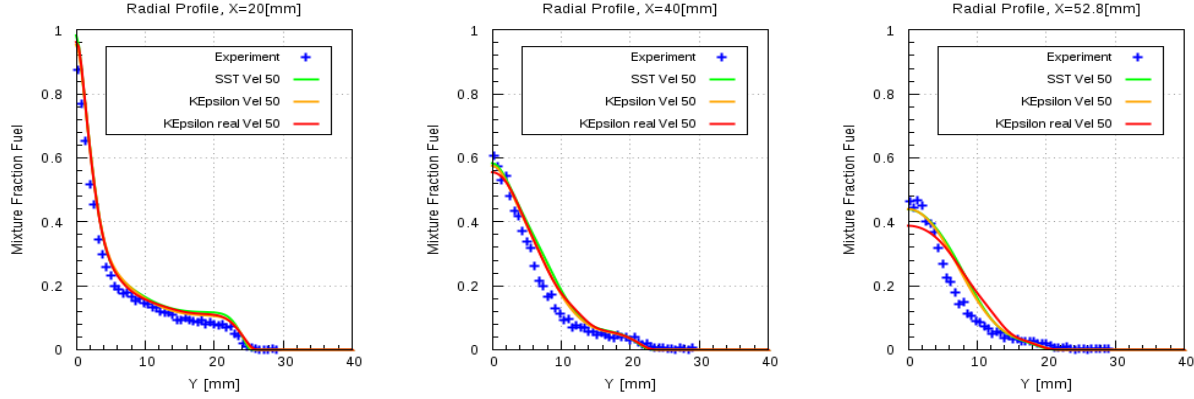


Figure 12.5(h)

$U_J = 70 \text{ m/s}$

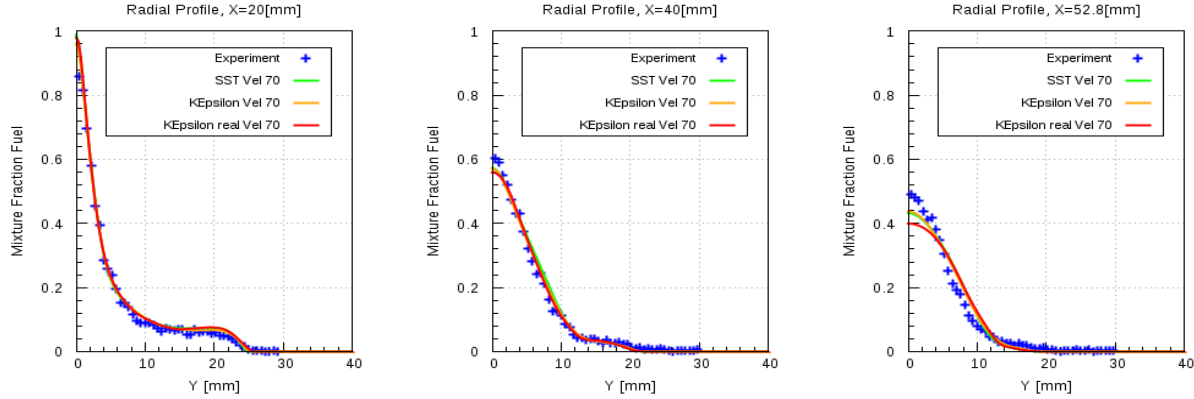


Figure 12.5(i)

12.3 Solver comparison between ANSYS CFX 16.1 and ANSYS Fluent 17.0

In this study a comparison of the results obtained from the turbulence models of the two solvers, with each other as well as with experimental data, is carried out. This comparison is only performed with the mixing field data. The comparison of the standard $k-\epsilon$, realizable $k-\epsilon$ and $k-\omega$ SST models from ANSYS Fluent 17.0 will be done with standard $k-\epsilon$ and $k-\omega$ SST models of ANSYS CFX 16.1 respectively. Figure 12.6(a) shows the radial mixture fraction profiles of the numerical results compared with the experimental data. It is seen that the standard $k-\epsilon$ models of both the solvers are in good agreement with the experimental data. Also they both deliver almost consistent results to each other. Realizable $k-\epsilon$ model over-predicts the mixing significantly from the axial location $X = 40$ [mm] and continues to do so until the location $X = 58.8$ [mm]. Justification for the same was obtained from the comparison of the mixture fraction contours. Streamline comparison showed that realizable $k-\epsilon$ model under-predicts the length of recirculation zone (Shown in Appendix)

12.3.1 CNG

12.3.1.1 k- ϵ model

$$U_J = 50 \text{ m/s}$$

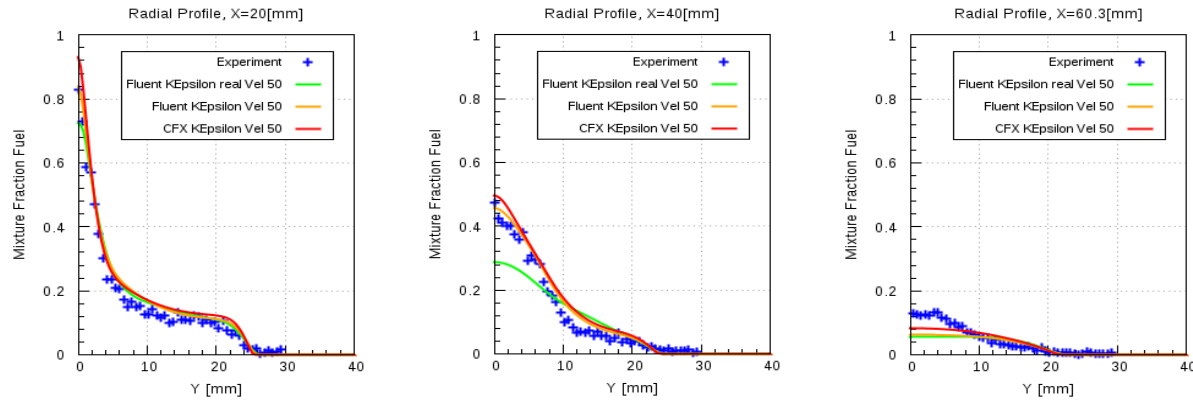


Figure 12.6(a)

$$U_J = 85 \text{ m/s}$$

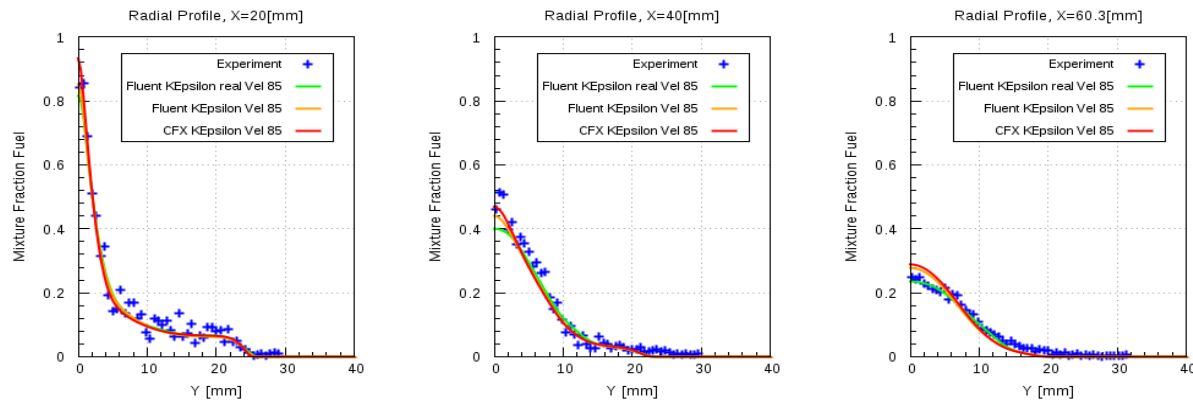


Figure 12.6(b)

$$U_J = 143 \text{ m/s}$$

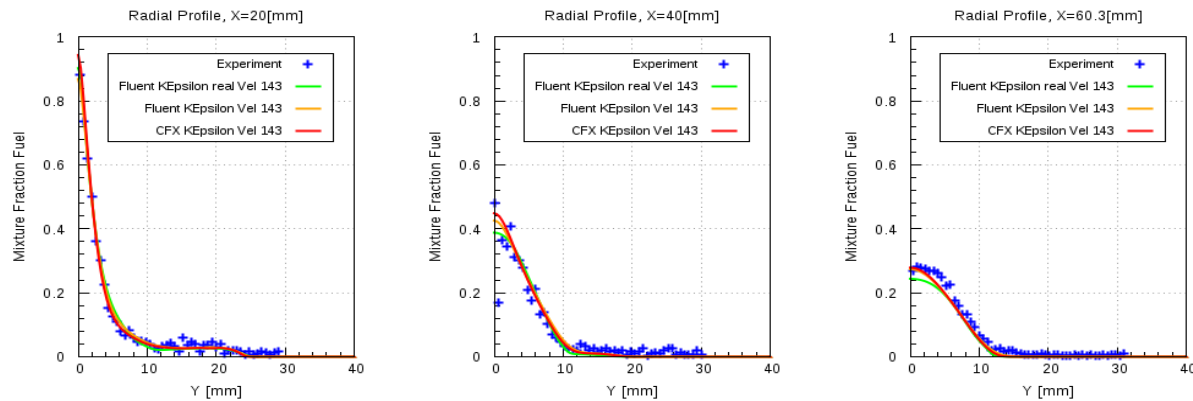


Figure 12.6(c)

From figure 12.6(b)&(c) it can be seen that with the same fuel, but with different momentum at the jet inlet, realizable k- ϵ model does not over-predicts the mixing as significantly as it does in the case of $U_J = 50$ m/s. Apart from that standard k- ϵ model for both solvers are consistent with each other and are in good agreement with the experimental data.

From the figure 12.6(d)-(f) it can be seen that the radial mixture fraction profiles for the k- ω SST models for both the solvers are consistent with each other and are in good agreement with each other.

12.3.1.2 k- ω SST model

$$U_J = 50 \text{ m/s}$$

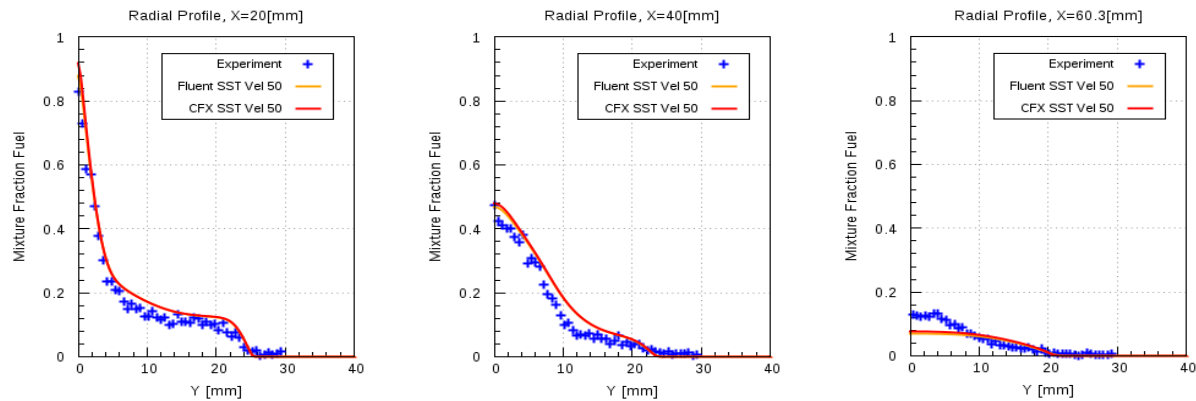


Figure 12.6(d)

$$U_J = 85 \text{ m/s}$$

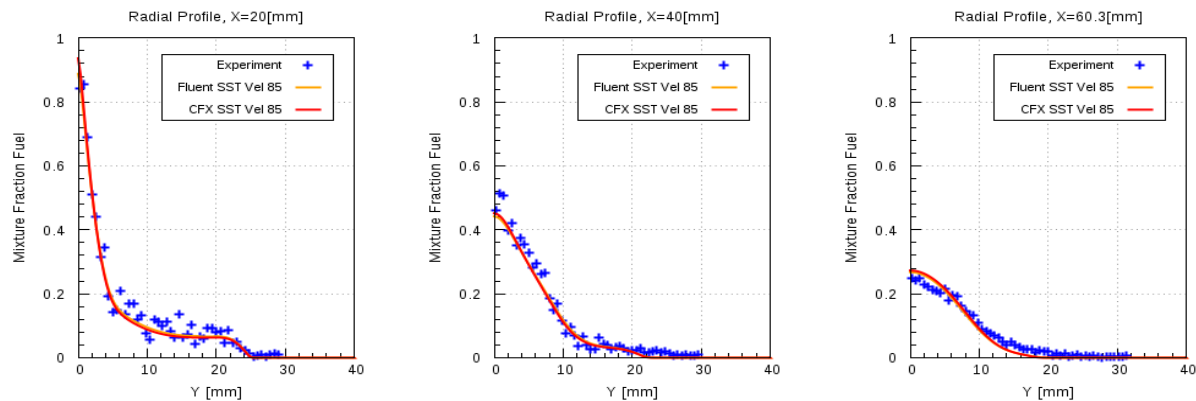


Figure 12.6(e)

$$U_J = 143 \text{ m/s}$$

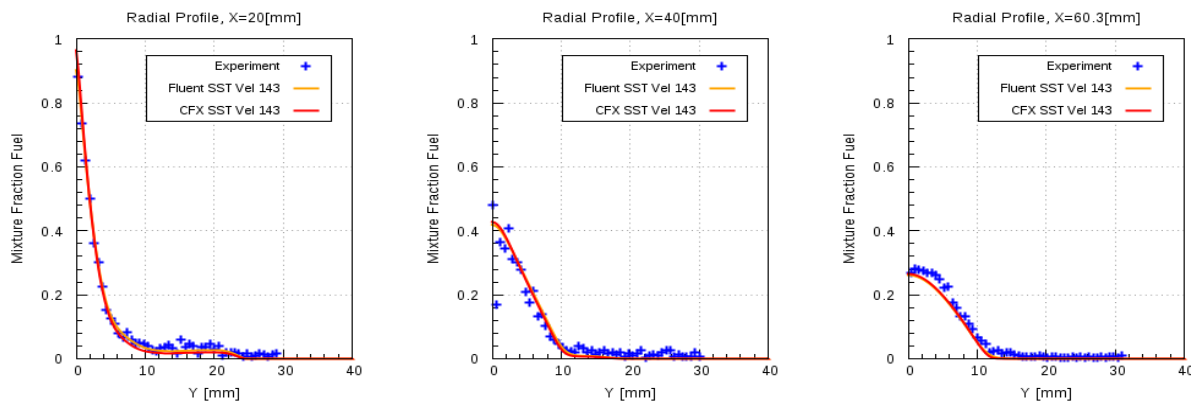


Figure 12.6(f)

13 Conclusions

Both test cases were carried out with the purpose of investigating the turbulent mixing of species in the recirculation zone behind the bluff body, carried out with isothermal and steady state flow conditions.

13.1 Sandia Propane jet

Mesh independent solutions were achieved on both mesh 3 and 4. Radial profiles of propane mass fractions were in good agreement with the experimental data, but the axial velocity component (U) profiles showed some noticeable difference when compared with the experimental data. The first profile of the radial velocity shows good agreement with the co-flow seeded experimental data. Further downstream it is under-predicted. However, there is considerable uncertainty in the experimental data, which is seen by the large discrepancies between the jet and co-flow seeded data, which reduces towards the outlet. A small recirculation region is visible behind the bluff body with one complete vortex and a small incomplete vortex. The reason explaining the incomplete vortex is the available space, for the other vortex to develop, is too less.

Turbulent inlet boundary condition study was performed to testify the assumed turbulent inlet boundary conditions with the other possible boundary conditions. Apart from that the famous round jet anomaly phenomenon for the round jet/plane jet was also included in this study. As sometimes recommended in scientific literature the correction of $C\epsilon_1=1.6$ in the $k-\epsilon$ equations was applied. But the results show clearly, that the improvement made in the comparison of radial velocity profiles for the round jet is paid for by a deterioration of the Propane jet diffusion, where results became substantially worse by that $k-\epsilon$ model modification. Other $k-\omega$ SST model, in combination with different turbulent inlet boundary conditions, did not show any noteworthy improvement in comparison with the experimental data.

Model error study with ANSYS CFX 16.1 showed that the $k-\omega$ SST and standard $k-\epsilon$ model showed consistent results with each other and are in good agreement with the experimental data. Modified $k-\epsilon$ model showed improvement in the velocity profiles, but over-predicts the propane mass fraction profiles. With ANSYS Fluent 17.0 two diffusivities were used in combination with the turbulence models. It turned out that both diffusivities delivered identical results and their profiles overlapped each other, as seen from the comparison plots. Both $k-\omega$ SST and standard $k-\epsilon$ model are in good agreement with each other and with the experimental data.

In comparison of ANSYS CFX 16.1 and ANSYS Fluent 17.0, $k-\omega$ SST and standard $k-\epsilon$ model (with different diffusivities in ANSYS Fluent 17.0) were used. Both models showed good agreement with each other and the experimental data as well.

In summary, both $k-\epsilon$ models (ANSYS CFX 16.1 & ANSYS Fluent 17.0) give almost the same level of accuracy in this investigation, but with more observed difficulties in obtaining a converged solution. Hence $k-\omega$ SST model would be the recommended turbulence model for the turbulent mixing of the non-reacting species in the jet. Turbulent Schmidt number for the transport equation of species should be 0.9, which is the default value in ANSYS CFX 16.1. In certain region of the domain there is a quite big difference in the results as compared to the

experimental results, which is due to the simplifying assumptions made in the RANS turbulence models i.e. isotropic turbulence and the well known so-called “round jet anomaly” for RANS models. If desired, higher accuracy results can be obtained with e.g. Large Eddy Simulation (LES) or hybrid models, but at much higher computational costs.

13.2 Sydney Bluff Body

Obtained numerical results are compared with the available experimental data and also obtained results are compared in ANSYS CFD Post to deduce certain conclusions. Iteration error and spatial discretization studies were performed to remove all the associated numerical errors. Mesh independent solutions were obtained on all mesh resolutions. Radial velocity profiles were showing good agreement to the experimental data. From the streamline plots it is seen that two fully developed vortices are present in the recirculation zone. Three mixing layers are identified inside the recirculation zone. Those layers are found between the outer vortex and the co-flow air, the outer vortex and the inner vortex and the inner vortex and the jet.

In order that the flow physics get resolved appropriately and the global imbalances for the conserved quantities get reduced to a specified lower value, residual convergence history and the imbalance monitors were observed closely. Model error study was performed for all the combinations of fuels with different velocities at fuel jet inlet, on all mesh resolutions. Comparison of the mixture fraction profiles with the experimental data showed that $k-\omega$ SST model for ANSYS CFX 16.1 and realizable $k-\epsilon$ model for ANSYS Fluent 17.0 were not consistent with the other models and also not in good agreement with the experimental data. The reason for that is shown from the comparison of the streamlines where it is shown that both $k-\omega$ SST and realizable $k-\epsilon$ model were predicting smaller length of recirculation zones, more significantly in case of realizable $k-\epsilon$ model. Also the mixture fraction profiles showed that both models were over-predicting the mixing of jet, significantly by realizable $k-\epsilon$ model , at certain intermediate locations downstream the bluff-body.

Comparison of the streamlines for Ethylene fuel jet with different velocities showed that the shift from double to single vortex structure in the recirculation zone happens in between intermediate and highest jet velocities. It is apparent from the figure that the outer vortex is more stable and stretches ~50 mm downstream the bluff-body, also it shows no effect towards the momentum change in the fuel jet. The inner vortex which is the smaller one and is sensitive towards the momentum change in the jet fuel. The central core of the inner vortex shifts downstream with the increase in the jet momentum and continues to shift until it loses its circular pattern.

In the solver comparison $k-\omega$ SST and $k-\epsilon$ model of ANSYS CFX 16.1 and ANSYS Fluent 17.0 were compared with each other and plotted against the experimental data. It was seen from the mixture fraction profiles that the realizable $k-\epsilon$ model was over-predicting the mixing of the jet fuel as compared to the other models and also the experimental data. Apart from that $k-\omega$ SST and standard $k-\epsilon$ model of both solvers were in good agreement with each other and the experimental data as well.

Hence for such type of isothermal, steady state flow configurations where turbulent mixing is involved, behind the bluff body or in the recirculations zone, $k-\omega$ SST and standard $k-\epsilon$ model would be the recommended turbulence models.

References

1. R.W.Schefer and R.W.Dibble,"Mixture Fraction Field in a Turbulent Non-reacting Propane Jet", AIAA Journal, Vol.39, no.1, pp.64-72, 2001
2. R.W.Schefer, V.Hartmann and R.W.Dibble, "Conditional Sampling of Velocity in a Turbulent Nonpremixed Propane Jet", AIAA Journal, Vol.25, no.10, pp.1318-1330, 1987
3. Robert W. Schefer "Data Base for a Turbulent, Non-premixed, Non-reacting Propane-Jet Flow ", Sandia National Laboratories Research Report, pp. 1-21, 1985
4. E.J. Smith, J. Mi, G.J. Nathan and B.B. Dally, "Preliminary Examination of a" Round Jet Initial Condition Anomaly" for the k- ϵ Turbulence Model", 15th Australian Fluid Mechanics Conference, 13-14 December 2004
5. S. B. Pope, "An Explanation of the Turbulent Round-Jet/Plane-Jet Anomaly", AIAA Journal, Vol.16, no.3, pp.279-281, 1978
6. The University of Sydney, Department of Mechanical and Mechatronic Engineering and Sandia National Laboratories Combustion Research Facility, "Turbulent Non premixed Combustion Data for Piloted and Bluff-Body Stabilized Flows", <http://sydney.edu.au/engineering/aeromech/thermofluids/bluff.htm>
7. Dally, Bassam B., Masri, Assaad R., Fletcher, David F. "Modeling of bluff body recirculating flows", Twelfth Australasian Fluid Mechanics Conference, The University of Sydney, Australia, pp. 529-532, 1995
8. B.B.Dally, D F Fletcher & A.R.Masri, "Flow and mixing fields of turbulent bluff-body jets and flames", Combustion Theory and Modeling 2, pp.193-219, 1998
9. Jiyuan Tu, Guan Heng Yeoh and Chaoqun Liu, "Computational Fluid Dynamics A Practical Approach", Elsevier, 2008
10. H K Versteeg and W Malalasekera, "An Introduction to Computational Fluid Dynamics THE FINITE VOLUME METHOD", Pearson, 2007
11. ANSYS ICEM CFD USER GUIDE
12. ANSYS CFX THEORY GUIDE
13. ANSYS FLUENT THEORY GUIDE
14. ERCOFTAC CFD BEST PRACTICE GUIDELINES

15. Kai Liu, Stephen B. Pope, David A. Caughey, "Calculations of bluff-body stabilized flames using a joint probability density function model with detailed chemistry", Combustion and Flame, Vol.141, pp.89-117, 2005
16. Robert W Elliott, Harry Watts, "Diffusion of some Hydrocarbons in Air: a Regularity in the Diffusion Coefficients of a Homologous Series", Canadian Journal of Chemistry, Vol.50, pp. 31-34, 1972
17. Michael Andreas Wild, "General Purpose PDF Solution Algorithm for Reactive Flow Simulations in OpenFOAM", ETH ZÜRICH , Doctoral Thesis, 2013
18. Christopher M. Briggs Jr., "Large Eddy Simulation of Non-Reacting Jet", University of Maryland, Master Thesis, 2015
19. F.C.Gouldin, R.W.Schefer, S.C.Johnson, W.Kollmann, "Non-reacting Turbulent Mixing Flows", Progress in Energy and Combustion Science, Volume 12, Issue 4, pp.257-303, 1986
20. Moss, J. B., "Simultaneous Measurements of Concentration and Velocity in an Open Premixed Turbulent Flame," Combustion Science and Technology, Vol. 22, No. 1, pp. 119–129, 1980.
21. Driscoll, J. F., Schefer, R.W., and Dibble R.W., "Mass Fluxes Measured in a Turbulent Nonpremixed Flame," Nineteenth Symposium (International)on Combustion, Combustion Inst., Pittsburgh, PA, pp. 477–485, 1982.
22. F.R.Menter, "Two-equation eddy-viscosity turbulence models for engineering applications", AIAA-Journal., 32(8), pp. 1598 - 1605, 1994.
23. Yoshihide Tominagaa, Ted Stathopoulos, "Turbulent Schmidt numbers for CFD analysis with various types of flow-field", Atmospheric Environment, Vol. 41, pp.8091-8099, 2007

Appendix

1. Sandia Propane Jet

1.1. Iteration or Convergence Error ANSYS CFX 16.1

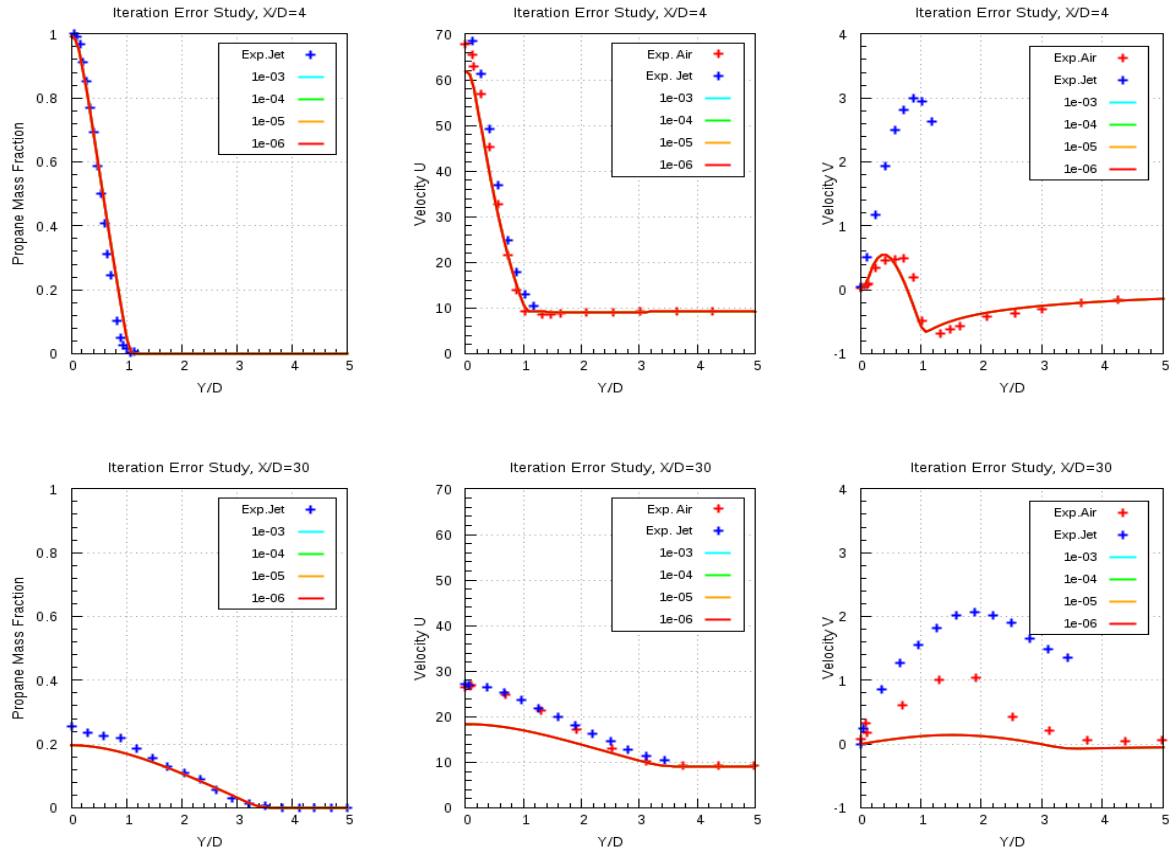
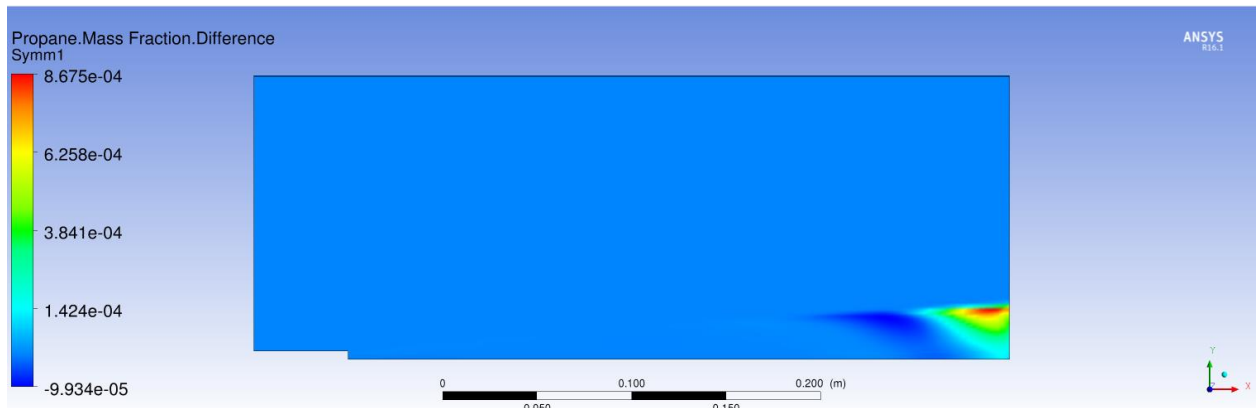


Figure 1

Propane Mass fraction difference contours



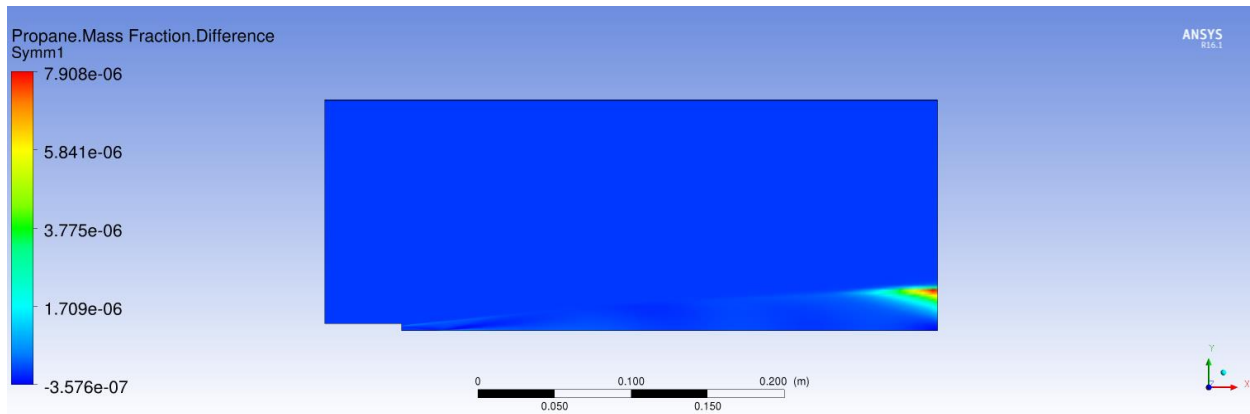


Figure 2

Spatial Discretisation Error for ANSYS CFX 16.1

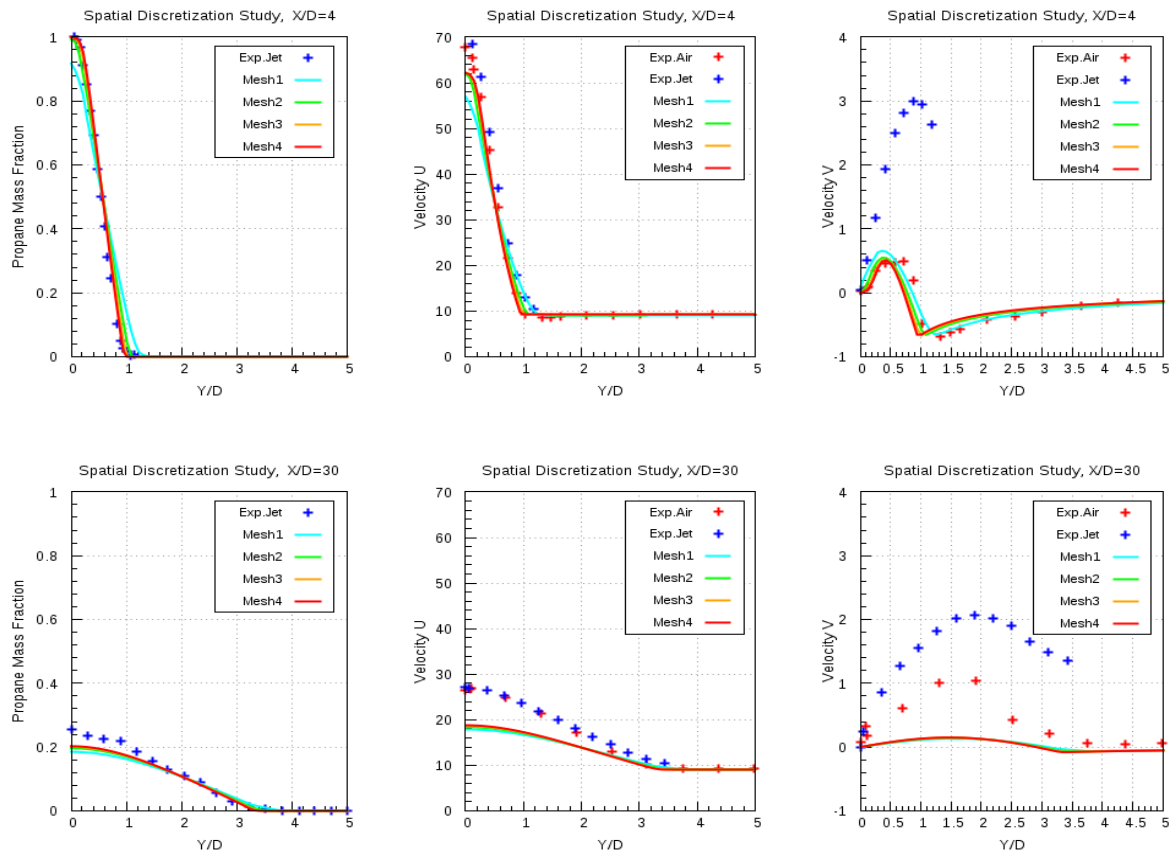


Figure 3

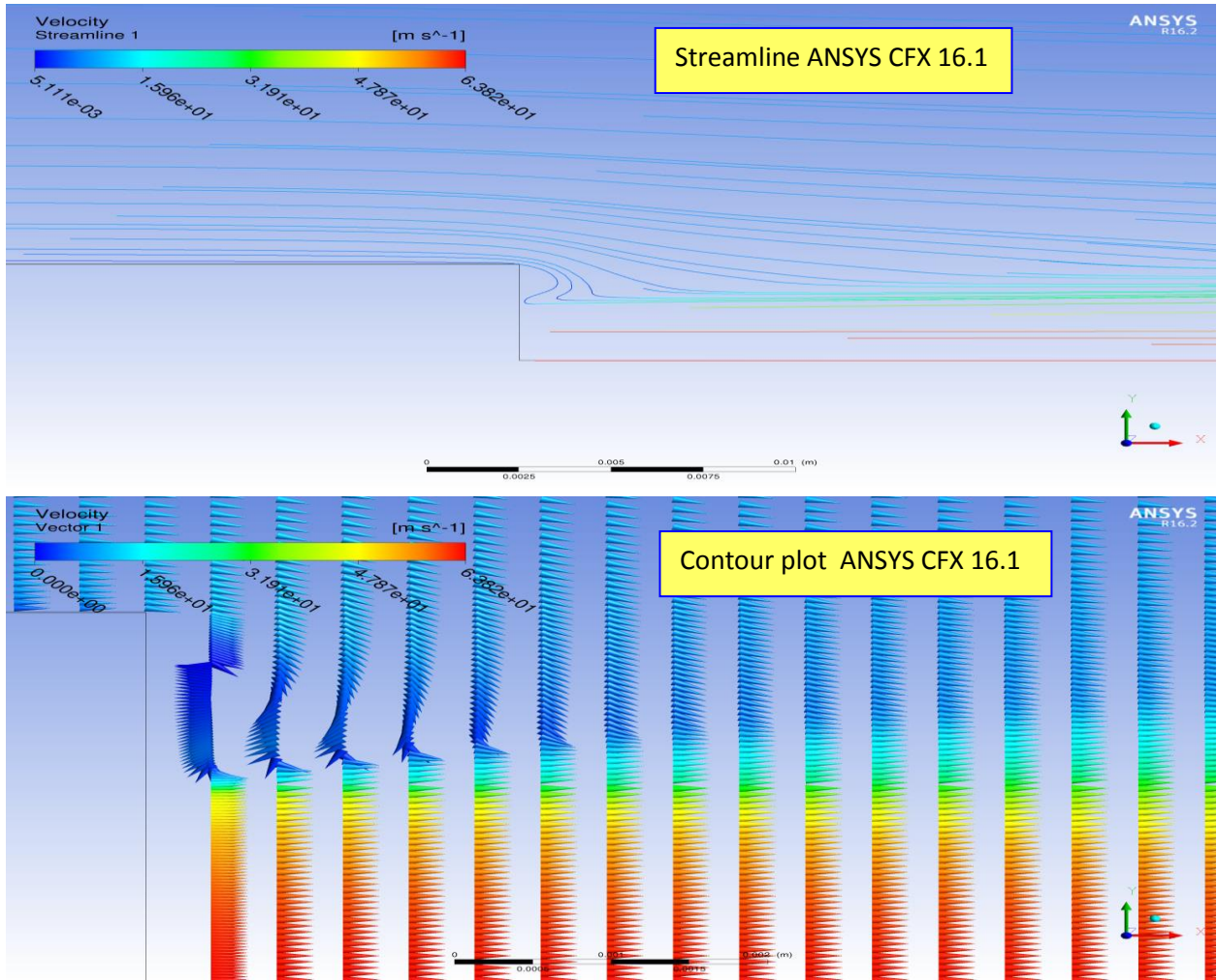
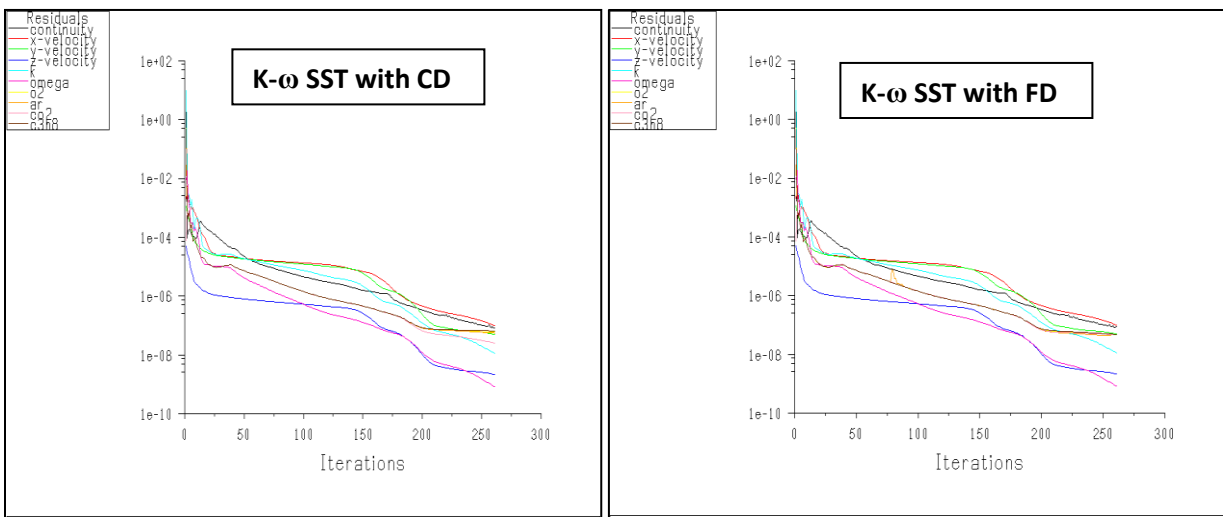


Figure 4
Model Error Study (ANSYS Fluent 17.0):



Residual convergence history (ANSYS Fluent 17.0)

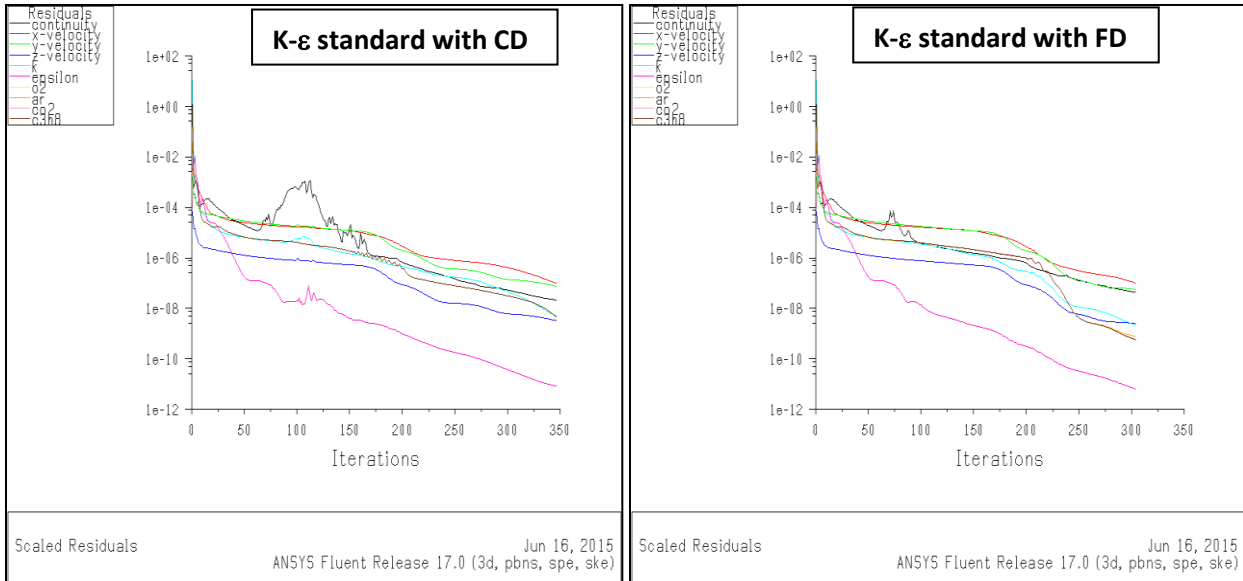


Figure 5

Radial profile plots for ANSYS Fluent 17.0

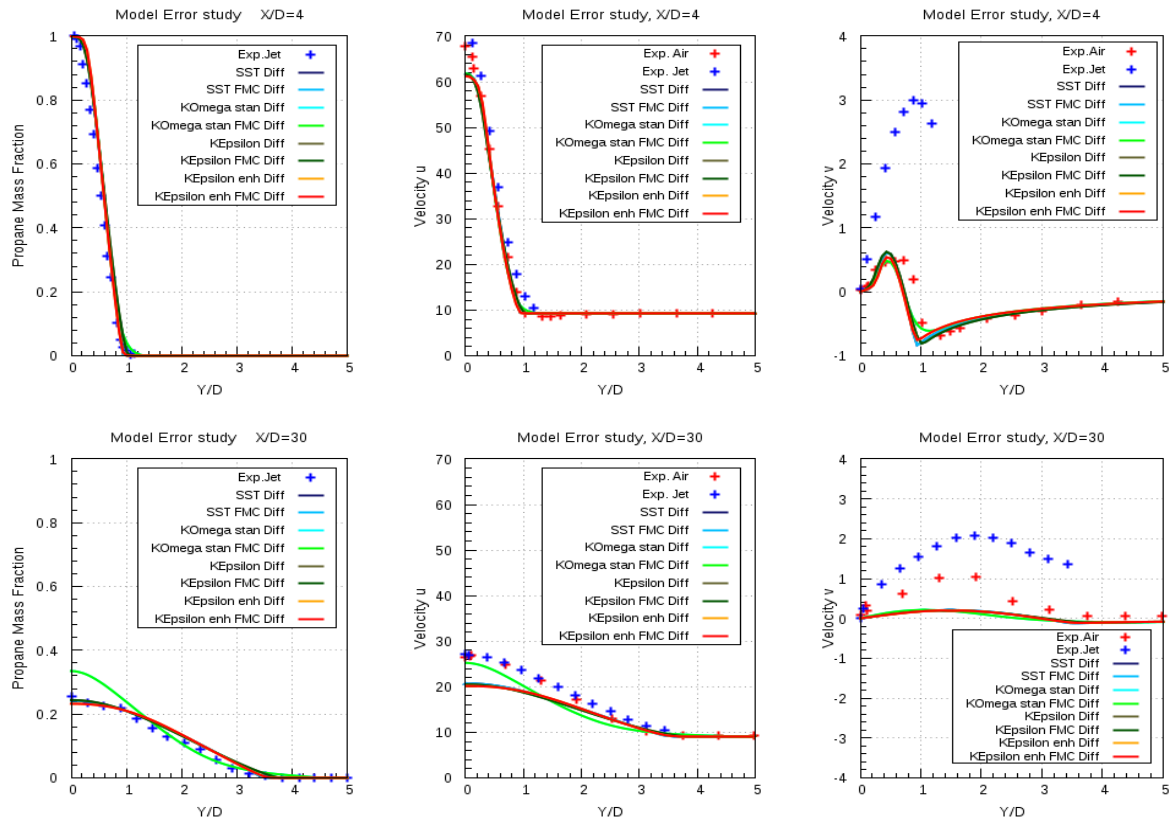
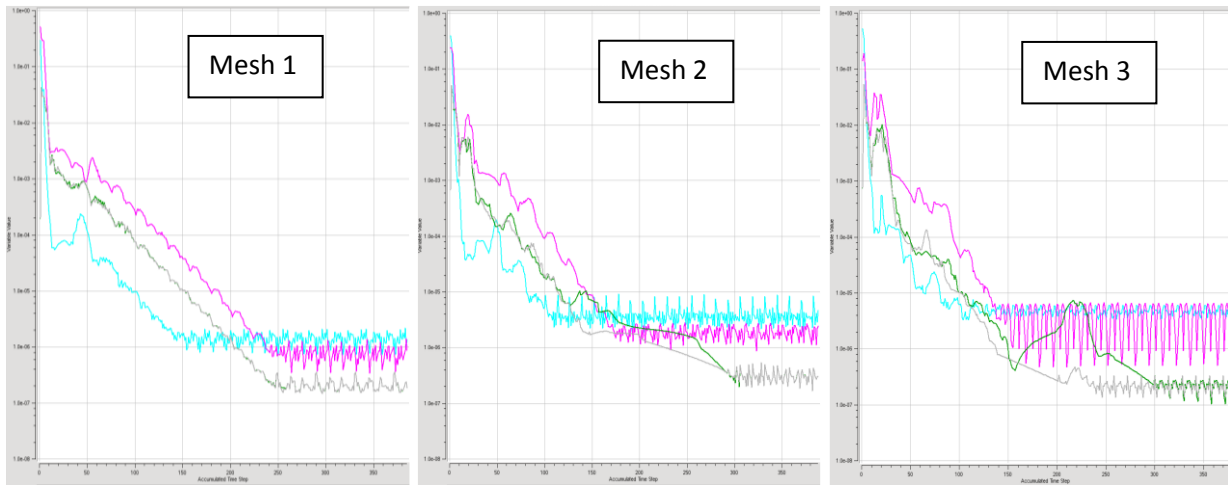


Figure 6

Sydney Bluff Body:

Spatial discretization study for ANSYS CFX 16.1:

Residual convergence history



Imbalance monitor plots

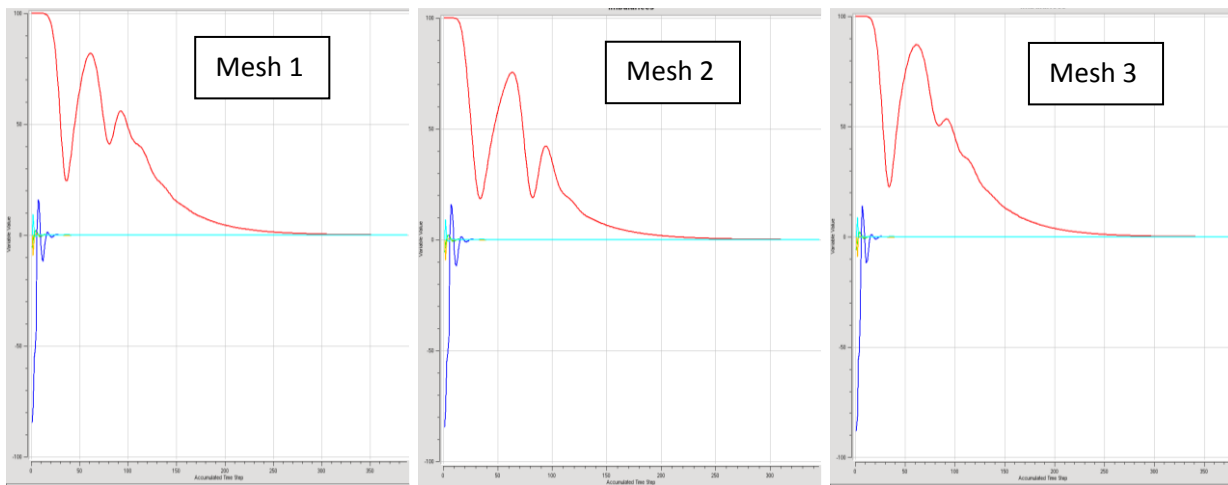


Figure 7

Model Error Study (ANSYS CFX 16.1)

Residual history and Imbalance monitors for CNG fuel, $U_J = 50 \text{ m/s}$

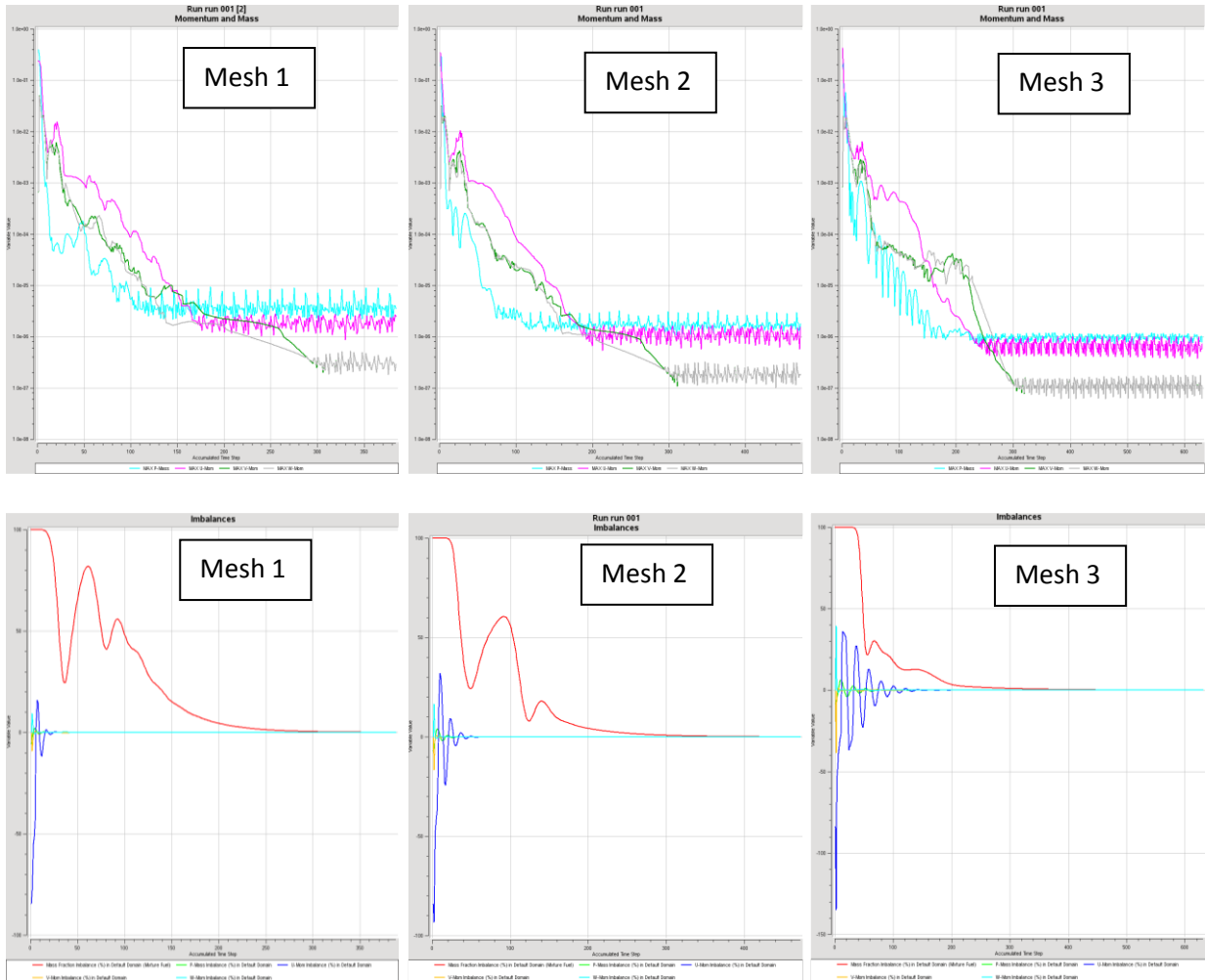
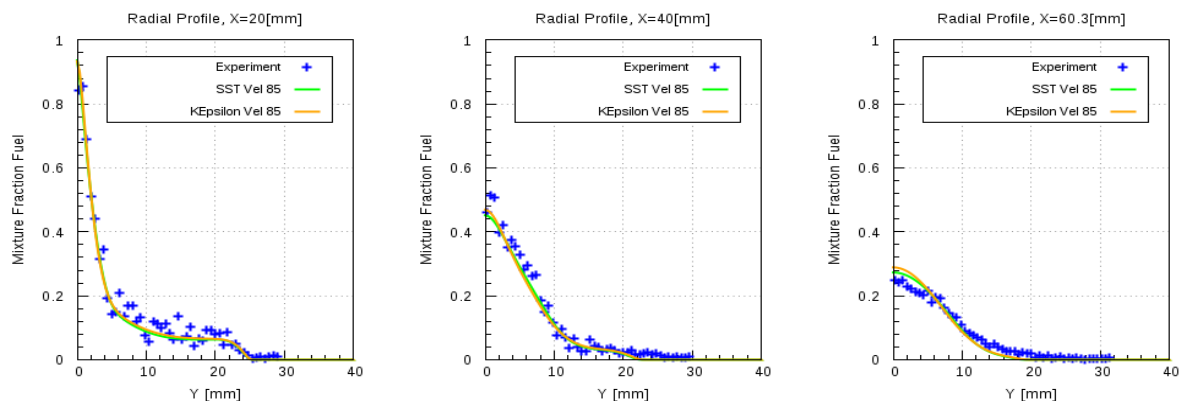


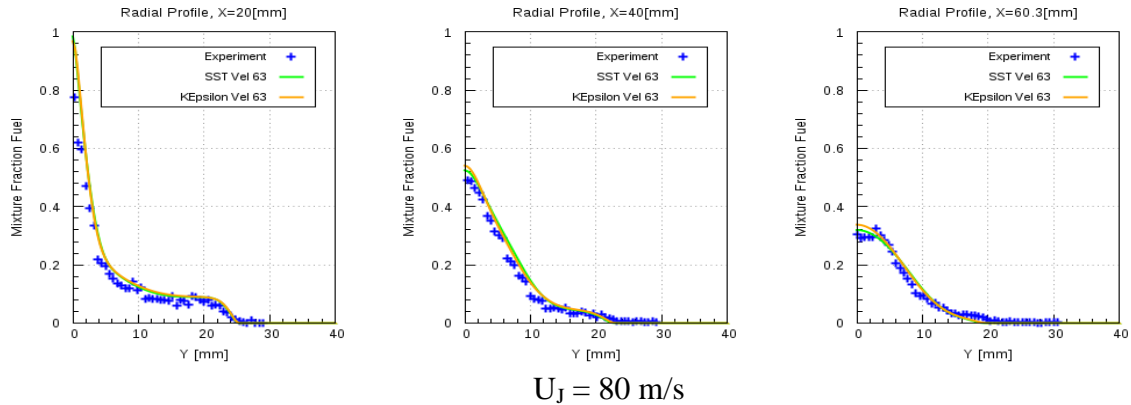
Figure 8

Ethylene:

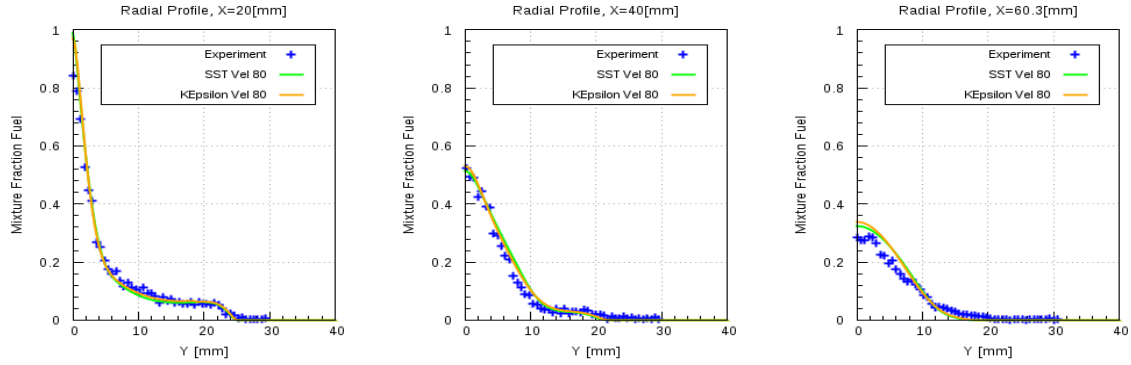
$U_J = 50 \text{ m/s}$



$U_J = 63 \text{ m/s}$



$U_J = 80 \text{ m/s}$



LPG:

$U_J = 50 \text{ & } 70 \text{ m/s resp}$

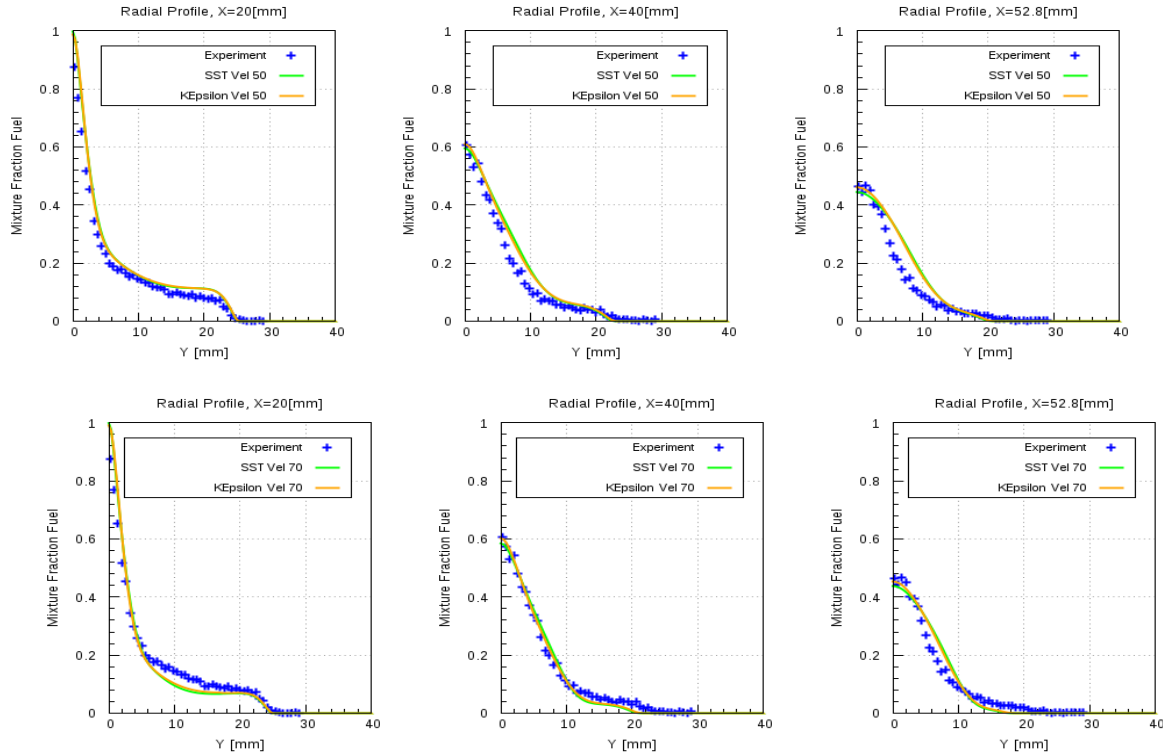


Figure 9

Residual convergence history (ANSYS Fluent 17.0) for CNG at $U_J = 50, 85 \& 143$ m/s :

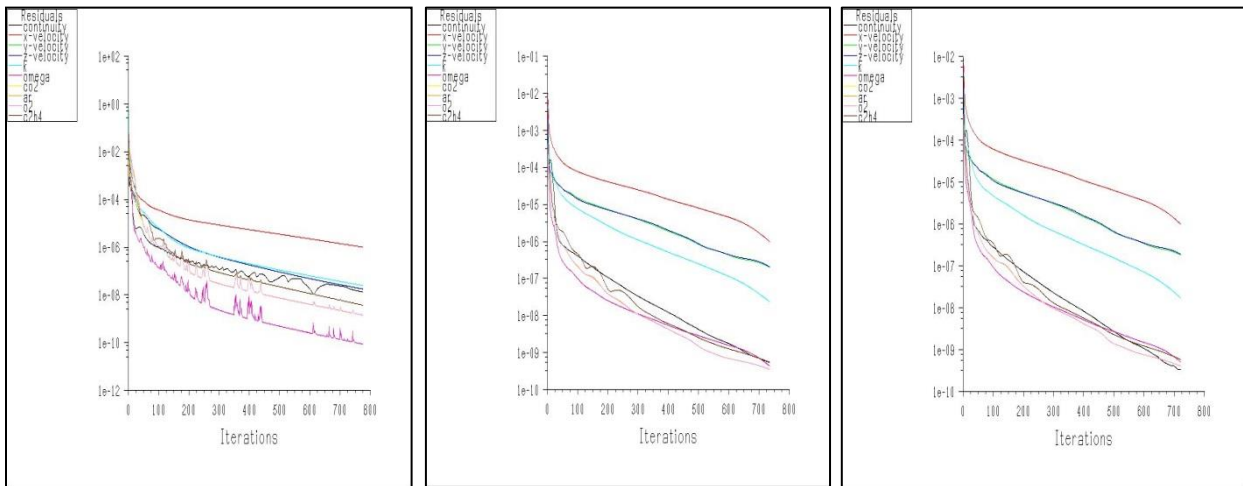


Figure 10

Solver comparison

CNG fuel $U_J = 50$ m/s

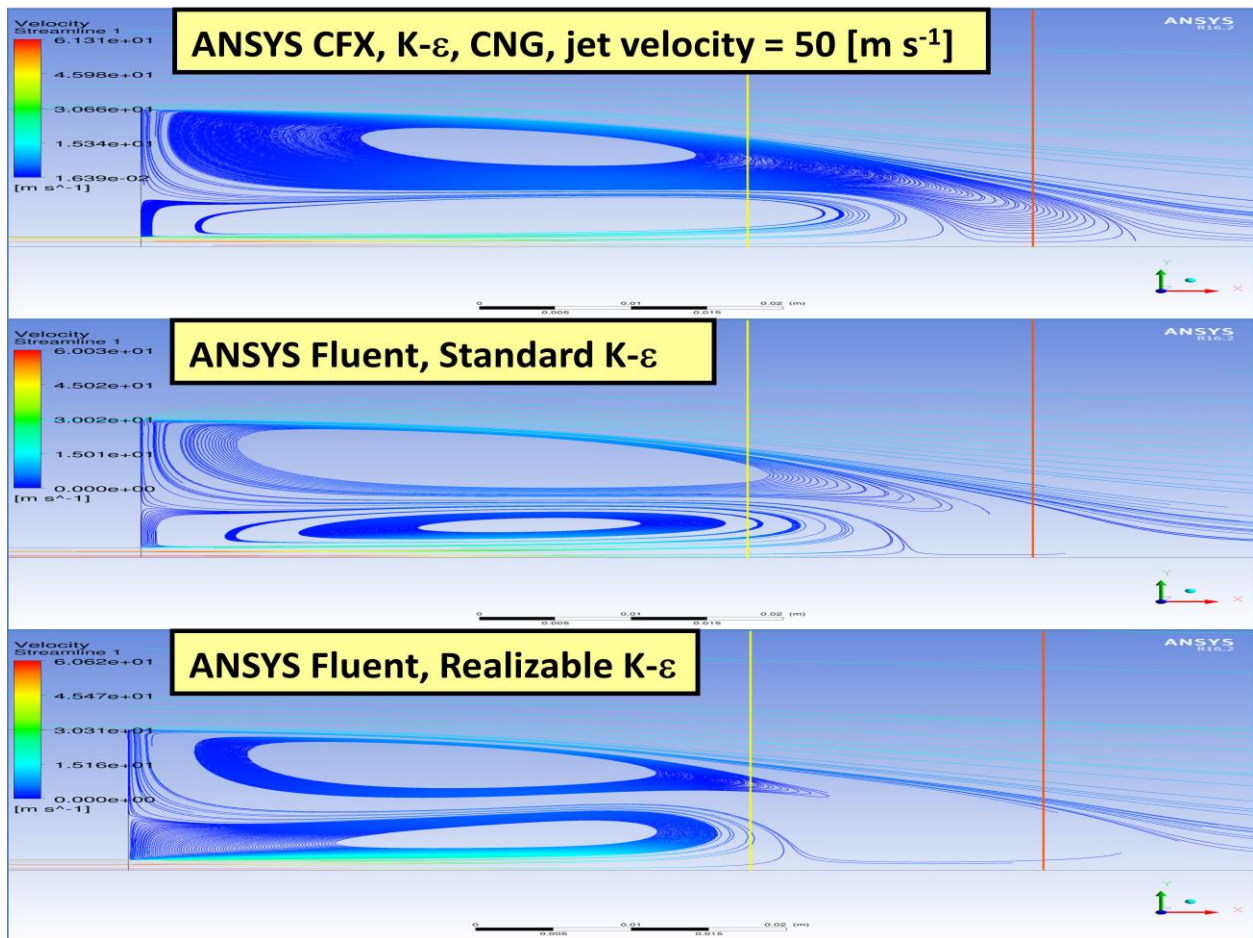


Figure 11

Contour plots for CNG, $U_J = 50 \text{ m/s}$

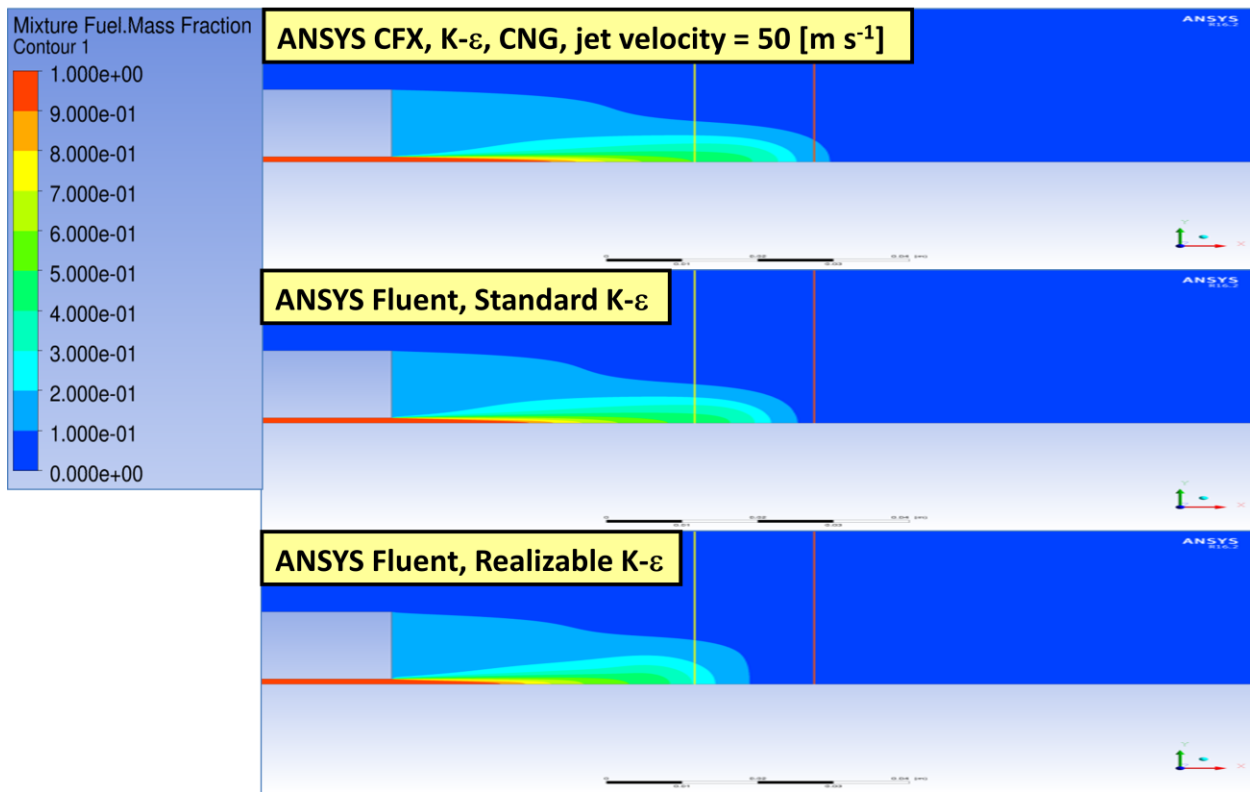


Figure 12

Ethylene:

$$U_J = 50 \text{ m/s}$$

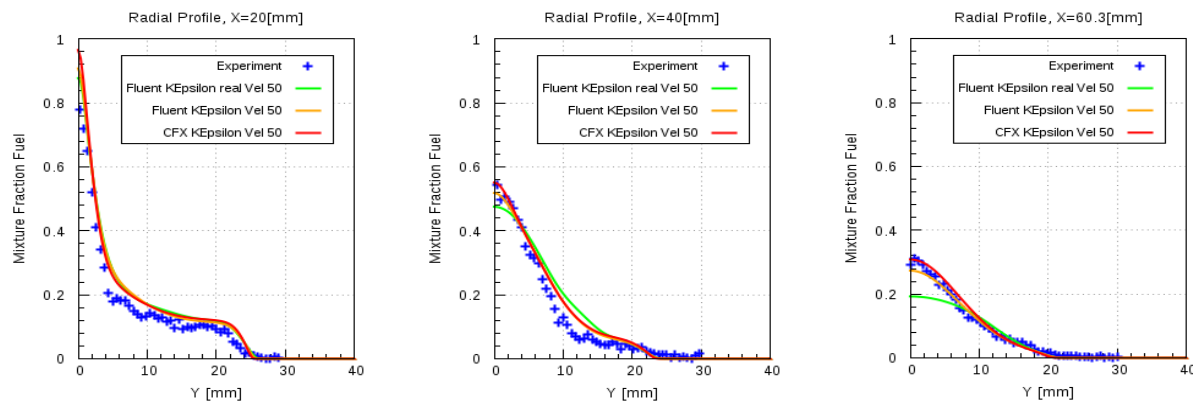
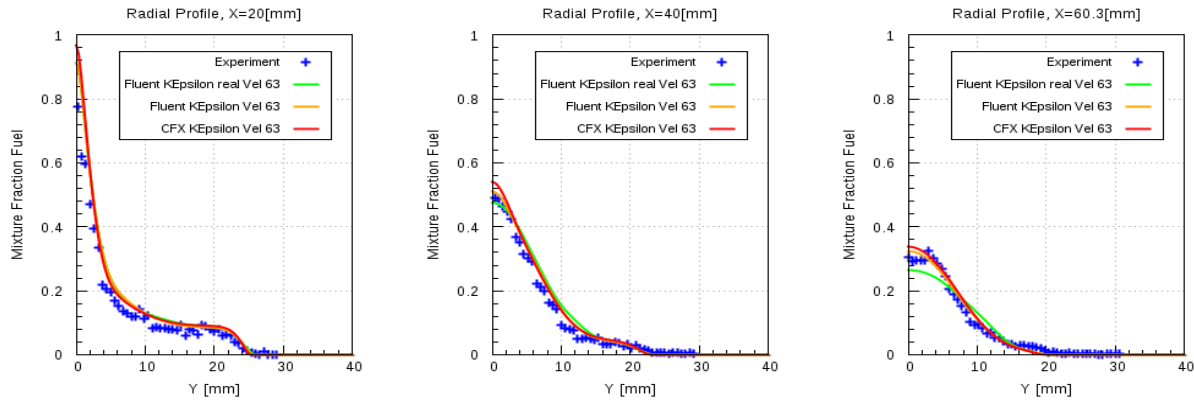


Figure 13

$U_J = 63 \text{ m/s}$



$U_J = 80 \text{ m/s}$

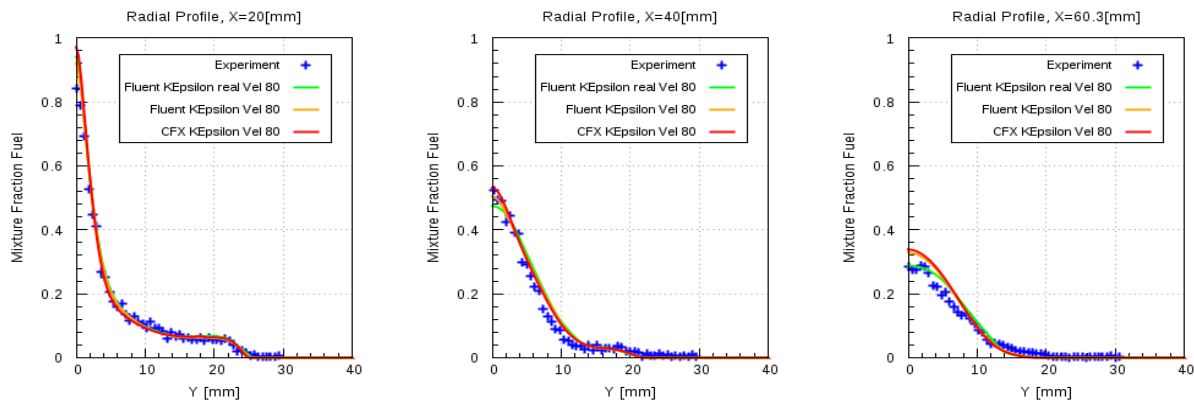
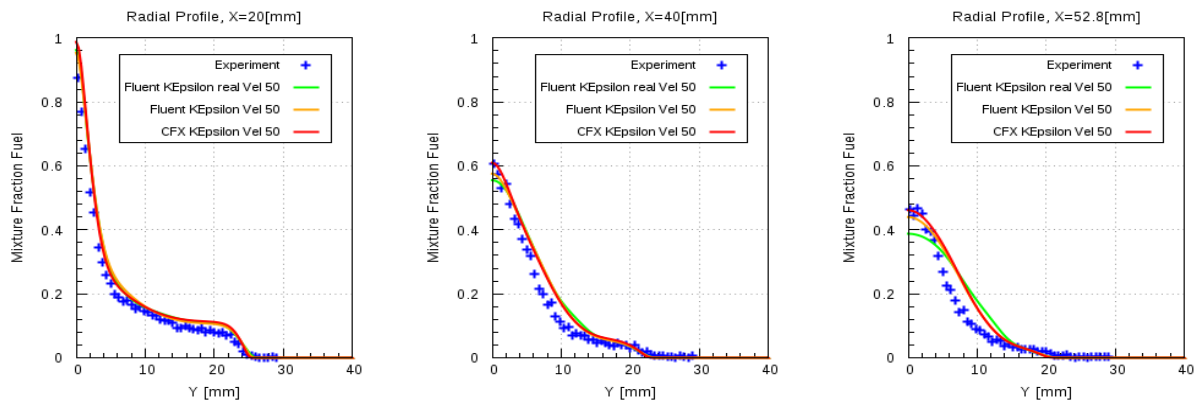


Figure 14

LPG (k- ϵ model)

$U_J = 50 \text{ m/s}$



$$U_J = 70 \text{ m/s}$$

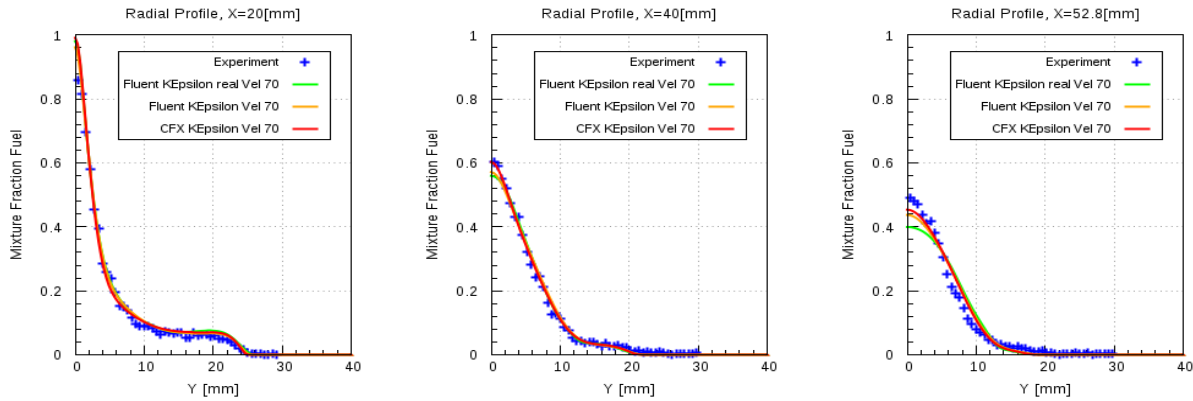
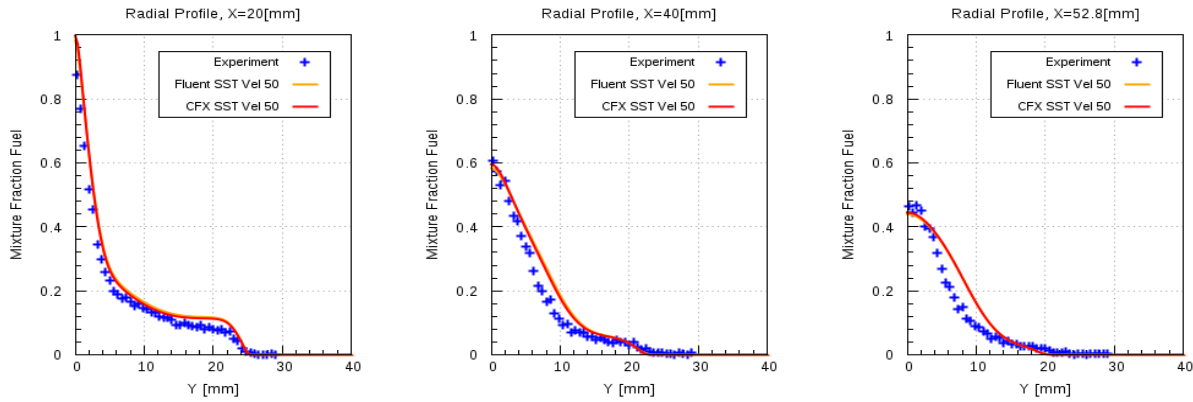


Figure 15

LPG($k-\omega$ SST)

$$U_J = 50 \text{ m/s}$$



$$U_J = 70 \text{ m/s}$$

